The Dissertation Committee for Ning Li Certifies that this is the approved version of the following dissertation:

High-Output-Power Photodetectors for Analog Optical Links and Avalanche Photodiodes with Undepleted Absorber

Committee:

Joe C. Campbell, Supervisor

Archie L. Holmes, Jr.

Dean P. Neikirk

Leonard F. Register

David A. Tulchinsky

High-Output-Power Photodetectors for Analog Optical Links and Avalanche Photodiodes with Undepleted Absorber

by

Ning Li, B.S.; M.S.

Dissertation

Presented to the Faculty of the Graduate School of

The University of Texas at Austin

in Partial Fulfillment

of the Requirements

for the Degree of

Doctor of Philosophy

The University of Texas at Austin

December, 2005

Acknowledgements

First of all, I would like to express my deepest appreciation and gratitude to my advisor, Dr. Joe C. Campbell. It was his advice, support, and encouragement that guided me to gradually find a path of doing research in my Ph.D. program. His enthusiasm and insightfulness for research, together with encouragement for new ideas, constantly inspired me and will continue to be my guidance in the future. I also enjoyed very much his excellent leadership that gave the research team an active, free and collaborative atmosphere, which made this group a great place to learn and grow.

I am in debt to Dr. Archie L. Holmes, Jr. His MBE group has been providing me with materials of great quality, which is crucial to many projects. I also benefited greatly from the discussion with him during and after our weekly group meetings, especially on the high power photodiode wafer bonding project. I appreciate Dr. Dean P. Neikirk, Dr. Leonard F. Register and Dr. David A. Tulchinsky for kindly serving on my committee, reviewing my work, and giving advices. I would also like to thank all the faculty and staff members at the Microelectronics Research Center for providing such a nice environment for conducting graduate research.

I want to thank Dr. David A. Tulchinsky and Dr. Keith J. Williams at Naval Research Laboratory for the long term very helpful collaboration on the

high power photodiode project. The discussion with them made me look much deeper into the problem. The project would never be successful without their encouragement. I appreciate Dr. Eric Harmon and Dr. David Salzman at Lightspin Technologies, Inc. for their interest and helpful discussion on avalanche photodiodes with undepleted absorber.

I would like to thank my fellow research group members and colleagues, Xiaoguang Zheng, Xiaowei Li, Stephane Demiguel, Rubin Sidhu, Hao Chen, Feng Ma, Gauri Karve, Shuling Wang, Ariane L. Beck, Xiangyi Guo, Ning Duan, Jeff B. Hurst, Katie Lipson, Bo Yang, Zhengmao Ye, Jungwoo Oh, Geoffrey S. Kinsey, Charles C. Collins, Sebastian Csutak, Zhihong Huang, Xiaofeng Zhang, Mingguo Liu, Ning Tan and Lijuan Zhang. All of them have been my good friends and sources of learning during these years. It is impossible to enumerate all the contributions that they made to my research, but I wish to name a few. I really appreciate Rubin Sidhu and Hao Chen for growing high quality MBE materials, without which some of the work in this dissertation would be impossible. Xiaoguang Zheng kindly trained me to conduct complex cleanroom processing, and constantly assisted me in solving processing and testing problems. Xiaowei Li was my source of knowledge when I started on the high power photodiode project. Stephane Demiguel helped me a lot in high frequency measurements. I enjoyed very much the close collaboration with him on

waveguide photodiodes. Feng Ma was very resourceful in semiconductor physics, which stimulates many helpful discussions. I want to thank Shuling Wang for kindly helping me to get used to everything when I joined the group. I want to thank Gauri Karve for testing undepleted absorber avalanche photodiodes in Geiger mode and helpful discussions. Xiangyi Guo helped me in many ways. There were many interesting discussion with him, though we were working on different materials. I want to thank Ning Duan for helping me with processing and measurements and for helpful discussions. Thank Mingguo Liu for helping me in the simulation of resonant cavities. I am grateful to Ariane L. Beck and Dr. Joe C. Campbell for critical reading on all my dissertation chapters and gave me a lot of good advices.

I want to thank Geoff Kinsey and his colleagues at Spectrolab, Inc., Alex Pauchard and his colleagues at Nova Crystals, Inc., and Alex Anslem and his colleagues at Applied Optoelectronics, Inc., for providing high quality epitaxy materials.

I want to thank my previous advisor Dr. Yi Luo at Tsinghua University, Beijing, China, for stimulating my interest in doing research work in the optoelectronics field.

Finally, I want to express my gratefulness to my parents for encouraging me to pursue advanced study, which led me to this point.

High-Output-Power Photodetectors for Analog Optical Links and Avalanche Photodiodes with Undepleted Absorber

Publication No._____

Ning Li, Ph.D.

The University of Texas at Austin, 2005

Supervisor: Joe C. Campbell

High-power photodetectors are crucial components in analog optical links for applications, such as cable televisions, phased array antennas, antenna remoting, photonic signal processing, and future wireless communication systems. The link performance, which includes link gain, noise figure, and spurious free dynamic range, can be improved by increasing the optical carrier power and using a high-power photodetector. In this dissertation, an analysis of the limiting factors of photodiode output power is presented. Based on this analysis, improved photodiode structures that can suppress space charge effect and loading effect were designed and experimentally studied. Record high values of RF output power were obtained. In order to suppress laser relative intensity noise (RIN),

which limits the dynamic range of the link at high optical power, high-power top-illuminated and evanescently-coupled waveguide balanced photodetectors were demonstrated. High saturation current, broad bandwidth, high responsivity and good broadband common mode rejection ratio were achieved. Bonding photodiode to Si using a gold intermediate layer was demonstrated to improve the device heat handling capability. The responsivity of the bonded photodiode was also increased significantly due to the resonant cavity introduced by the gold bonding layer.

Avalanche photodiodes (APDs) are key components for optical communication, imaging and various photon counting applications. In the second part of this work, a novel avalanche photodiode structure with undepleted absorber was proposed and experimentally studied. Theoretical analysis shows that this structure could have orders of magnitude lower dark current than the APDs with depleted absorber. It also has the advantage of high low-gain bandwidth and no multiplication in the absorber. For the fabricated devices, low dark current performance was observed. Because of this property, the structure has potential to be used as a high performance photon counter.

Table of Contents

List of Tables

List of Figures

Chapter 1: Introduction

1.1 Photodetectors for analog fiber-optic links

With the invention and development of low loss optical fibers, lasers, photodetectors and other optoelectronic components, fiber-optic links are more and more widely used for transmitting high data rate or broadband signals. The major advantage of the fiber-optic link comes from its low loss and broad bandwidth. Figure 1 shows the attenuation characteristics of a silica optical fiber. The transmission loss near 1.55μm (~194THz) is below 0.2dB/km, which is more transparent than clear air. This means that a very large bandwidth is available with little attenuation. Other advantages of the fiber-optic links include low dispersion, immunity to electromagnetic interference, high security, light weight, and small size. These attributes make fiber-optic links the preferred transmission medium choice for many applications.

A fiber-optic link consists of a transmitter, an optical fiber, and a receiver. At the transmitting end, an electrical signal is converted into an optical signal. The signal then travels as an optical wave along the optical fiber. At the receiving end, the optical signal is converted back into an electrical signal using an optical receiver. The photodetector in the front end of the receiver module plays the crucial role of absorbing the optical signal and converting it into electrical current.

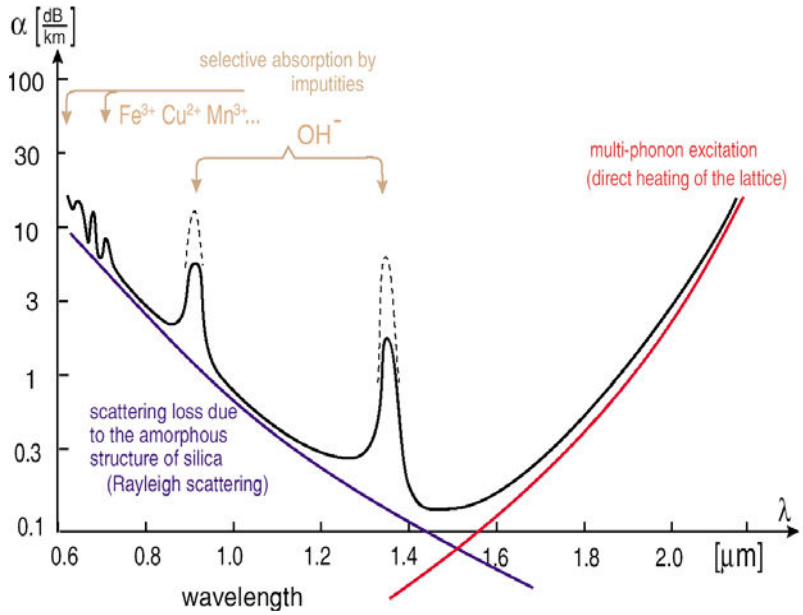

Figure 1.1 Attenuation characteristics of a silica optical fiber.

In order to exploit the low dispersion and low attenuation properties of the silica fiber at 1.3μm and 1.55μm, devices working at these wavelengths must be used. The operating spectral range of a photodetector is determined by the material used for the absorption region. Figure 1.2 shows the absorption coefficient of various semiconductor materials. $In_{0.53}Ga_{0.47}As$ is commonly used for fiber optic photodiodes because it is lattice matched to InP and has a high absorption coefficient at 1.3μm and 1.55μm.

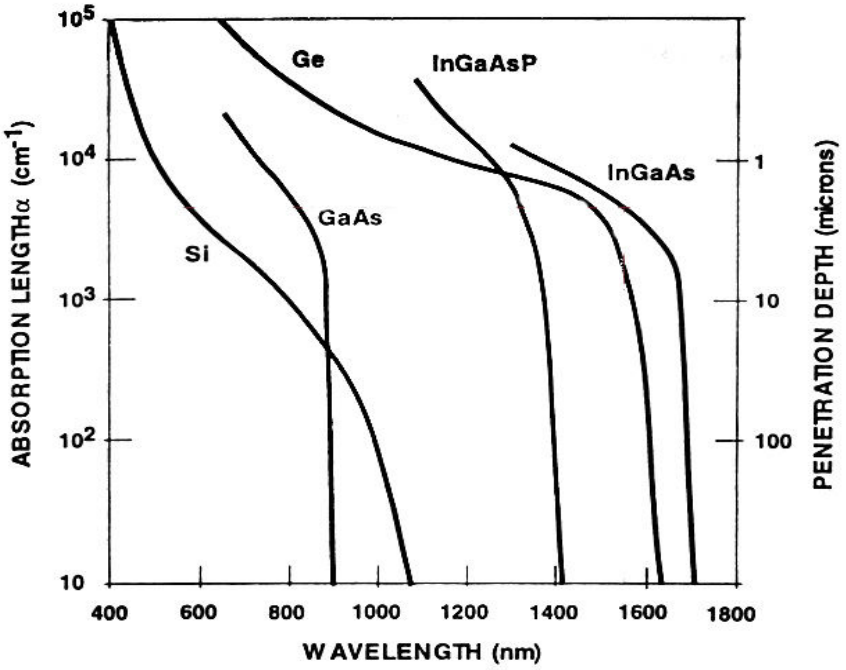

Figure 1.2 Absorption coefficients of semiconductor materials

1.1.1 Analog optical links

Today the vast majority of fiber-optic links for telecommunications and data networks are digital. However, there are a fast growing number of applications for analog fiber-optic links [1-1]. Figure 1.3 shows the block diagram of an intensity-modulated direct-detection (IMDD) analog optical link [1-2]. It consists of lasers and modulators to impose the RF signal onto the optical carrier, an optical fiber as the transmission medium, and a photodetector to recover the RF signal from the optical carrier.

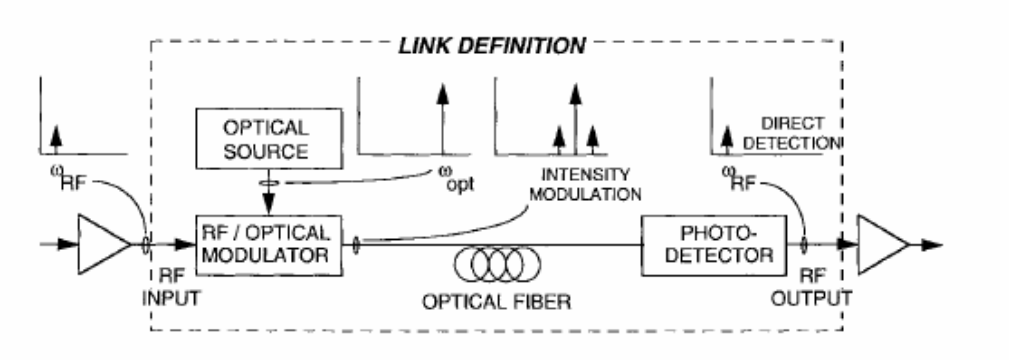

Figure 1.3 Block diagram of intensity-modulation direct-detection (IMDD) analog optical links [1-2]

The major applications for analog fiber-optic links include cable television, phased array antennas, antenna remoting, optical signal processing, and wireless communication [1-3]-[1-7]. The distribution of cable television signals to the local hub via analog optical links eliminates the high loss electrical cables and broadband electrical amplifiers. In phased array antenna systems, using fiber-optic links reduces both the weight and volume of the electrical beam-forming networks. In antenna remoting applications, where RF or microwave signals are transferred to remote sites, low-loss optical fibers can replace the coaxial cables, allowing the expensive signal processing equipment to be kept at a central station. Analog fiber optical links can also be used to process wideband microwave signals optically using optical delay lines, filters and AD-DA converters. In the future, analog optical links have potential for use in wireless communication systems. In order to accommodate more data, higher frequency carriers will be

used in wireless communications. At these higher frequencies, conventional coaxial cable performs poorly, whereas analog fiber-optic links can transmit high frequency subcarriers with very low loss. With fibers linking numerous antennas, wireless communication can provide full or increased coverage in areas with poor reception, such as in underground stations, tunnels, parking structures and in/between buildings.

For digital links, the most important requirements for photodetectors/receivers are sufficient bandwidth and low bit-error-rate (BER). Due to the nature of analog signals, transmitting the signal with as little distortion as possible requires the analog link to have very high linearity and a large dynamic range [1-8, 1-9]. For example, a cable TV network [1-10] requires high gain and low noise figure optical links. A phased array antenna [1-11] requires both wide dynamic range and high linearity. One means of increasing the dynamic range and reducing the noise figure of a photonic link is to increase the optical carrier power [1-8]. On the receiver side, a high output power photodetector is needed to recover this high power signal. Figure 1.4 shows an illustration of calculated spur-free dynamic range versus total photodetector current for various levels of laser relative intensity noise (RIN) in an externally modulated fiber-optic link [1-8]. The system dynamic range increases as the

photocurrent increases until it is limited by the laser RIN. This establishes a challenge for the development of high power photodetectors for these applications.

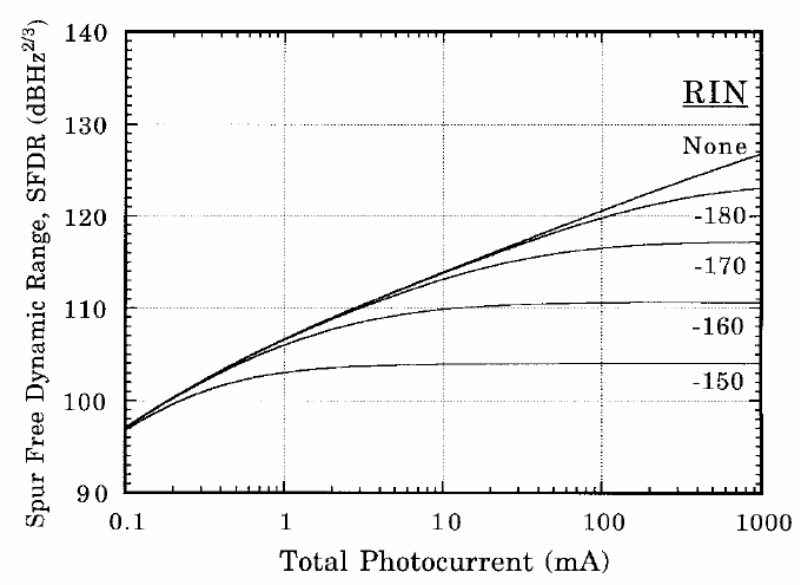

Figure 1.4 Calculated spur-free dynamic range versus total photodetector current for various levels of laser RIN in an externally modulated fiber optic link [1-8]

1.1.2 A brief review of approaches for high-power photodetectors

As discussed above, the requirements for analog optical links challenge the limit of the photodetector output power. In the digital domain, using high power photodetectors and optical amplifiers in the receiver can also decrease the complexity of high-bit-rate digital receivers [1-12, 1-13] and increase the receiver sensitivity.

Unfortunately, photodetectors saturate at high current levels [1-8]-[1-13]. The characteristics of saturation include RF power compression, bandwidth reduction and significant nonlinearities. The main factors causing the photodiodes to saturate are analyzed in detail in chapter 3. The space charge effect is one of the primary factors, and is caused by the increased density of mobile electrons and holes in the depletion region as the photocurrent increases. This mobile space charge will modulate the electric field and cause the electric field to collapse at high current levels. Once the electric field collapses, the carrier velocity decreases, and saturation occurs. Various device structures have been reported to reduce the space charge in the depletion region, such as uni-traveling-carrier photodiodes [1-14]-[1-16], a dual-depletion region photodiode [1-17], partially depleted absorber photodiodes [1-18, 1-19], waveguide photodiodes [1-20]-[1-23], and a velocity matched waveguide photodiode [1-24]. In order to suppress laser RIN, these photodiodes needs to be incorporated into a balanced photodetector configuration [1-25]-[1-27]. The above device structures will be reviewed briefly in the following.

A. Uni-traveling-carrier (UTC) photodiode

Davis et al. [1-28] reported a photodetector with a 3μm-thick undepleted InGaAs absorber and a 5μm-thick InP depletion region in 1996 to decouple the device capacitance and quantum efficiency. The device had a RC limited

bandwidth of 295MHz and a small-signal saturation current of 150mA. The quantum efficiency at 1319nm was close to 100%. In 1997, Ishibashi et al. [1-14] demonstrated that this kind of photodiode could achieve high-speed and high saturation current operation, if the layer thicknesses were designed properly. Since only electrons transit the depletion region, it was named as a uni-traveling-carrier photodiode.

A schematic band diagram for a UTC-PD is shown in Figure 1.5. The active layer of the UTC-PD consists of a p-type light absorption layer and a wide bandgap depletion layer. The photo-generated holes respond within the dielectric relaxation time, which is on the order of femtoseconds [1-14]. The photo-generated electrons travel from the p-type absorbing layer to the wide bandgap depletion region by diffusion and drift. If the InP depletion layer is thin enough, the electrons can travel at overshoot velocity [1-14]-[1-16] in this region. Therefore, the total space charge density in the depletion region of a UTC PD is much smaller than that in a conventional PIN photodiode, where the slow holes dominate. High bandwidth and high output RF power have been reported for UTC photodiodes [1-15, 1-16].

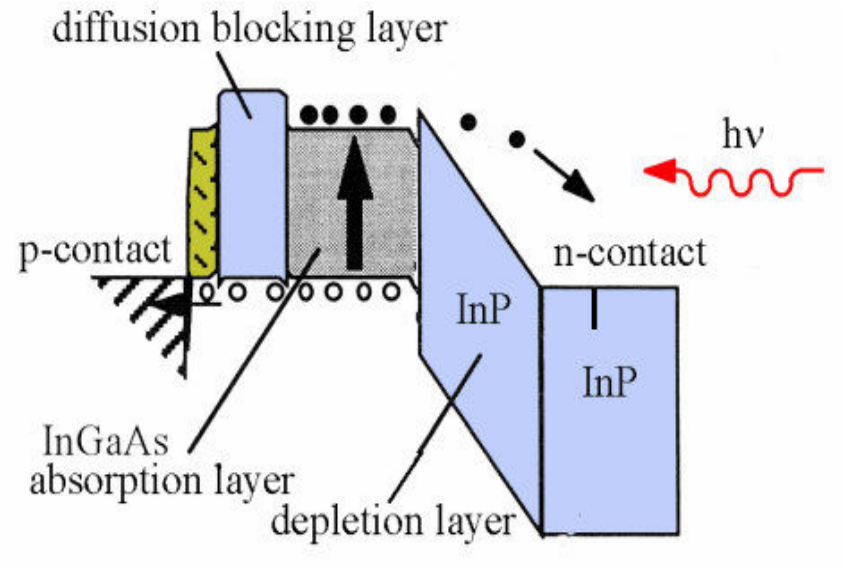

Figure 1.5 Band diagram of uni-traveling-carrier photodiode

B. Dual-depletion region photodiode

Another promising design for high-speed and high-saturation-current photodetectors is the dual-depletion-region (DDR) photodetector [1-17]. The depletion region consists of two layers. Typically, the first layer is a narrow bandgap absorption region, and the second layer is a wide bandgap non-absorption region. In this structure, the electrons travel a longer distance than the holes. Since the electron travels faster, the transit times for electrons and holes can be balanced. An advantage of this approach is that the photodiode capacitance can be reduced without increasing the carrier transit time. The dual-depletion-region photodetector was first proposed by Abhay Joshi. Simulation work shows

that the DDR is a promising candidate to achieve both high-speed and high-saturation-current [1-29].

C. Partially-depleted-absorber (PDA) photodiode

Figure 1.6 shows the structure of a PDA photodiode. This structure employs a relatively thick, partially depleted InGaAs absorption layer. The thickness of the p-, i-, and n- layers can be adjusted for optimum performance. The main advantage of this structure is that it can deliver high quantum efficiency while minimizing the space charge effects, by using a thin depletion region. It has a much lower space charge density than a PIN photodiode with the same thickness InGaAs absorption layer. Compared to the UTC photodiode, the photogeneration of holes in the intrinsic layer of the PDA can result in larger space charge. However, this effect is not as severe if the depletion layer is thin. Unlike UTC photodetectors, there are no band discontinuities to cause carrier "pileup," which is common at heterojunction interfaces. For these reasons, the PDA can be operated under low bias voltage to reduce the total power consumption, while still suppressing saturation [1-18, 1-19].

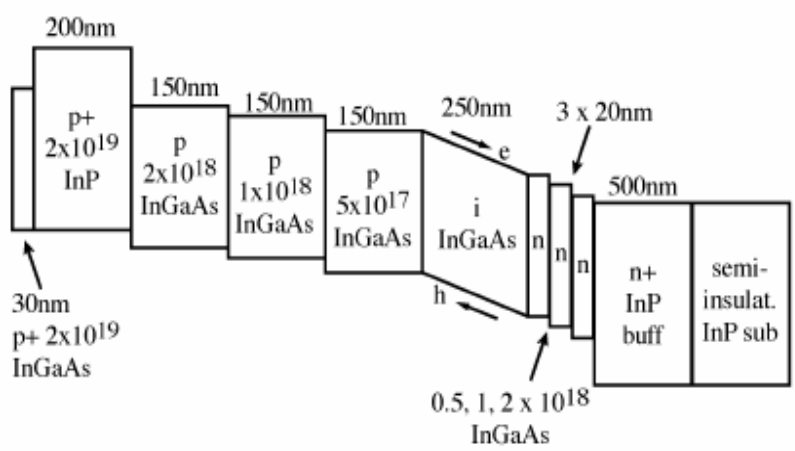

Figure 1.6 Schematic band diagram of a partially-depleted-absorber (PDA) photodiode

D. High power waveguide photodetector

For the surface illuminated photodiode, there exists a tradeoff between quantum efficiency and carrier transit time. This tradeoff limits the responsivity of high speed devices. Side-illuminated photodiodes can overcome this restriction by decoupling the responsivity and transit time. Directly side-illuminated photodiodes have achieved both high responsivity and broad bandwidth [1-20]. However, they have poor optical power handling capability due to high current density near the waveguide input facet. Evanescently-coupled waveguide photodiodes can achieve a much higher saturation current than the directly side-illuminated approach [1-21, 1-22], owing to more uniform light absorption. Figure 1.7 shows an example of a structure that utilizes two single mode tapers to

increase the coupling efficiency with a single mode fiber input [1-21]. High responsivity, high speed and good saturation power can be achieved with this type of waveguide photodiode.

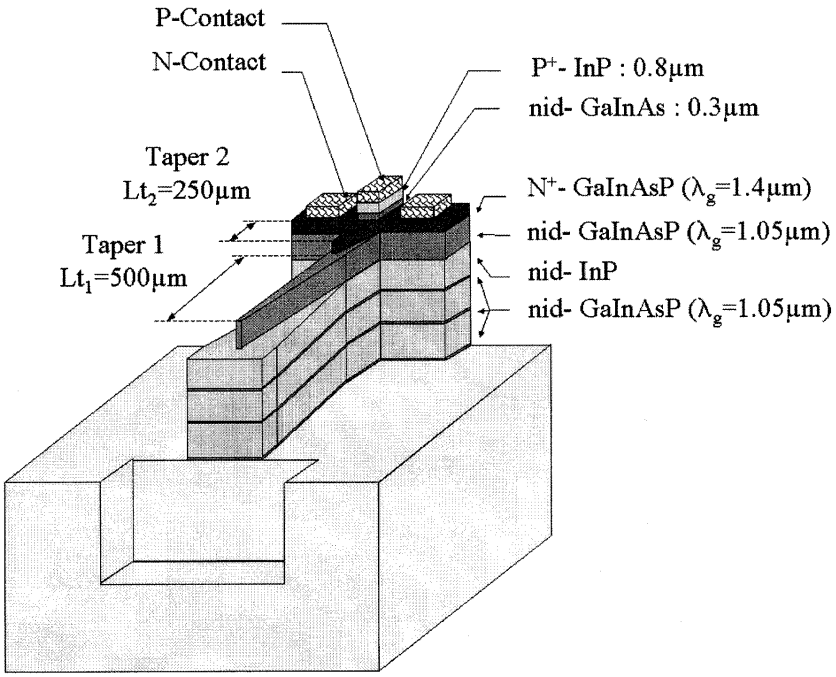

Figure 1.7 Double stage taper waveguide photodiode [1-21]

E. Velocity matched distributed waveguide photodiode

Another type of waveguide high power photodetector is the velocity-matched waveguide photodetector. It consists of an array of individual photodiodes serially connected by long, passive waveguides and transmission lines [1-24]. An advantage of the periodic configuration is the feasibility of velocity matching between the microwave phase velocity and the optical group

velocity using electrical delay. The light absorption can also be distributed to several photodiodes along the waveguide to reduce the space charge density.

F. Balanced photodetector

In high power and high frequency analog optical links, the link performance, including the link gain, noise figure, and spurious free dynamic range, can be improved by increasing the power of the optical carriers. However, as the optical power level increases, the relative intensity noise (RIN) of the laser source and the amplified spontaneous emission noise (ASE) from the erbium-doped fiber amplifiers (EDFAs) will become dominant and set an upper limit on the signal-to-noise ratio of the system [1-25]. Balanced photodetection can be used to suppress laser RIN and EDFA ASE noise [1-25]-[1-27]. Therefore, in order to fully utilize the high power capability of the photodiodes to improve system performance, balanced detection is required. By using a high-saturation-current balanced photodetector, the optical link can achieve shot noise limited performance at high optical powers. In optical heterodyne receivers using optical local oscillators, high power balanced photodetectors also serve the function of suppressing local oscillator noise. Previously, balanced photodetectors with discrete photodiodes [1-25], waveguide photodiodes [1-26], and velocity-matched distributed configurations [1-27] have been reported.

1.2 Avalanche photodiodes

An avalanche photodetector (APD) is a specially designed reversed biased p-i-n photodetector where the photo-generated carriers drift to a high-field region. In the high field region, the accelerated carriers undergo impact ionization, generating additional carriers, thus amplifying the signal current. Since this process has lower noise than electrical amplifiers in long-haul, high-bit-rate optical communication systems, InGaAs APDs that work at 1.3μm and 1.55μm can be used to increase the signal-to-noise ratio (SNR) and consequently the receiver sensitivity. The use of APDs also relaxes the requirements on the subsequent amplifiers in receivers. The major performance requirements for APDs in communication applications are high gain-bandwidth product, high responsivity, low excess noise, and sufficiently low dark current [1-30].

In addition to communications applications, rapidly emerging three-dimensional (3-D) near-infrared imaging applications [1-31] require focal-plane APD arrays that operate in the wavelength range between 0.8μm and 2μm. The major requirements for APD imaging arrays are high detection sensitivity, high gain uniformity, low dark currents at room temperature, and sufficient speed.

When the intensity of light is very low, the incident photons arrive as separate bursts of energy. If the average separation between incoming photons at such low light level is longer than the time resolution of the detector, a digital

response is generated for individual photons. At this low light level, digital detection of photons is better than analog signal measurements for high detection efficiency, low noise, and greater stability. This is often referred to as single photon counting [1-32]. Recently, infrared photon counting detectors have received increased attention due to the emergence of applications such as quantum cryptography, optical network testing, three-dimensional imaging, recombination kinetics studies in indium-based semiconductors, and optical time domain reflectometry (OTDR) [1-33]-[1-35]. 1.3μm and 1.55μm wavelengths are of special interest due to the low loss and small dispersion in optical fibers at these wavelengths. 1.55μm is the eye-safe wavelength and thus attractive in applications such as atmospheric monitoring and eye-safe range finding [1-36]. Novel applications such as non-destructive IC debugging and failure analysis tools have also been developed using single photon counters [1-37].

InGaAs APDs have been widely studied for infrared single photon counting [1-38, 39]. Compared to photomultiplier tubes (PMTs), APDs are compact, have lower operating voltages and cost less. They are also good candidates for fabricating arrays for applications such as 3-D LIDAR imaging and spatially resolved detection of fluorescence decay [1-40]. Most importantly, their IR detection efficiencies are far superior to PMTs, which making them very attractive at optical communication wavelength. However, challenges still exist

for reducing dark counts and trap related phenomena at the single photon level [1-32].

1.3 Thesis organization

The applications for analog fiber-optic links set challenges for increasing the operating optical power level of photodetectors. The development of communication systems, imaging and photon counting also establish new requirements for APDs. The motivation of this dissertation is to find new approaches for improving the performance of photodetectors to meet these challenges and requirements.

Chapter 2 describes in detail the high-speed photodetector fabrication and characterization techniques used in this work. Chapters 3 through 6 discuss high-output-power photodetectors for analog optical links. A detailed analysis of photodiode saturation mechanisms under large signal modulation is presented in Chapter 3. Based on this analysis, improved uni-traveling-carrier photodiodes for different frequency ranges are designed. Their measured characteristics are also discussed in this chapter. In order to fully utilize the high power capabilities of the photodetectors to improve system performance, laser RIN must be suppressed using balanced detection. A high power balanced photodetector is demonstrated in Chapter 4 for this purpose. Chapter 5 presents an evanescently-coupled short-

multimode waveguide photodiode structure to increase the responsivity of the high power balanced photodetectors. In Chapter 6, a gold wafer bonding method is used to improve the heat conduction of the high power photodiodes. This device structure also shows improved responsivity. Chapter 7 is devoted to a novel APD structure with an undepleted absorber, including both theoretical analysis and experimental studies. The potential applications of this new APD structure in communication and photon counting applications are also discussed. Finally, the work in this dissertation is summarized in Chapter 8. Some of the ideas for future work are also proposed.

Chapter 2: Photodiode Fabrication and Characterization

2.1 Introduction

This chapter describes the processing and measurement techniques that were used to fabricate and characterize the photodetectors in my research program.

Section 2.2 describes the process technology that was used in the fabrication of high-speed high-saturation-current photodiodes, avalanche photodiodes, and waveguide photodiodes. The level of processing complexity required depends on the sophistication of the tests performed on the finished device. A normal incidence high-speed photodetector (high-power photodiode or APD) requires a full-scale device fabrication process which includes p-metallization, p-mesa etch, passivation, n-mesa etch, n-metallization, deposition of contact pads, p-contact via opening, and air-bridge electroplating. A waveguide photodiode requires two more steps: planarization and V-groove etching. A full-scale fabrication of devices from an as-grown epitaxial wafer is usually time consuming, and any glitch during the process results in device degradation or device failure. Therefore, it is advisable to perform simple DC measurements before full-scale fabrication. An adequate test device may be fabricated simply by p-metallization, p-mesa etch, passivation, and n-metallization.

Section 2.3 describes the characterization methods used in this work. This includes current-voltage, capacitance-voltage, impedance, speed, saturation output power, quantum efficiency, excess noise, and sensitivity measurements.

2.2 Photodiode fabrication

2.2.1 P-metallization

Good p-metallization is critical for high-speed InGaAs photodiodes, because the major part of the series resistance comes from p-type contact. To achieve a good p-type ohmic contact, the metal is usually deposited on a very highly-doped ($>10^{19}cm^{-3}$), thin InGaAs p-contact layer. A Ti(200Å)/Pt(400Å)/Au(1000Å) contact on this type of surface provides low contact resistance and excellent adhesion. The titanium is used for adhesion. The platinum prevents gold migration into the semiconductor, which can form gold spikes that short the device [2-1]. A AuZn alloy can be used to reduce the contact resistance of materials that resist ohmic contact formation. This contact is usually annealed to allow Zn to diffuse into the material to form a very highly doped p-layer. Mn/Au can also be used to achieve very low contact resistance, if the subsequent processing steps do not require high temperatures, because this contact will degrade very quickly at temperatures higher than 300°C.

The p-metallization process started with a solvent cleaning, which includes rinsing in acetone, isopropanal (IPA) / methanol, de-ionized water (DI) and blowing dry with nitrogen. Contact openings were made using photoresist before the e-beam evaporation. The commonly used photoresist was AZ5214. The photoresist was spun on the wafer at 4000 rpm for 40 seconds, and the wafer was soft-baked at 90°C for 10 minutes. After being carefully aligned to the mask on a Karl-Suss mask aligner, the wafer was exposed approximately 0.8 minutes under UV illumination. The development took about 30 seconds in AZ726 solution. Then the wafer was ready to load into the chamber for e-beam evaporation.

When thick metal was required, the top contact metal was formed using a SiO_2-asisted lift-off process. A 2000Å-thick SiO_2 film was deposited immediately after the solvent cleaning. After definition of the p-metal patterns, the wafers were dipped in a buffered oxide etchant (BOE) to remove the oxide prior to metal deposition. Then the wafer was loaded into the e-beam evaporator for metal deposition. After deposition, the wafer was immersed in acetone for lift off, which includes an ultrasonic bath when needed.

If the measured contact resistance was high, the device was annealed using the standard annealing condition of 420º C for 30 sec for the p-type Ti-Pt-Au contact.

2.2.2 P-mesa etch

Either wet chemical etching or reactive ion etching (RIE) can be utilized to define *p*-mesa patterns on InP-based material systems. Etching is an important step for both high-power photodiodes and avalanche photodiodes, because low surface leakage current is important for both types of devices. For InGaAs/InAlAs, H_3PO_4:H_2O_2:H_2O (1:1:10) is the preferred wet etch solution. It yields smooth side walls and a well-controlled etch rate of ~0.5μm/min. For InP, Br:methanol is a good choice for its isotropic and smooth etching. When the device feature is so small that very little undercut can be tolerated, a dry etch must be used. In an RIE etching process using BCl_3:$SiCl_4$ gas mixture and an RF power of 150 W, InGaAs/InAlAs layers are etched at a rate of ~0.1μm/min. A dry etch recipe using CH_4: H_2:Ar has also been developed for InP etching [2-2].

When Br:methanol was used, a ~1000Å SiO_2 mask was used instead of a photoresist mask, since the solution attacks photoresist. In this case, SiO_2 was first deposited after the p-metallization. Adhesion promoter was used on SiO_2 surface before deploying the photoresist. Otherwise, the photoresist detached easily after development. After a standard lithography process was used to form a p-mesa photoresist pattern on top of the SiO_2 layer, the wafer was baked at 120°C for 20 minutes in order to suppress an excessive undercut in the photoresist mask during the following buffered-oxide-enchant (BOE) etch of SiO_2. It took approximately

20seconds to etch through 1000Å of SiO_2. Because the lateral undercut was intolerable if the BOE etch was too long, it was important to stop immediately after the SiO_2 window was completely opened. After removing the photoresist, the underlying SiO_2 layer was used as a p-mesa mask. For the device structures that did not have an etch-stop layer, the etch rate had to be calibrated carefully using an alpha step profiler. Br:methanol etching is diffusion limited and always leaves trenches along the mesa edge [2-3]. This could be a problem for high power photodiodes, since it increases the n-layer lateral resistance. In order to reduce the trench depth, a dry etch was used to decrease the total thickness to be etched by Br:methanol.

2.2.3 Passivation

After mesa etching, a passivation step is necessary to terminate the dangling bonds at the mesa edge and protect the sidewall of the photodiode. This can reduce the surface leakage current and prevent the photodiode from early degradation. A standard passivation was performed in a plasma-enhanced chemical vapor deposition (PECVD) chamber by depositing a thin layer of silicon dioxide. The samples were loaded into the PECVD chamber immediately after mesa etching and cleaning. A 2000Å-thick silicon dioxide film was sufficient to meet most mesa passivation requirements.

2.2.4 N-mesa etch

High-speed devices require semi-insulating substrates to avoid the excessive capacitance formed between the p-contact pads and the substrate. Consequently, an epitaxial n-type contact layer, which is normally heavily doped to minimize the n-contact resistance, must be removed from beneath the contact pad area. For this purpose, a second mesa etch was performed to etch down to the semi-insulating substrate to remove the n-contact layer area. After finishing n-mesa pattern definition using standard photolithography, a BOE etching step was used to remove the exposed SiO_2. As the n-mesa is relatively large, a short chemical wet etch is quite adequate to remove the n-contact layer.

2.2.5 N-metallization

Similar to the p-metallization process, n-contact openings were made using a photoresist lithography step before the e-beam evaporation. The n-metal contact usually consisted of Ni(100Å)/AuGe(400Å)/Au(1000Å) on top of a highly doped n-type epitaxial surface. This recipe provided low contact resistance and good adhesion to the wafer surface. After n-metal formation, a standard lift-off process was used, and the wafer was annealed in the RTA at 420°C for 20s. A good n-contact is relatively easy to form on the InP material system. The typical specific contact resistance, which was obtained by on-wafer TLM (transfer length method) pattern measurements, was far below $1\times10^{-6}\ \Omega cm^2$.

2.2.6 Contact pad deposition

It is not advantageous to deposit the contact pads directly on top of the semi-insulating substrate, because leakage current through the substrate is not-negligible. Therefore, after the second mesa etching, a new layer of SiO_2 was deposited on the wafer. After n-metallization, contact pads were made on top of this SiO2 isolation layer using a photoresist lift-off process and e-beam evaporation. The metal used for the contact pads was Ti(200Å)/Au(800Å). Ti was used to provide good adhesion to the SiO_2 surface. The leakage current between the pads deposited on this SiO_2 layer was very low.

2.2.7 P-contact via opening

At this point, there was a layer of SiO_2 on top of the p-metal. In order to connect the p-metal to the p-pad, it was necessary to open a via in the SiO_2 on top of the p-metal. Since the p-mesa for the high-speed devices is small, the lithography and the BOE etching for the via opening had to be handled very carefully to prevent damage to the SiO_2 passivation layer on the photodiode mesa sidewall.

2.2.8 Air-bridge electroplating

The final step of the full-scale high-speed photodiode processing is to connect the deposited contact pads and ohmic-metals using an air-bridge interconnect technique. The fabrication of the air-bridge consisted of two metal processes. Each process had its own mask. In the first lithography step, the first

mask was used to define the pier area (n-metal, p-metal via, and contact pad openings) of the air-bridge. The photoresist on these areas was removed by developing. Then e-beam evaporation was used to deposit Ti(200Å)/Au(300Å) as a seed layer on top of the wafer. Without removing the first layer of the photoresist, a second layer of photoresist was spun onto the wafer. A second lithography was then used to remove the second layer of photoresist in the bridge area (between n-metal and n-pads, p-metal and p-pads). The samples were then electroplated in a MICROFAB AU-100 gold-plating solution, which was obtained from Enthone-OMI Inc. In the electroplating, the device was connected to the cathode and a gold mesh was connected to the anode. The electric current was set at 2mA. The time of the plating process varied according to the amount of gold area exposed. It usually took 10 minutes to plate a 1.5μm-thickness of gold on a $1cm^2$ wafer. After the electroplating step, the device was ready for the final lift-off. The two photoresist layers together with the thin metal seed layer sandwiched in between were lifted off in an acetone solution. An ultrasonic bath was helpful during the lift-off process. A finished high-speed APD device, with the above full-scale processing, is shown in Figure 2.1 [2-4].

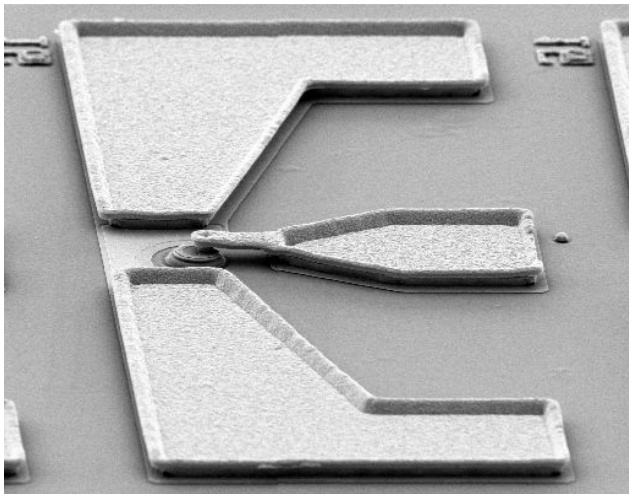

Figure 2.1 SEM picture of a finished normal incidence high-speed photodiode with air-bridge interconnects [2-4]

2.2.9 Waveguide photodiode related processing

Most steps in the fabrication process of waveguide photodiodes are the same as the normal incidence devices. The two additional processing steps required for waveguide photodiodes are described in this section.

A. Planarization

In an evanescently coupled waveguide photodiode structure (refer to Chapter 6), there are waveguide layers and optical matching layers below the n-contact layer and above the semi-insulating substrate. These layers are about 3μm thick in total. They all need to be etched through in the second mesa etching process to avoid excessive parasitics. After this etching, a step of approximately 3μm or higher will be formed around each device on the wafer. Photoresist can

not uniformly and completely cover the corners and edges of such high steps. This was a problem for the following processing steps, which usually require a planarization step to address this problem.

The planarization was done using polyimide. It was usually spin-coated on the sample, and the film thickness was controlled by the rotation speed. Openings in the polyimide film were formed by direct photolithography if the polyimide was photosensitive. The sample was then cured in several steps to harden the film. The curing procedure was quite different for different types of polyimide and can be found in the manual.

B. V-groove

In order to achieve good responsivity in multimode waveguide photodiodes (Chapter 6), the waveguide length has to be controlled very accurately [2-5]. This requires waveguide cleaving with accuracy on the order of a few microns. Deep etched grooves defined by photolithography on the wafer can serve as accurate cleaving marks for this purpose.

Since HBr etches InP anisotropically, a V shaped groove is formed on the InP wafer by HBr etching along a specific crystal orientation. This orientation was determined by a test etch before the start of the photodiode process. The pattern used to define the etching area is 50μm wide and 500μm long. The etching rate of HBr on InP is about 3μm/min. After ~10 minutes of etching, a 25μm deep

V-groove, with the valley in the center of the pattern, was formed on the wafer. After the photodiode fabrication, the wafer was cleaved by applying pressure on the V-groove. The cleave line occurs at the center of the V-groove pattern.

Figure 2.2 is a picture of a fabricated balanced waveguide photodiode. The polyimide planarization layer and the V-grooves can be seen from the picture. The device structure and performance will be discussed in Chapter 6.

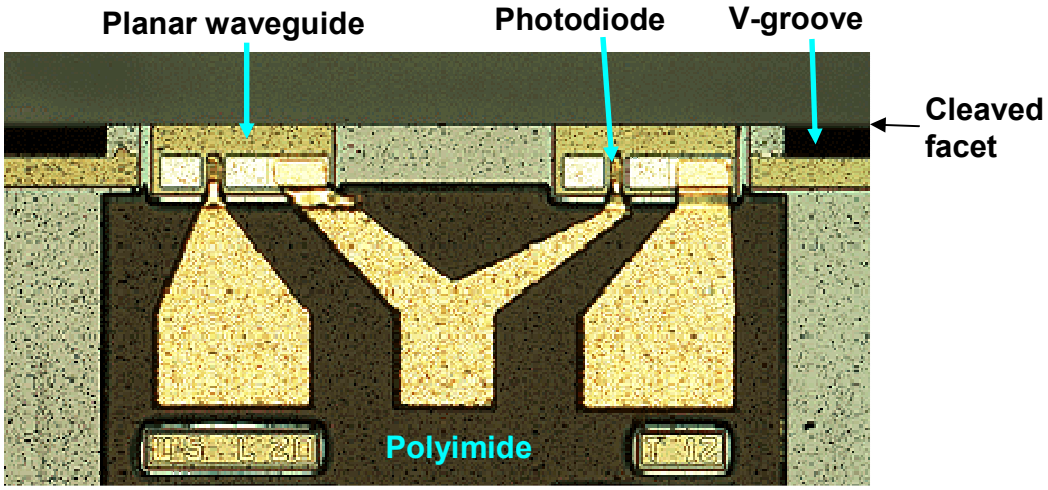

Figure 2.2 Microscope picture of fabricated balanced waveguide photodiode

2.3 Photodiode characterization

2.3.1 Current-voltage and capacitance-voltage characteristics

DC current-voltage (IV) measurements were conducted using a probe station and an HP4145B semiconductor parameter analyzer. Specific contact

resistance and the sheet resistance were calculated based on IV measurements on TLM (transfer length method) patterns. The photocurrent was generated using white light from a microscope lamp. The capacitance-voltage (CV) characteristics of the photodiodes were measured using the same probe station and an HP4275A LCR meter.

2.3.2 Impedance measurement

An Agilent 86030A Lightwave Component Analyzer (LCA) was used to measure the photodiode impedance. The setup is shown in Figure 2.3. A microwave cable, a high-speed bias tee, and a high-speed microwave probe were connected to one of the electrical ports of the LCA. Then the standard open, short and 50Ω load calibrations were conducted using the calibration kit. After the calibration, the photodiode was probed using the microwave probe. A DC reverse bias was applied on the photodiode through the bias tee. The LCA measured the reflection coefficient of the photodiode under test at reverse bias voltage. The impedance of the device can be read from measured data on a Smith Chart. This measurement is useful to determine the series resistance and the total capacitance of the photodiode. This permits the RC-limited bandwidth to be calculated.

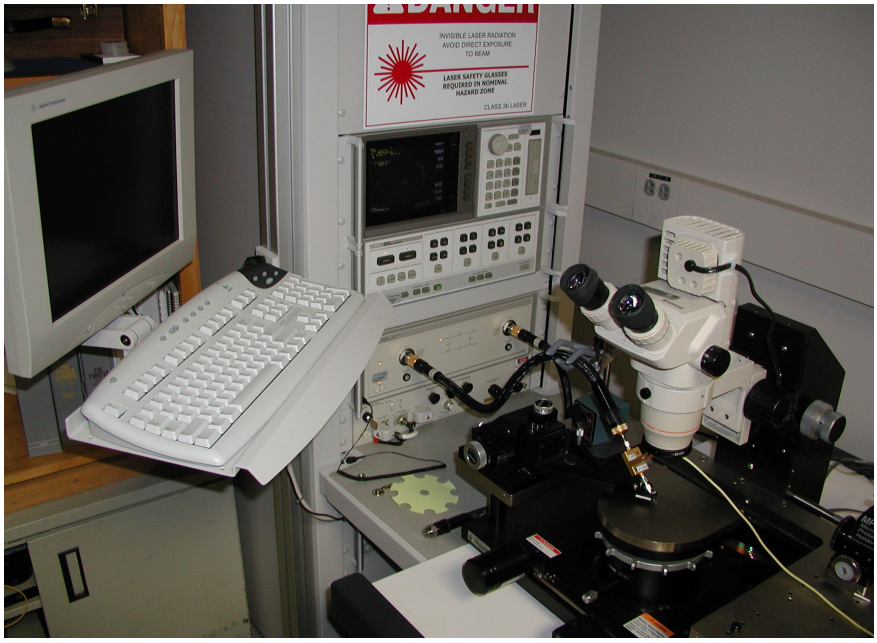

Figure 2.3 Photodiode impedance measurement setup

2.3.3 Speed measurement

Frequency response and saturation power of the photodiodes were examined using the optical heterodyne setup shown in Figure 2.4. In the setup, two DFB lasers were optically mixed to provide a heterodyned RF optical signal. The wavelengths of DFB lasers were 1543.58nm and 1543.60nm, respectively, at 25 C. The linewidth was a few MHz. The frequency of the lasers was tunable over a wide frequency range (>100GHz) by tuning the temperature. In order to achieve 100% modulation depth, the output power of the two DFB lasers were matched using current controllers. The beat frequency was swept from 0 to 50GHz by tuning the temperature of one of the lasers.

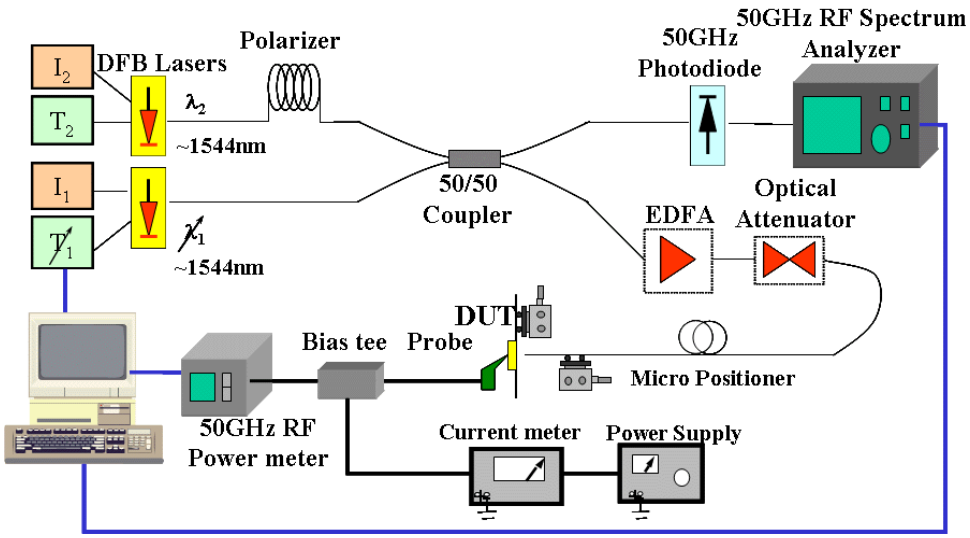

Figure 2.4 Optical heterodyne setup used to measure the frequency response and saturation power

The output polarization of the two lasers needs to be the same to provide a beat signal. A polarization controller is used at the output of one of the lasers to make sure that the polarizations are aligned when the two signals are combined in the coupler. The mixed optical signal was then split into two arms. In one arm, this beat frequency was measured with an NEL 50GHz photodetector and an HP 50GHz spectrum analyzer. In the other arm, the heterodyned optical signal was amplified by an Erbium-doped fiber amplifier (EDFA) and focused onto the photodiode under test (DUT), which was probed with a microwave probe. The DC power supply and current meter were connected to the photodiode through a bias tee. The RF output of the photodiode was measured with an Anritsu 50GHz RF power meter.

2.3.4 Saturation power measurement

The saturation behavior of high power photodiodes was measured using the same setup shown in Figure 2.4. Large signal modulation (~100% modulation depth) is used in the measurement. In order to achieve 100% modulation, the output power of the two DFB lasers were balanced using the current controller. EDFAs with 300mW saturation output power and 2W saturation output power were used in the measurement. An optical attenuator was used to tune the optical power incident on the photodiode under test.

When the photodiode bandwidth is much larger than the beat frequency, the current generated in the photodiode can be can be expressed as

$$i_{RF}(t) = I_{DC} + I_{DC} \cdot \cos(\omega t) \qquad (2.1)$$

Where, t is time, $i_{RF}(t)$ is the transient current, and I_{DC} is the average DC current. The second term (AC term) is delivered to the load. The RF power dissipated on the load can be calculated as

$$P_L = \frac{1}{2} \cdot {I_{DC}}^2 \cdot R_L \qquad (2.2)$$

where P_L is the load RF power, and R_L is the load impedance.

The ideal relation of the RF power on the load is plotted in Figure 2.5. The thick line shows the calculated RF power delivered to the 50Ω load versus the photodiode DC current at frequencies much smaller than the photodiode 3dB roll over frequency. The thin line shows RF output power values at the photodiode

3dB roll over frequency. These values can be used to calibrate the heterodyne setup and determine the point where the RF output power saturation occurs in the measurement.

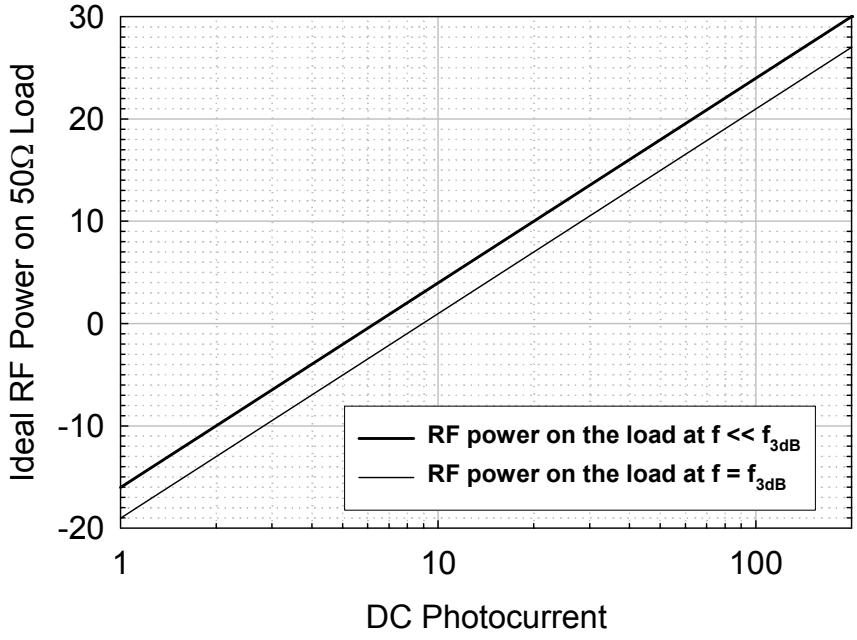

Figure 2.5 The ideal relation between the RF power delivered to the 50Ω load and the photocurrent when the incident optical signal is 100% modulated.

2.3.5 Quantum efficiency measurement

The quantum efficiency was measured using a tungsten-halogen light source, a spectrometer, and a lock-in amplifier. The light source was chopped at a frequency of ~200Hz and the photocurrent was detected using a Stanford

Research SR850 lock-in amplifier. The position of the device under test (DUT) should be carefully adjusted to obtain maximum photoresponse. Then, at a specific reverse bias voltage, the photocurrent was measured in the wavelength range of interest. Without changing the optical path for the measurement, a calibrated germanium photodetector was inserted and the photocurrent was maximized by adjusting the device position. The photocurrent was measured in the same wavelength range used for the DUT. The photocurrents of the DUT and the Ge detector were compared, and external quantum efficiencies of the APD were derived from the calibrated external quantum efficiencies of the Ge photodetector using the following expression

$$\eta_{ext,DUT} = \frac{I_{ph,DUT}}{I_{ph,Ge}} \cdot \eta_{ext,Ge} \qquad (2.3)$$

2.3.6 Excess noise measurement

The excess noise measurement was performed using a HP8970 noise figure meter. The noise signal was amplified with a low noise amplifier and then fed into the noise figure meter. The center frequency value (normally 30MHz) of the HP8970 was chosen so that ambient noise was minimized. A Santec laser with an output wavelength near 1.55μm was used as the optical input. A high resolution Keithely current meter was utilized to measure both photo and dark currents, while a high-resolution digital voltage source was used to provide an accurate device bias.

Chapter 3: High -Power Improved Uni-Traveling-Carrier Photodiode

3.1 Introduction

As discussed in the first chapters, for both digital and analog optical transmission systems, photodetectors that can operate at high power levels are becoming increasingly important. Especially in analog optical links, such as, wireless base stations, phased array antennas, cable televisions and photonic signal processing systems, the demand of high RF output power is unlimited. In this chapter, factors that limit the output RF power from the photodiode will be discussed. This is followed by a description of two improved uni-traveling-carrier photodiode structures. The experimental results will also be presented and analyzed.

3.2 Analysis of photodiode saturation under large signal modulation

There are two methods that are commonly used to measure saturation current. One is small signal modulation (modulation depth <5%), and the other is large signal modulation (modulation depth ~100%). The saturation current determined by the small signal measurement is mainly limited by the space charge effect, but is ultimately limited by thermal failure at elevated bias voltage. In this

kind of measurement, the AC current and the RF power delivered to the load are small. When the photodiode maximum output RF power needs to be measured, the large signal modulation technique is used. Under large signal modulation, the loading effect is taken into account. In this section, the discussion focuses on calculating the saturation current under large signal modulation.

3.2.1 Influence of beam spot size

With a Gaussian beam incident on a circular photodiode, the generated carrier density has the same lateral Gaussian distribution, which is high near the center and lower at the edge. The lateral diffusion of the carriers is negligible during the time required for carrier transport. Figure 3.1 shows the trade off between the coupling efficiency and the peak current density in a photodiode. When the beam spot size (R_{beam}) is small compared to the device size (R_{device}), the coupling efficiency is high, but the peak current density is high too. In this case, the device is easy to saturate due to the high space charge density. If the beam spot is diluted to a larger diameter, the peak current density is lower, but some of the light will be lost. By expanding the Gaussian beam such that 10% of the light misses a circular absorbing region, the current density in the center of the device can be significantly reduced [3-1]. Hence, in the measurements reported in this dissertation, the beam spot was always diluted to have a more uniform beam size at a coupling efficiency of approximately ~90%.

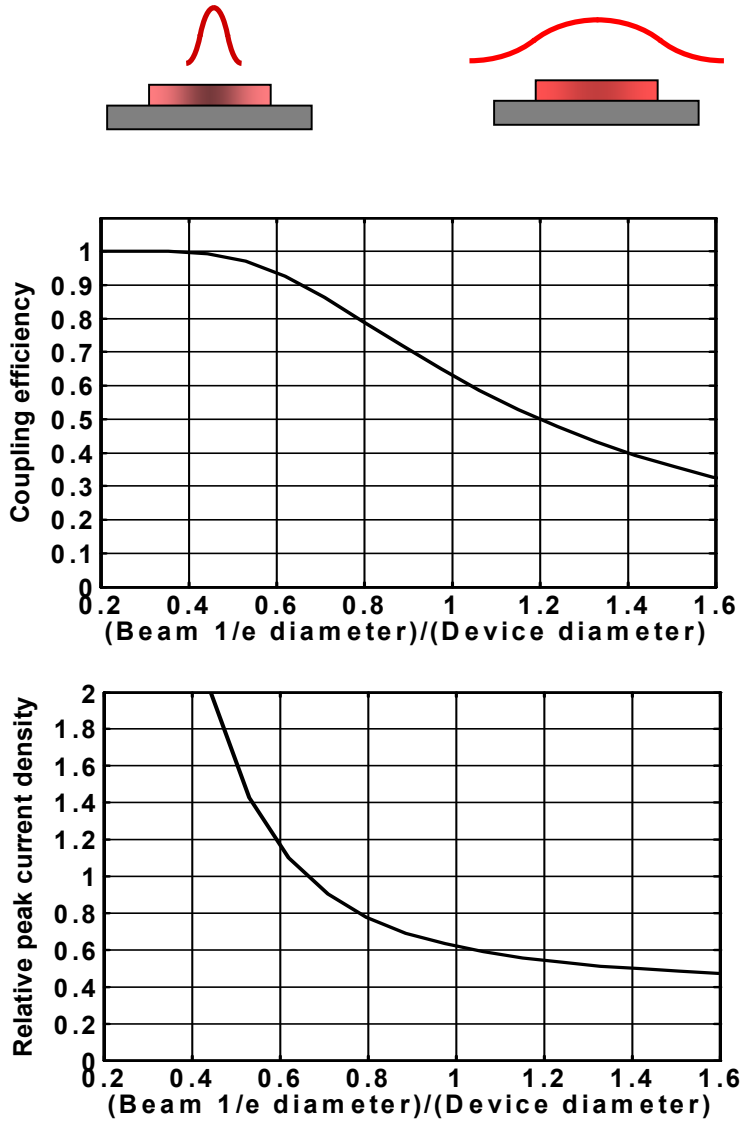

Figure 3.1 Influence of beam spot size on coupling efficiency and current density

3.2.2 Calculation of space charge density

Figure 3.2 shows the calculated peak space charge density versus photodiode transient current for the coupling condition described above for UTC

photodiodes with various areas. For 100% modulation depth, at an average photocurrent of 80mA, the peak transient current is 160mA. The peak current density is calculated to be 420kA/cm^2 and 210kA/cm^2 for 100μm^2 and 200μm^2 photodiodes, respectively. Assuming an electron overshoot velocity of 2×10^7cm/s, the peak space charge densities are 1.3×10^{17}cm^{-3} and 6.5×10^{16}cm^{-3}.

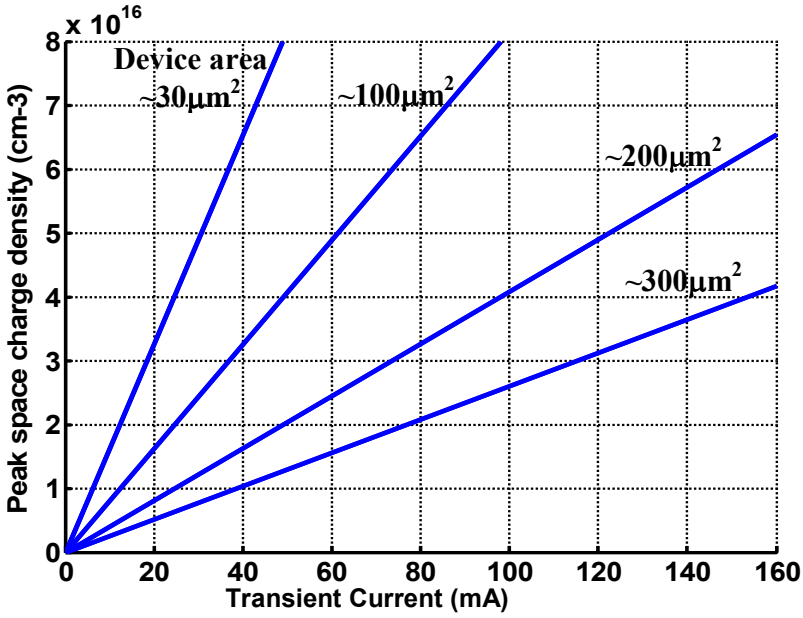

Figure 3.2 Calculated space charge density versus transient photocurrent for InGaAs/InP UTC photodiodes of different areas

3.2.3 Loading effect

The space charge effect and thermal failure are the main limiting factors for current saturation in a photodiode operating in the small signal case. However, for the large signal case, when large RF power is delivered to the load, the load

voltage swing plays a very important role in determining the photodiode saturation current.

Figure 3.3 shows a simulation of the influence of the load voltage swing at different frequencies. Figure 3.3(a) is the equivalent circuit of a high power photodiode connected to a 50Ω load. A DC bias voltage is applied to the photodiode. In AC operation, the photodiode is in parallel with the 50Ω load. The voltage swing induced by the AC current delivered to the load will be superimposed on the photodiode bias. In the case of small signal detection or small signal measurement of saturation current, this voltage swing is negligible compared to the DC bias. Under large signal operation, however, when the AC current on the load is very high, the superimposed DC and AC bias has to be considered. Figure 3.3 (b) shows the photodiode total bias versus the photodiode transient current at different frequencies. In the calculation, the DC bias is 4V, the average photocurrent is 80mA, the modulation depth is 100%, and the load is 50Ω. The series resistance of the photodiode is considered negligible here.

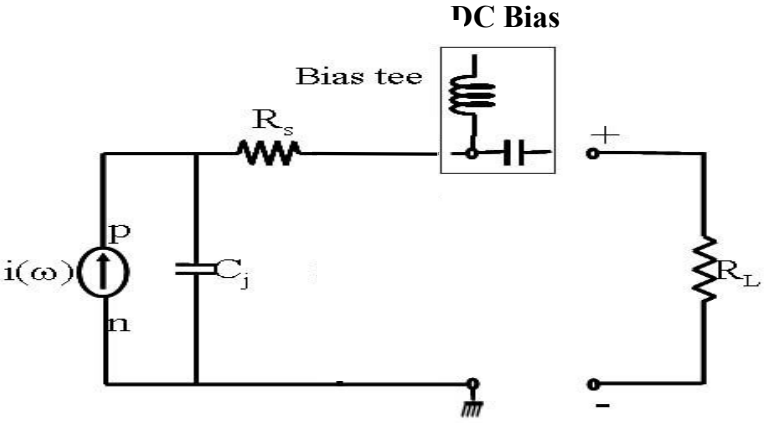

(a)

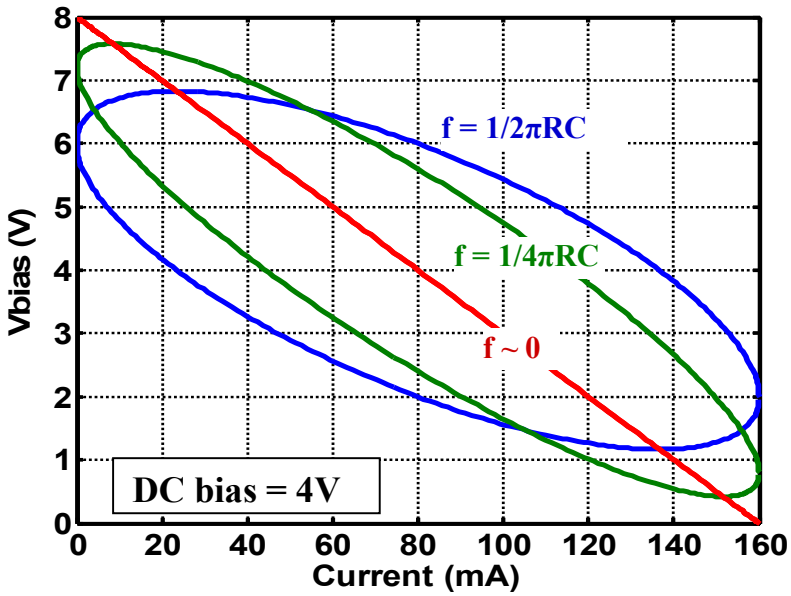

(b)

Figure 3.3 (a) Circuit model of the photodiode in operation, and (b) photodiode transient bias at various frequencies versus transient current under large signal modulation

It is clear that at this high current level, the voltage swing occupies a significant amount of the device bias. At low frequencies close to DC, the voltage swing is high, because there is no RC induced loss. The load line is a straight line, because there is no phase difference between the conduction current on the photodiode and the AC current delivered to the load. At high frequencies, the voltage swing drops due to RC induced RF power loss on the load. The load line becomes elliptical, because there is a phase difference between the conduction current on the photodiode and the AC current delivered to the load.

3.2.4 Series resistance

Any resistance in series with the photodiode can induce a voltage drop at high current levels. The presence of this resistance will cause the photodiode to saturate early. This series resistance usually includes the lateral resistance in the doped semiconductor layers and the contact resistance between the semiconductor and the metal. The p-layer lateral resistance is much larger than the n-layer lateral resistance due to small hole mobility. In the top illumination structure (p-layer is on top), the p-layer lateral resistance can be large enough to dominate the saturation of the photodiode [3-2]. Using back side illumination, the p-layer lateral resistance can be made negligible because the contact covers the whole p-layer.

3.2.5 Determination of saturation current

The saturation current under large signal modulation can be determined by considering the mechanisms discussed above [3-3]. Since electron velocity decreases when the electric field gets below 10kV/cm, the required bias voltage to operate without saturation can be calculated as

$$V_{req} = V_{pounch-through} - V_{built-in} + 10kV/cm \times D_{dep}$$

where $V_{pounch\text{-}through}$, $V_{built\text{-}in}$ and D_{dep} are the space charge punch-through voltage, photodiode built–in potential and depletion layer thickness, respectively. This photodiode required bias voltage versus the average photocurrent for large signal modulation for several different UTC PD structures is plotted in Figure 3.4.

As discussed above, in a large-signal measurement, the AC voltage swing will modulate the device bias. In order for a photodiode to operate without saturation, the bias on the photodiode must exceed the required bias at all times. The photodiode is more sensitive to bias reduction at high frequencies than at low frequencies, because at low frequencies, the slower carrier speed does not affect the output RF power. At the 3dB roll over frequency, the photodiode transient bias at the peak photocurrent, $V_{pdbias,}$ can be expressed as

$$V_{pdbias} = V_{bias} - \frac{I_{ph}(50 + R_s)}{(1 + (2\pi f(50 + R_s)C_j)^2)^{1/2}}$$

where V_{bias}, I_{ph}, f, R_s, and C_j, are applied DC bias voltage, average photocurrent, signal frequency, device series resistance and junction capacitance, respectively.

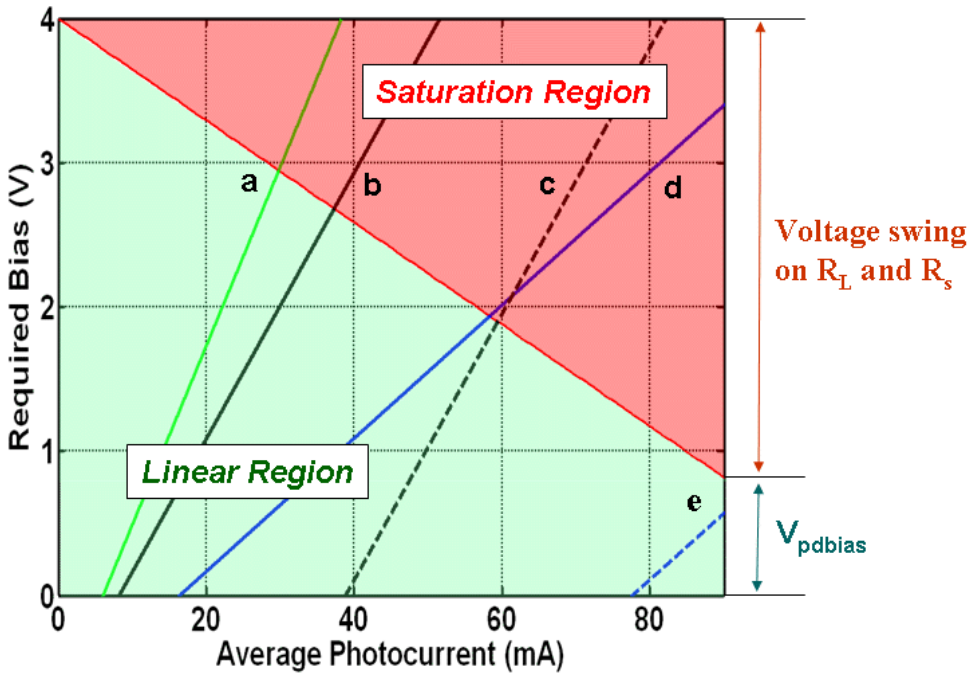

Figure 3.4 Calculated photodiode required bias voltage versus average photocurrent at 4V DC bias for various UTC photodiode structures with doping, thickness and size of (a) undoped, 290nm, 99μm^2, (b) undoped, 250nm, 100μm^2, (c) 5×10^{16}cm^{-3}, 250nm, μm^2, (d) undoped, 250nm, 200μm^2, and (e) 5×10^{16}cm^{-3}, 250nm, 200μm^2

This V_{pdbias} separates the graph into a saturation region and a linear region. When $V_{req}<V_{pdbias}$, the device operates in the linear region. When $V_{req}\geq V_{pdbias}$, the device is in the space charge induced saturation region. From Figure 3.4, the saturation current can be determined from the point where the $V_{req} = V_{pdbias}$. The calculated saturation current values for different structures will be discussed in the next section.

3.3 Charge-compensated InGaAs/InP UTC photodiode

3.3.1 Device design

It has been suggested, that the space charge suppression of the electric field could be compensated by a fixed distribution of background dopants [3-4]. By doping the depletion region, the electric field can be pre-conditioned to be higher at the location where ultimately it would tend toward zero in the presence of high photocurrent. This type of charge compensation can effectively increase the maximum photocurrent without the associated failure caused by increased thermal loading from higher bias voltages. For the UTC PDs with significant space charge density, an n-type doped InP depletion region can be used to compensate the mobile space charge and reduce the net space charge density. Figure 3.4 compares the structures with and without n-type doping in the InP depletion region. A saturation current of 30mA (a) given by this calculation is close to the reported RF power of 14dBm [3-5]. It is clear from this graph that a compensation charge density of $5\times10^{16}cm^{-3}$ can increase the large-signal saturation current of a $100\mu m^2$ photodiode from 37mA (b) to 60mA (c) and that of a $200\mu m^2$ photodiode from <60mA (d) to >90mA (e).

3.3.2 Device structure

The device structure was grown by MOCVD, on a semi-insulating InP substrate. The epitaxial layer structure is shown in Figure 3.5. The device consists

of a 600nm n^+ InP buffer layer, a 250nm depletion region, a 450nm p-type $In_{0.53}Ga_{0.47}As$ absorbing region, a 200nm p-type InP diffusion blocking layer, and a 30nm $In_{0.53}Ga_{0.47}As$ p-contact layer.

The depletion region is comprised of a 200nm n-doped InP layer, a 5nm heavily n-doped InP charge layer, two 15nm n-doped InGaAsP layers, and a 15nm un-doped $In_{0.53}Ga_{0.47}As$ layer. The two 15nm-thick-InGaAsP quaternary layers in the collection region were used to smooth the abrupt conduction band barrier at the $In_{0.53}Ga_{0.47}As$/InP heterojunction interface. A 5nm-thick S doped (5×10^{17} cm^{-3}) InP layer was used to increase the electric field in the transition region.

The doping in the p-type absorber was "graded" in three steps (5×10^{17} cm^{-3}, 1×10^{18} cm^{-3}, and 2×10^{18} cm^{-3}) to form a quasi-electric field to aid carrier transport in the absorbing layer. In the depletion region, the 200nm InP layer was S doped to 5×10^{16} cm^{-3}. The two InGaAsP transition layers were also doped to compensate the space charge. The wafer was fabricated into a backside illuminated mesa structure using conventional photolithography, wet chemical etching, SiO_2 passivation, and lift-off metallization techniques. Air-bridge connected contact pads were fabricated for RF measurements. A 220nm-thick SiO_2 film was deposited on the backside as an anti-reflection coating.

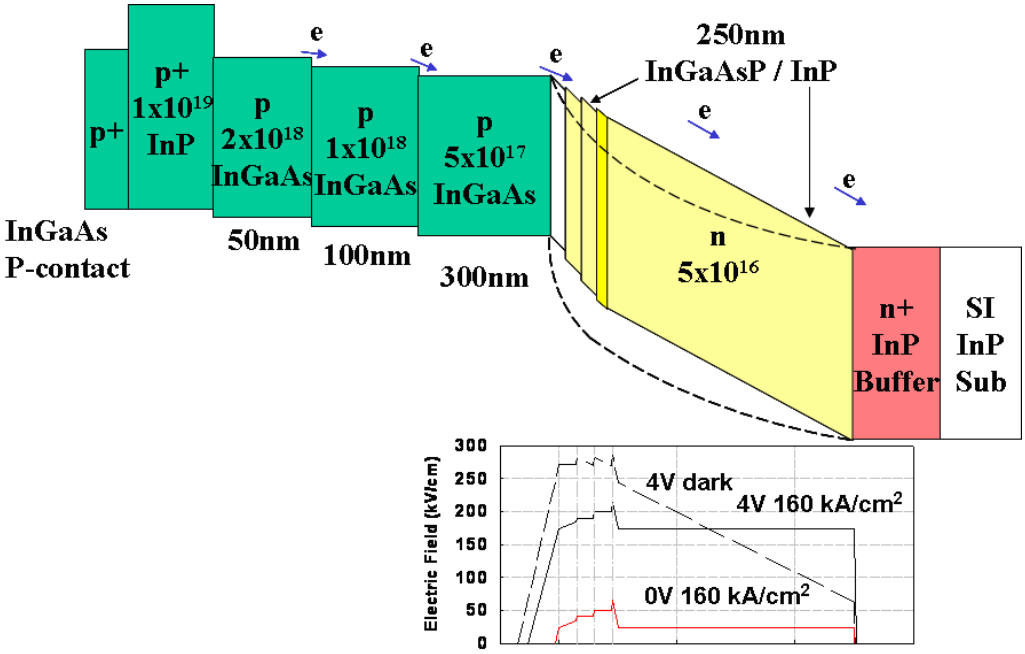

Figure 3.5 Schematic band diagram and calculated electric field for a charge compensated UTC photodiode

3.3.3 Measurement results and discussion

A photodiode with a diameter of 20μm and a smaller photodiode with an area of ~100μm^2 were characterized. The impedance of these devices was measured using a 50GHz network analyzer. The 20μm-diameter device had a series resistance of 7Ω and a junction capacitance of 113fF, yielding an RC limited bandwidth of 25GHz. The 100μm^2 photodiode had a series resistance of 12Ω and a junction capacitance of 40fF, which projects to an RC limited bandwidth of 64GHz.

Frequency response and output saturation of the photodiode were examined using large-signal modulation. Two equal-power, single-frequency DFB lasers were optically mixed to provide a heterodyned RF optical input signal, as discussed in section 2.3. Both lasers were temperature controlled; the frequency was swept by changing the temperature of one of the lasers. The heterodyned optical signal was amplified by an Erbium-doped fiber amplifier and focused onto the backside of the device. The measured responsivity of the photodiode was 0.45A/W. Assuming an absorption coefficient of $0.67\mu m^{-1}$, the theoretical responsivity of a double passed 465nm-thick absorber is ~0.56A/W. The difference between the measured and theoretical value was mainly due to the imperfect AR-coating and the top metal reflection loss. The frequency of the signal was obtained from a spectrum analyzer, while the output RF power was measured with an RF power meter. RF losses induced by the microwave probe and bias-tee were measured and normalized out [3-6].

Figure 3.6(a) shows the measured RF response of a 20μm-diameter device at different photocurrents under 4V bias. The bandwidth increases as the photocurrent increases mainly due to the self-induced electric field in the absorption region. The bandwidth is higher than 20GHz when the photocurrent is greater than 30mA, and is higher than 25GHz when the photocurrent is above 70mA. Figure 3.6(b) shows the measured output RF power versus average

photocurrent at 20GHz under 3V and 4V bias. The ideal relation between the RF power of a 100% modulated large-signal and the average current on a 50Ω load is also plotted for reference. Since the device bandwidth increases with increasing photocurrent, the output RF power is closer to the ideal line at a high photocurrent prior to saturation than at a low photocurrent. It is clear that at 4V bias, the saturation starts at ~90mA, and the maximum output RF power is ~20dBm at 20GHz. The saturation is mainly limited by the allowable voltage swing at 4V DC bias.

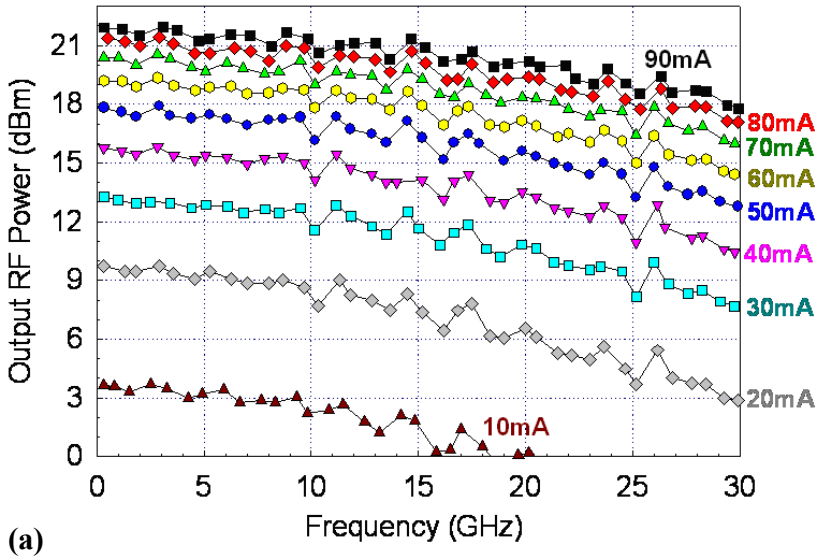

Figure 3.6 Measured (a) frequency response and (b) output RF power versus current of a 20μm-diameter charge compensated UTC-PD

Figure 3.7(a) shows the measured RF response of a 100μm^2 photodiode at different photocurrents under 4V bias. The fluctuations in the RF power originated from the reflection between the probe, the bias-tee, and the RF sensor head. This behavior was repeated in every measurement and is not related to the photodiode. The device bandwidth is higher than 35GHz when the photocurrent is above 10mA and reaches 50GHz when the photocurrent is greater than 40mA. Figure 4.7 (b) shows the measured output RF power at 40GHz versus photocurrent under 3V and 4V bias. The 1dB saturation current is between 50 and 60mA and the maximum output RF power is ~17dBm at 40GHz.

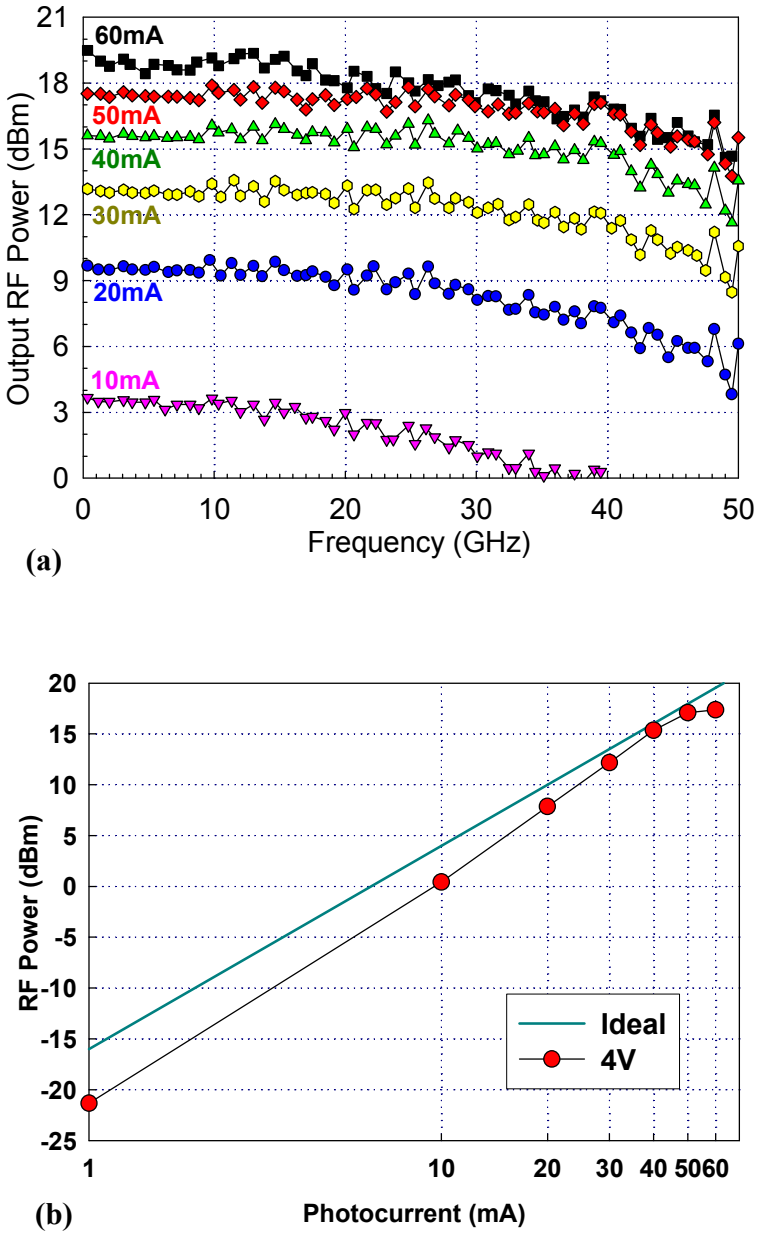

Figure 3.7 Measured (a) frequency response and (b) output RF power versus current of a 100μm^2 charge compensated UTC-PD

Figure 3.8 shows the measured photodiode bandwidth versus the photocurrent. When the current exceeds 50mA, in the 100μm^2 device, the current density is so high that the space charge induced saturation becomes significant and the bandwidth decreases. At a bias below 4V, the large-signal saturation current in the 20μm-diameter photodiode is limited by the output voltage swing, which modulates the device bias. In this case, there are two effects that cause the RF power to be compressed more at low frequencies than at high frequencies. First, the voltage swing at low frequencies is higher than at high frequencies, because the RF power at low frequencies is higher. Second, the AC current and the AC voltage on the photodiode are anti-phase (180° out of phase) at low frequencies, but only 135° out of phase at the RC limited 3dB drop frequency. Therefore, the bandwidth of the photodiode shows a slight increase after saturation.

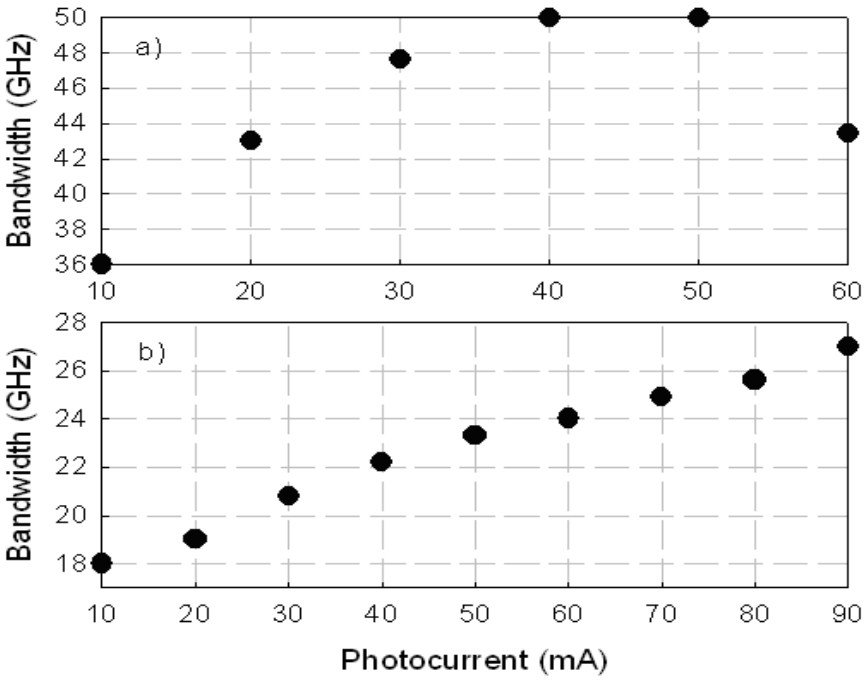

Figure 3.8 Measured photodiode bandwidth versus photocurrent for (a) a 100μm^2 photodiode and (b) a 20μm-diameter photodiode under 4V bias

3.4 Uni-traveling-carrier photodiode with thick depletion region

3.4.1 Device design

Figure 3.9 shows the required photodiode bias versus the average photocurrent for devices with different RC limited bandwidths. For the devices with large area and low RC limited bandwidth (the 6GHz devices), the space charge density and the photodiode required bias are still very low, when saturation occurs. Almost all of the bias voltage was used to balance the load

voltage swing. Very little bias is needed to overcome the space charge effect in the photodiode. For these large devices, the output RF power is limited by the allowable total voltage swing, which is limited by the highest DC bias voltage. In order to increase the DC bias, we need to suppress the dark current at higher bias and improve the photodiode heat handling capabilities to allow higher power dissipation.

These observations lead to the conclusion that a photodiode with a thicker depletion region is preferable for two reasons. First, the breakdown voltage and the voltage at which the tunneling component of the dark current becomes significant will be higher for a thicker depletion region. This would allow the photodiode to be biased at higher DC bias, while maintaining a low dark current. Second, with the same RC limited bandwidth, a thicker depletion region photodiode will have a larger area. According to a thermal model, this geometry will also exhibit better heat conduction to the substrate. This will allow the photodiode to dissipate more heat for the same temperature increase, thus postponing the thermal failure to a higher level of total dissipated power.

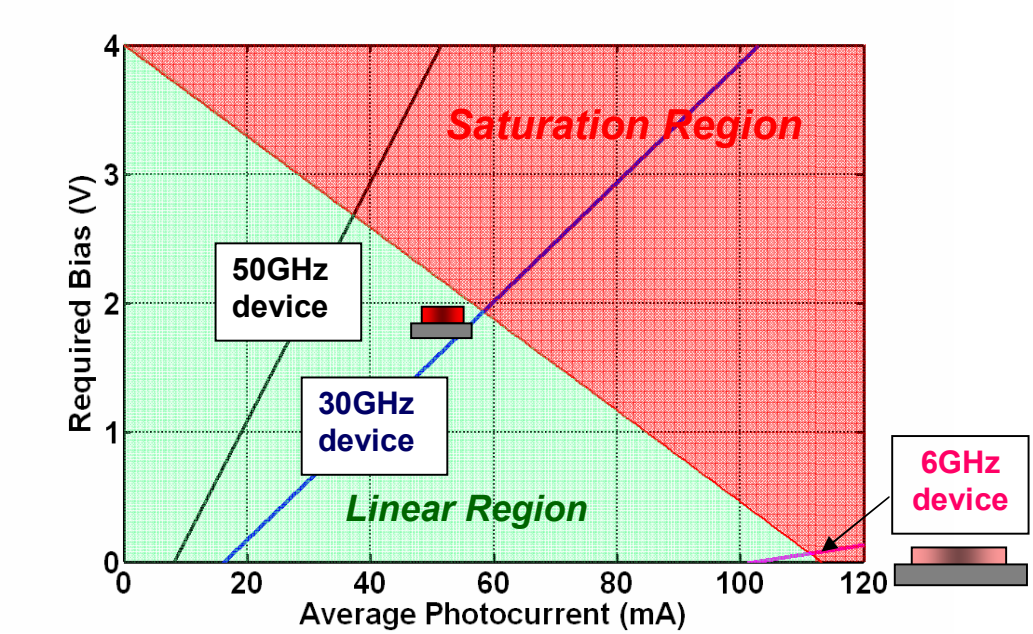

Figure 3.9 Bias voltage required to overcome space charge effect versus the average photocurrent under large-signal modulation for UTC PDs with different RC limited bandwidths. The InP depletion layer thickness used in the simulation is 250nm

3.4.2 Device structure

A wafer with a thick depletion region was designed, as shown in the layer structure in Figure 3.10. The depletion region of a UTC photodiode is usually made thinner than 300nm in order to reduce the carrier transit time. For this wafer, optimization for a lower bandwidth called for a depletion region thickness of 500nm.

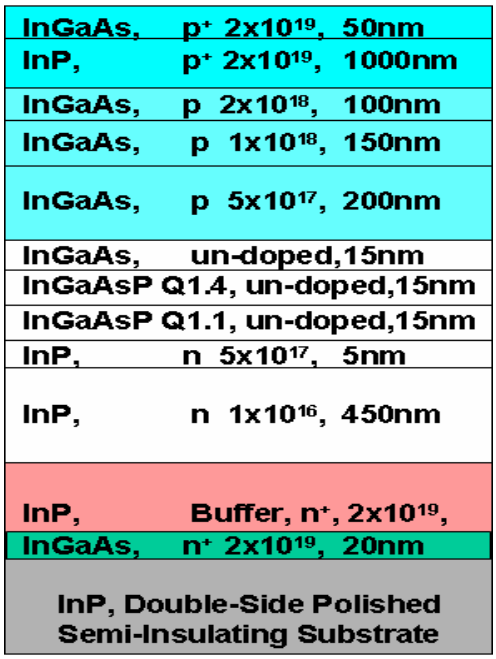

Figure 3.10 Layer diagram of the UTC Photodiode with thick depletion region

3.4.3 Measurement results and discussion

Figure 3.11 shows the dark current comparison of photodiodes fabricated from this wafer and a photodiode with a 250nm InP depletion region. The onset of the tunneling current occurs at a much higher voltage for the thicker depletion region device.

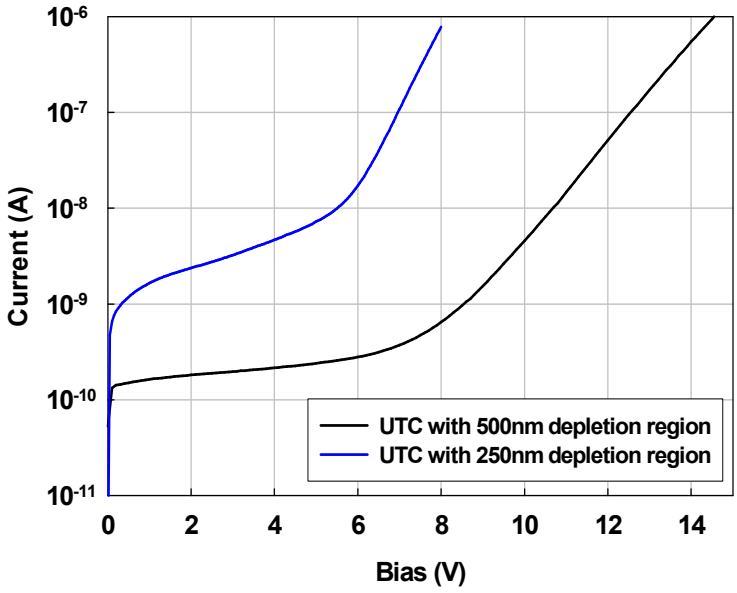

Figure 3.11 Dark current comparison of UTC PDs with thick and thin depletion region

Figure 3.12 (a) shows the comparison of the measured bandwidth of a 56μm UTC Photodiode with 500nm InP depletion region and a 40μm UTC photodiode with 250nm InP depletion region. These two devices have a similar RC limited bandwidth of ~6GHz. Figure 3.12 (b) shows the comparison of the measured output RF power saturation of these two photodiodes onto a 50Ω load both at 6V. Because of the better heat conduction, the 56μm UTC PD with a thick depletion region can achieve higher dissipated power. The maximum output power of the UTC PD with a 500nm InP depletion region was 25dBm, which is ~2.5dB higher

than the maximum output power of the UTC PD with a 250nm InP depletion region (~22.5dBm).

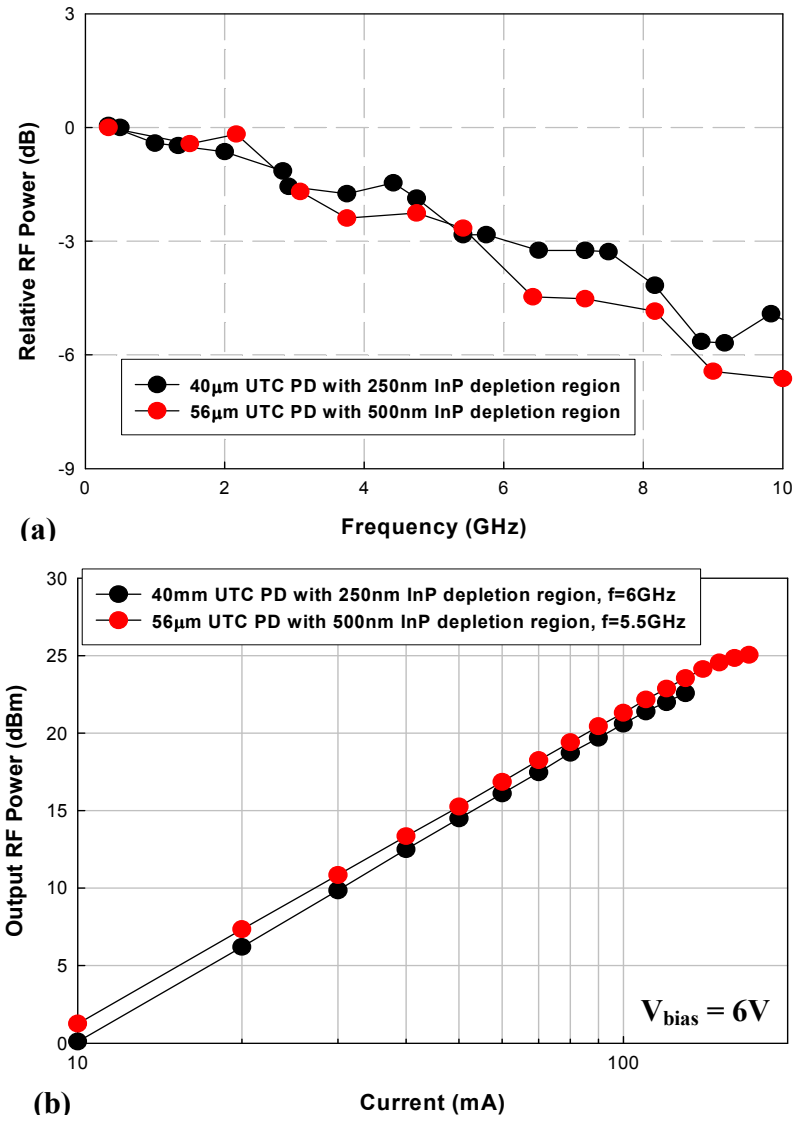

Figure 3.12 Comparison of (a) frequency response and (b) saturation output power of thick and thin depletion region UTC PDs with the same RC limited bandwidth of ~6GHz

3.5 Summary

An analysis of photodiode saturation mechanisms under large-signal modulation is discussed. A rough calculation of the UTC photodiode characteristics under large-signal saturation current is presented. Although this calculation is not intended to provide high precision, the primary limiting factors for the photodiode saturation can be identified. This is used as a guide to improve the design of photodiodes in order to achieve high RF output power.

Based on this analysis, two types of improved UTC photodiodes were designed and experimentally studied. The charge compensated UTC photodiode delivered 20dBm at 20GHz and 17dBm at 40GHz; a UTC photodiode with a thick depletion region delivered 25dBm at 6GHz, all record high output RF power values for the respective frequencies.

Chapter 4: High-Power Balanced Photodetectors

4.1 Introduction

High-power photodiodes are crucial components in analog optical links for applications, such as cable television, phased array antennas, and photonic analog-to-digital converter systems. The link performance, which includes link gain, noise figure, and spurious free dynamic range, can be improved by increasing the power of the optical carrier [4-1]. However, as the optical power level increases, the relative intensity noise (RIN) of the laser source and the amplified spontaneous emission noise (ASE) from the erbium-doped fiber amplifiers (EDFAs) will become dominant, setting an upper limit on the signal-to-noise ratio of the system. Balanced photodetection can be used to suppress laser RIN and EDFA ASE noise [4-2, 4-3]. Therefore, in order to fully utilize the high power capability of the photodiodes to improve system performance, balanced detection is required. By using a high-saturation-current balanced photodetector, the optical link can achieve shot noise limited performance at high optical powers. The link gain, spurious-free dynamic range, and noise figure can be greatly improved. In optical heterodyne receivers using optical local oscillators, high power balanced photodetectors also have important applications for suppressing local oscillator noise [4-4].

Previously, balanced photodetectors with discrete photodiodes [4-5], waveguide photodiodes [4-6, 4-7], and velocity-matched distributed configurations [4-8, 4-9] have been reported. Among these, a discrete balanced photodetector pair achieved a total current of 72mA and a bandwidth of 500MHz [4-5]; a balanced velocity-matched distributed MSM photodetector achieved a bandwidth of 13.8GHz and 26mA average current for small-signal modulation [4-8]; a balanced velocity-matched p-i-n photodetector achieved a DC linear photocurrent of 45mA [4-9]. In this chapter, high power balanced photodetectors with a top-illuminated, charge-compensated uni-traveling-carrier (UTC) structure are demonstrated. The balanced detection scheme and the device structure are described first. This is followed by a discussion on measurement results. An approach to improve the saturation current of the top illuminated photodiodes with thicker p-layer is also demonstrated.

4.2 Balanced detection scheme and device structure

Figure 4.1 (a) shows the monolithic balanced detector and the on-wafer probe configuration. Two adjacent photodiodes were fabricated in a balanced photodetector configuration. The p-contact pad of one photodetector was connected to the n-contact pad of the other using metallization during processing. The distance between the two photodiodes was chosen to be 250μm to match the standard pitch of fiber arrays and micro lens arrays. The measurement apparatus

used a custom-made microwave probe with two bypass capacitors on the two outside pins. Positive and negative DC bias can be applied to the photodetectors through these two pins, while they are both AC grounded. The equivalent DC and AC circuits are shown in Figure 4.1 (b) and (c), respectively.

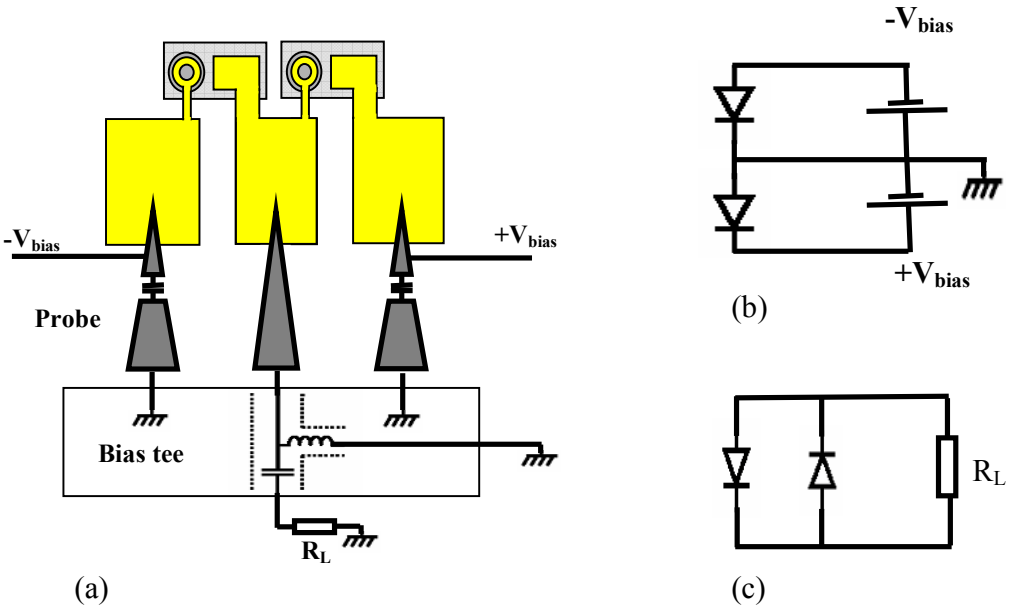

Figure 4.1 Proposed on-wafer balanced detection scheme (a), and equivalent DC (b) and AC (c) circuits

In this balanced configuration, the difference between the optical inputs on the two photodiodes will be delivered to the load, while the common part of the two inputs will be canceled. Therefore, in operation, the signals incident on these two photodiodes are made complimentary so that they will be added in phase on the load. At the same time, the RIN noise and the ASE noise are made common so

that they will cancel. However, due to the asymmetry of the two photodiodes, in real devices, the common mode input cannot be completely canceled. The output ratio of the differential mode input to the common mode input is called the common mode rejection ration (CMRR). It is a measure of the noise suppression capability of a balanced detector.

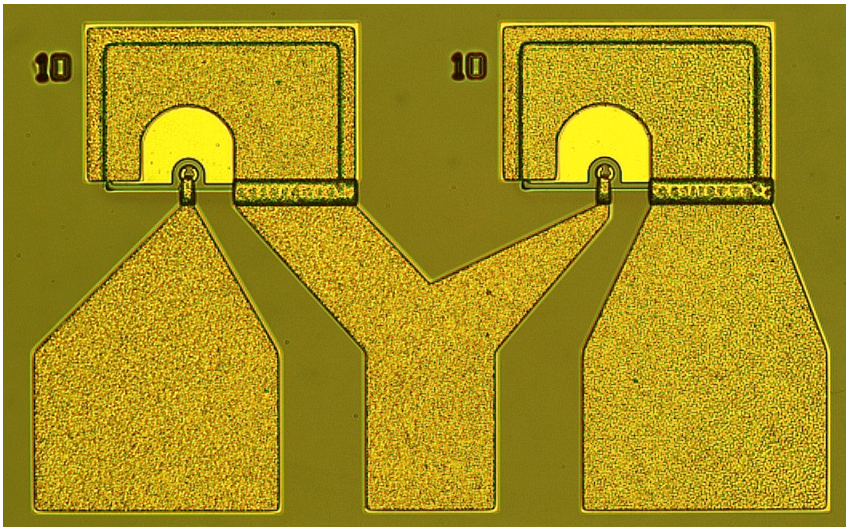

Figure 4.2 A microscopic picture of a fabricated 10μm-diameter photodiode balanced pair

The wafer structure used to fabricate balanced photodetectors is the same as the one shown in Figure 3.5 that has a charge-compensated UTC photodiode structure. For this project, the wafer was fabricated into top-illuminated, balanced photodetectors using conventional photolithography, wet chemical etching, and lift-off metallization techniques. A 220nm-thick SiO_2 film was deposited on top of the wafer after mesa definition to serve as a passivation and an anti-reflection

coating. Microwave pads were connected to the photodiode contact metal through electroplated air-bridges. Figure 4.2 is a picture of a fabricated balanced photodiode pair with 10μm-diameter photodiodes.

4.3 Measurement results and discussion

The frequency response, broadband CMRR and saturation behavior of the fabricated balanced photodetectors were characterized with a large-signal optical heterodyne setup shown in Figure 4.3. Two DFB lasers having nominal operating wavelengths of 1.54μm were used to produce a beat signal with 100% modulation depth. This signal was amplified by an EDFA, split into two branches, and coupled onto the top of the two photodiodes. A variable optical attenuator was connected in one branch to balance the optical power, while a variable optical delay line was used in the other branch to balance the delay time. Lensed fiber tips with a minimum output spot size of 3μm were used to illuminate the photodiodes. All of the photodiodes with diameters equal or larger than 10μm had a measured responsivity of ~0.32A/W.

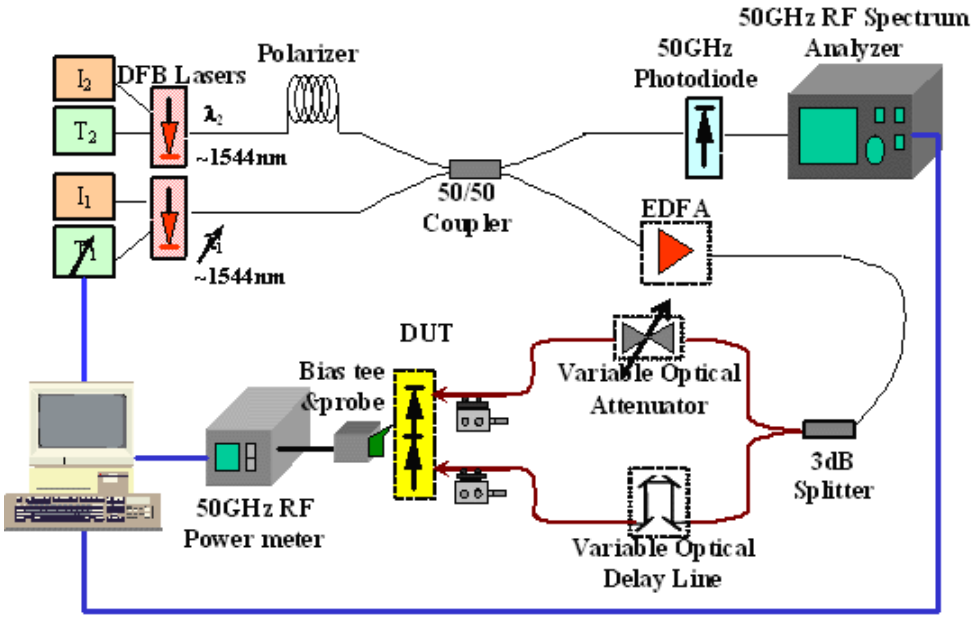

Figure 4.3 Heterodyne setup used for measuring the balanced photodetectors

Figure 4.4 shows the measured frequency response of a typical 20μm-diameter photodiode balanced pair. The top two curves in Figure 4.4 show the frequency response of the balanced photodetector, when only one photodiode was illuminated at a time. Both photodiodes were reverse biased at 4V. The photocurrent of the illuminated photodiode was 10mA. The 3dB bandwidth was measured to be ~10GHz. Compared to a single photodiode, the balanced photodetector exhibits a reduced bandwidth due to the two pn junction capacitances in parallel. The measured CMRR versus frequency is shown in Figure 4.4. In this measurement, the photocurrents of both photodiodes were

matched at 10mA. The optical delay was tuned to be the same in the two arms. A CMRR higher than 35dB was obtained up to 20GHz.

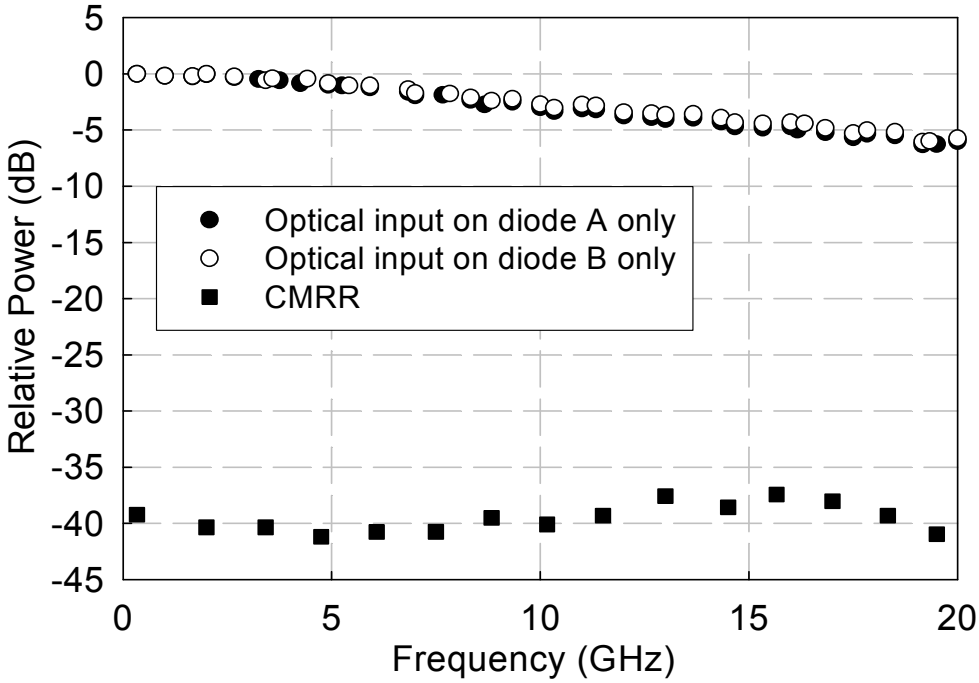

Figure 4.4 Measured relative frequency response of a 20μm-diameter photodiode balanced pair when both the diodes were reverse biased at 4V with (●) optical input on diode A only, at a photocurrent of 10mA, (○) optical input on diode B only, at a photocurrent of 10mA, and (■) two optical inputs with zero phase difference, at photocurrents of 10mA for both diodes

Figure 4.5 shows the results of the saturation current measurement at 10GHz, which is the 3dB frequency of the balanced pair. Under 6V bias, the photodiode can operate at 25mA without saturation. This value is lower than the measured value of the same sized photodiode under backside illumination,

because for top illumination, the lateral resistance in the thin p-type InP layer significantly decreases the voltage drop across the depletion region at high current levels. The saturation current for top illumination can be improved by using a relatively thick highly-doped p-InP window layer, which will be discussed in the next section.

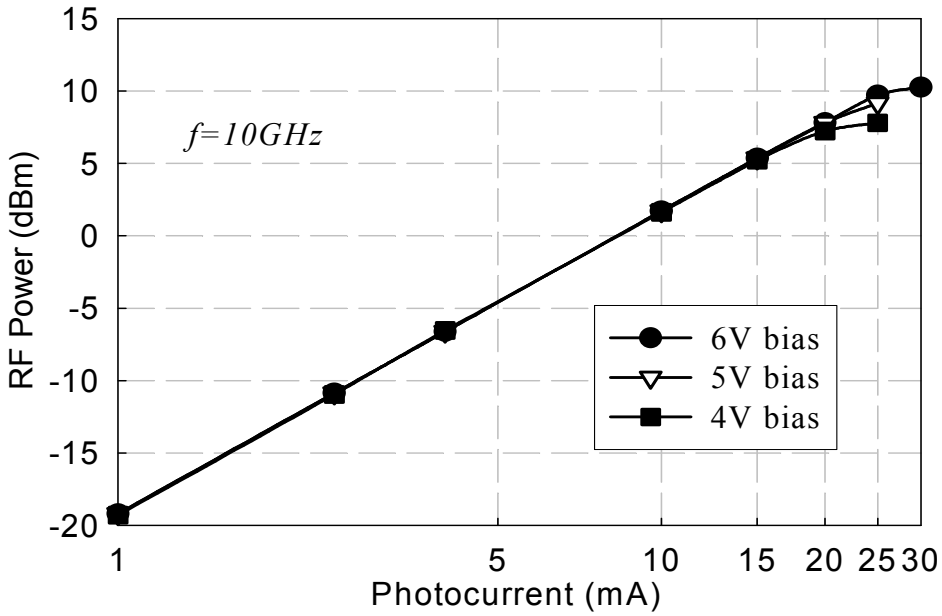

Figure 4.5 Measured output RF power versus photocurrent of a single 20μm-diameter photodiode under various biases at 10GHz

A 10μm-diameter photodiode balanced pair was also characterized. The broadband frequency response is shown in Figure 4.6. The bandwidth of each diode was measured to be ~26GHz. The difference between the two measured

frequency responses was less than 1dB up to 30GHz. In this frequency range, the measured CMRR was higher than 25dB. The broadband CMRR is determined by the symmetry of the frequency response of the two photodiodes. At low frequencies, the output RF power is relatively insensitive to the photodiode parameters, such as junction capacitance, series resistance, and carrier transit time. However, at high frequencies, slight difference between these parameters can result in differences in the RF power drop relative to the RF output power at low frequency. The higher the frequency, the more severe the divergence of frequency response. In addition, fabrication related differences in capacitance and resistance between the two photodiodes is more pronounced for small devices. Therefore, we typically found that the CMRR was lower at high frequencies and for small devices.

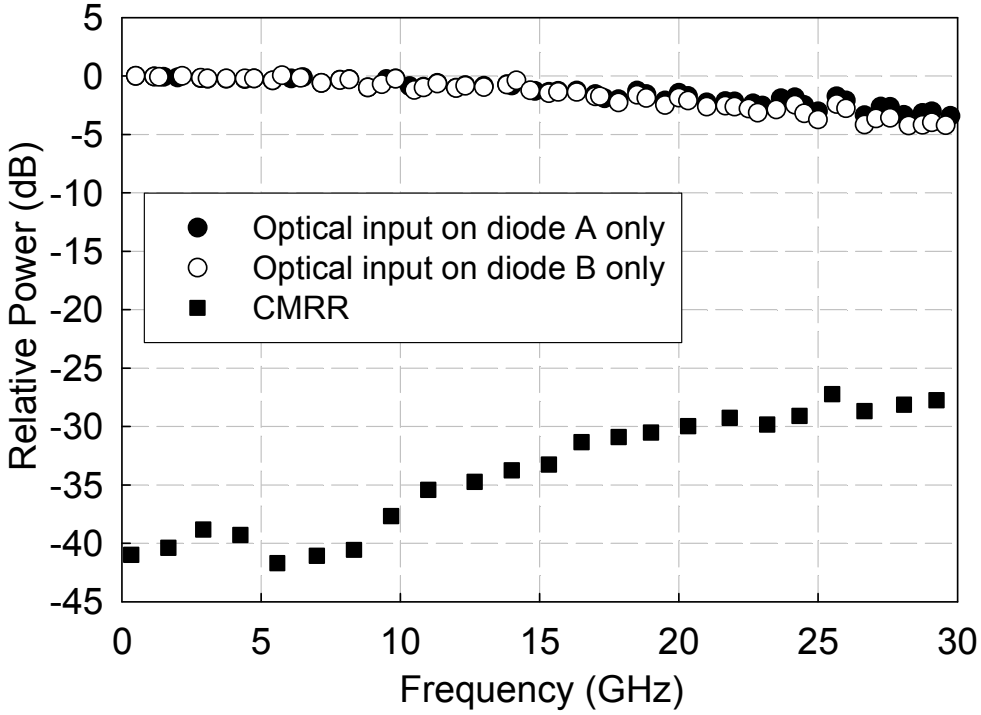

Figure 4.6 Measured relative frequency response of a 10μm-diameter photodiode balanced pair when both the diodes were reverse biased at 4V with (●) optical input on diode A only, at a photocurrent of 10mA, (○) optical input on diode B only, at a photocurrent of 10mA, and (■) two optical inputs with zero phase difference, at photocurrents of 10mA for both diodes

The power saturation behavior was measured at the 3dB bandwidth (26GHz) of the balanced pair as shown in Figure 4.7. Under 6V bias, the photodiode can operate at 15mA without saturation. The saturation current of this small photodiode is smaller than that of the 20μm-diameter photodiode primarily due to the increased current density and reduced maximum dissipated power.

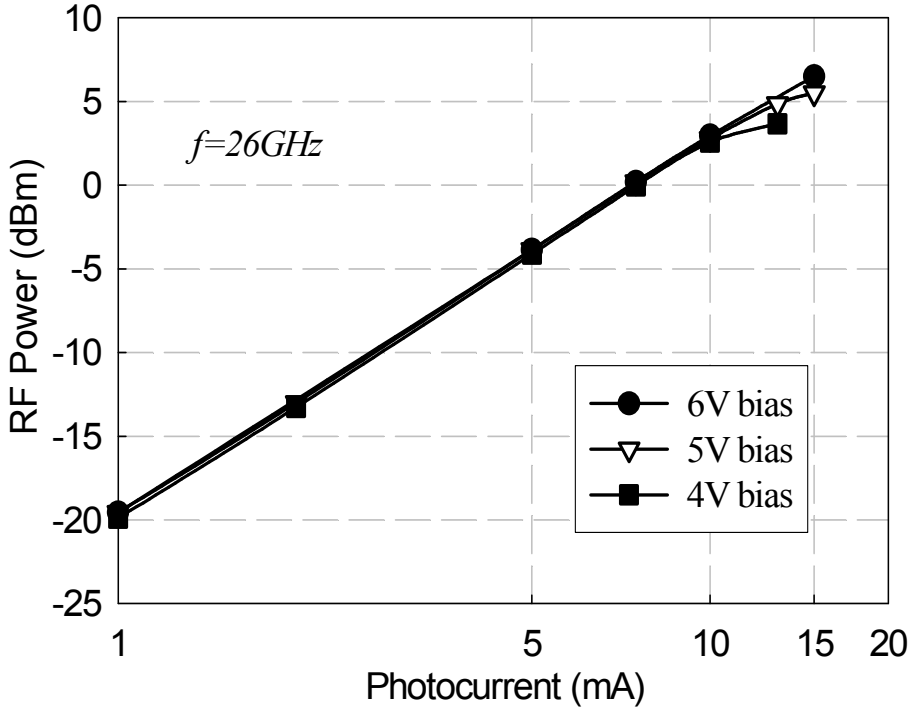

Figure 4.7 Measured output RF power versus photocurrent of a single 10μm-diameter photodiode under various biases at 26GHz

The output signal spectra of a 20μm-diameter balanced pair was also measured at a modulation frequency of 10GHz using a setup similar to the frequency response measurement. Figure 4.8 shows the observed output spectra, (a) when only one photodiode was illuminated, (b) when both photodiodes were illuminated with differential mode signal, and (c) when both photodiodes were illuminated with common mode signal. The differential and common mode inputs were obtained by tuning the variable optical delay line to make the phase

difference between the two optical inputs (2n+1)π and 2nπ, respectively, where n is an integer. The photocurrents of the two photodiodes were kept the same. The CMRR, which is the difference between the peaks of curves (a) and (c), was ~40dB at this frequency. Comparing the differential input signal (b) to the single input case (a), the output signal power was enhanced by ~6dB due to the doubled AC current.

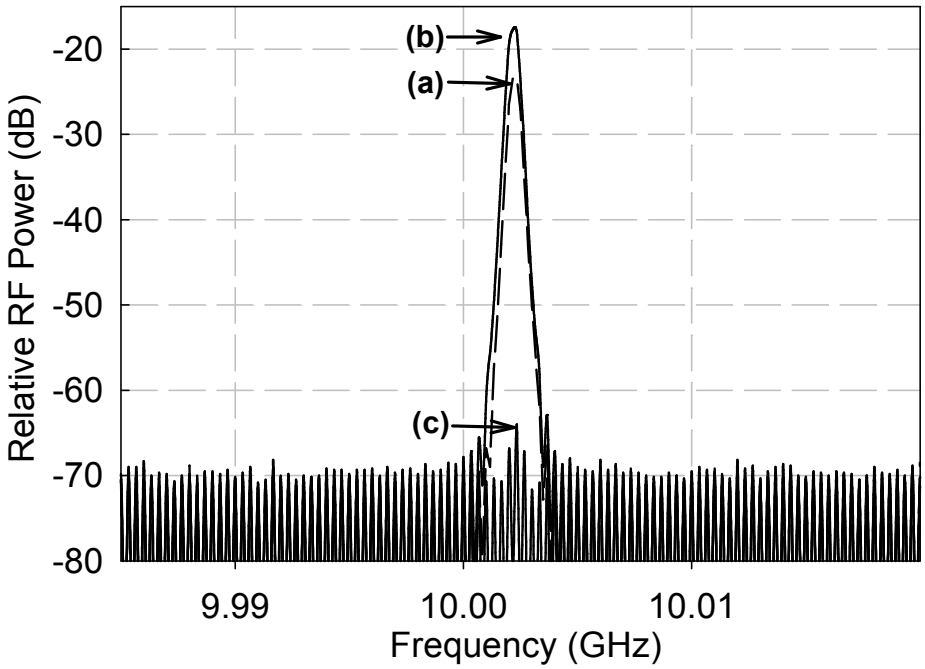

Figure 4.8 Measured output spectra of a fabricated balanced photodetector when (a) only one photodiode was illuminated, (b) both photodiodes were illuminated by the same intensity optical signals with a phase difference of (2n+1)π, and (c) both photodiodes were illuminated by the same intensity optical signals with a phase difference of 2nπ (n is an integer)

The noise suppression of the balanced photodetector was also measured. A comparison of the noise spectra of a 20μm-diameter balanced pair measured with a spectrum analyzer under unbalanced and balanced conditions is shown in Figure 4.9. The optical source used for this measurement was a CW 1.54μm DFB laser. The upper curve is the observed noise floor when only one photodiode was illuminated. The laser RIN peak can be clearly seen, since the balanced photodetector has a bandwidth of 10GHz, which is much larger than the laser RIN peak frequency (4~5GHz). The bottom curve is the observed noise floor when both photodiodes were illuminated so as to achieve the same photocurrent in each photodiode with the same optical delay relative to the source. In fact, the bottom curve is the same as the noise floor of the spectrum analyzer. The step in this noise floor is a property of the spectrum analyzer. The ripple in both noise floors originated from the reflection between the microwave connectors. At the laser RIN peak, the balanced photodetector output noise was suppressed by ~24dB.

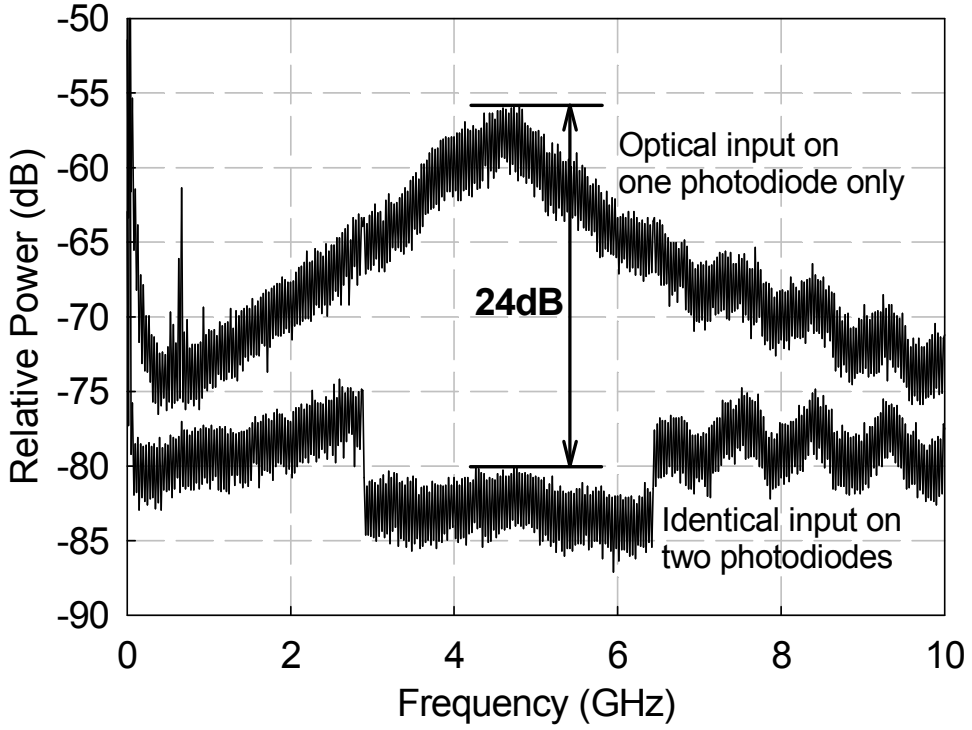

Figure 4.9 Measured noise spectra of a fabricated balanced photodetector in unbalanced (upper curve) and balanced condition (lower curve)

4.4 Saturation current improvement using thick p-layer

The saturation current of top illuminated photodetectors is much smaller than that for backside illumination mainly due to the p-layer lateral resistance. However, top illumination is preferred in some cases, as back illumination is more difficult. In order to increase the saturation current for top illumination, an

improved device structure with a thick p-type layer is proposed and demonstrated in this section.

Figure 4.10(a) shows the wafer structure (wafer #1) with 200nm-thick p-InP used to fabricate the balanced photodetectors discussed in the previous section. Figure 4.10(b) is the improved structure (wafer #2) with a 1000nm-thick p-type InP layer. The improved structure was grown using MBE at the University of Texas at Austin.

InGaAs,	p, $1x10^{19}$,	30nm
InP,	p, $2x10^{18}$,	200nm
InGaAs,	p, $2x10^{18}$,	50nm
InGaAs,	p, $1x10^{18}$,	100nm
InGaAs,	p, $5x10^{17}$,	300nm
InGaAs,	un-doped,	15nm
InGaAsP Q1.3,	n, $5x10^{16}$,	15nm
InGaAsP Q1.1,	n, $5x10^{16}$,	15nm
InP,	n, $5x10^{17}$,	5nm
InP,	n, $5x10^{16}$,	200nm
InP,	n, $5x10^{18}$,	600nm
InP,	Semi-Insulating Substrate	

(a)

InGaAs,	p, $1x10^{19}$,	30nm
InP,	p, $2x10^{18}$,	**1000nm**
InGaAs,	p, $2x10^{18}$,	50nm
InGaAs,	p, $1x10^{18}$,	100nm
InGaAs,	p, $5x10^{17}$,	300nm
InGaAs,	un-doped,	15nm
InGaAsP Q1.3,	n, $5x10^{16}$,	15nm
InGaAsP Q1.1,	n, $5x10^{16}$,	15nm
InP,	n, $5x10^{17}$,	5nm
InP,	n, $5x10^{16}$,	200nm
InP,	n, $5x10^{18}$,	600nm
InP,	Semi-Insulating Substrate	

(b)

Figure 4.10 (a) wafer #1 with 200nm-think p-InP layer and (b) wafer #2 with 1000nm-thick p-InP layer

The transfer-length method (TLM) was used to characterize the p-layer sheet resistance. The measured resistance versus contact pad distance is plotted in Figure 4.11. The sheet resistance was derived from the slope of the fitted lines. It

is clear that the p-layer sheet resistance of the wafer with a 1000nm-thick p-InP is about 1/3 of that of the wafer with a 200nm-thick p-InP. This could lead to significantly reduced lateral voltage drop in the p-InP from the contact ring to the center of the photodiode.

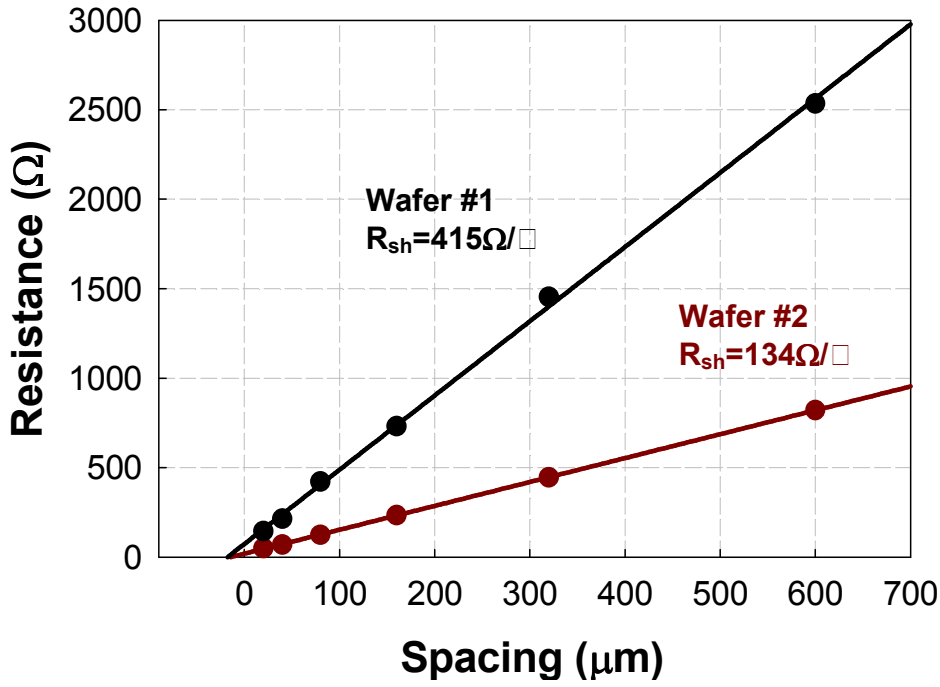

Figure 4.11 Measured p-layer sheet resistance of the two wafers using TLM pattern

Wafer #2 was fabricated into photodiodes using the same mask and process as those used for wafer #1. The fabricated devices were measured using the same setup as for the top illumination case. The saturation current measurement for a 20μm-diameter photodiode is shown in Figure 4.12 in

comparison with the results a photodiode of the same size fabricated from wafer #1. It is clear that the saturation current of the photodiode fabricated from wafer #2 is higher than that of the photodiode fabricated from wafer #1, at the same bias voltage. At 6V reverse bias, the saturation current increased from ~25mA to ~40mA. These results demonstrate that using a thick p-type window layer is an effective approach for improving the saturation current of top-illuminated photodiodes.

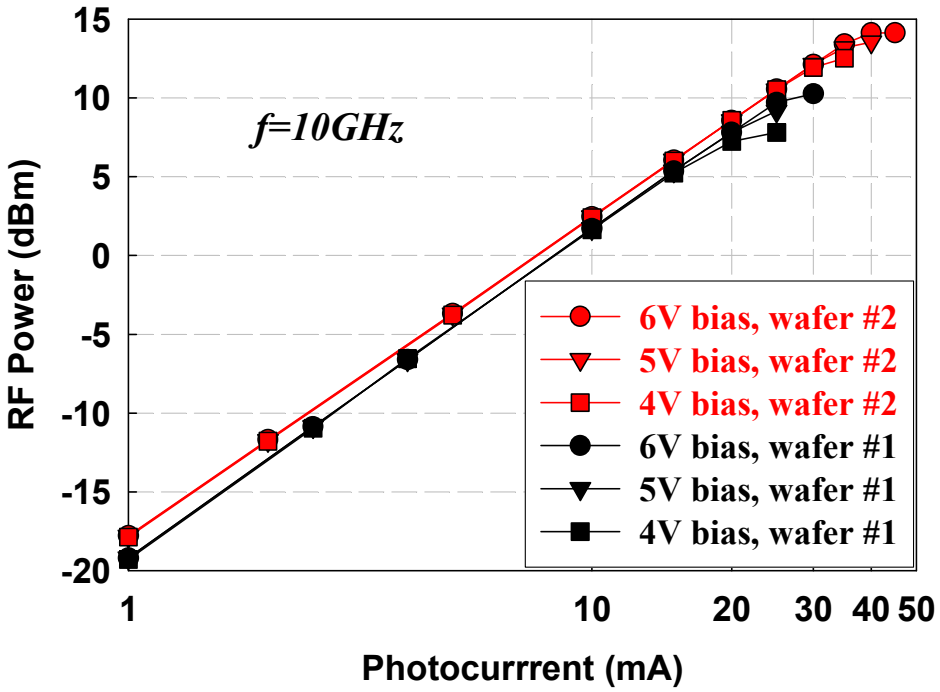

Figure 4.12 Comparison of measured RF output power versus photocurrent for top-illuminated photodiodes fabricated from wafer #1 and wafer #2

4.5 Summary

High-power top-illuminated balanced photodetectors were demonstrated. Using the charge-compensated UTC photodiode structure designed in Chapter 3, a 20μm-diameter photodiode balanced pair achieved a bandwidth of 10GHz and a large-signal saturation current of 25mA for each photodiode. A 10μm-diameter photodiode balanced pair achieved a bandwidth of 26GHz and a large signal saturation current of 15mA for each photodiode. The broadband common mode rejection ratio and noise suppression were also characterized. For top illumination, a thick p-type window layer is preferred because reduced the p-layer lateral resistance. By increasing the p-InP thickness from 200nm to 1000nm, the saturation current of a 20μm-diameter photodiode was increased from 25mA to 40mA. These high power balanced photodetectors can be used in high power and high frequency analog optical links to improve the link performance.

Chapter 5: Evanescently-Coupled Short-Multimode Waveguide Balanced Photodetectors

5.1 Introduction

For the surface illuminated photodiode, there exists a tradeoff between quantum efficiency and carrier transit time. This tradeoff limits the responsivity of high speed devices. Side-illuminated photodiodes in which the responsivity and transit time are decoupled can overcome this restriction. High responsivity and broad bandwidth were achieved for directly side-illuminated photodiodes [5-1]. However, the directly side-illuminated photodiode has poor optical power handling capability due to a high current density near the waveguide input facet. Evanescently-coupled waveguide photodiodes can achieve much higher saturation current than the directly side-illuminated approach [5-2], owing to more uniform light absorption. To increase the responsivity of high-speed high-power photodiodes, an evanescently-coupled waveguide structure is investigated in this chapter.

There are two approaches for evanescent coupling. One uses a single mode taper as a spot size converter [5-3, 5-4]; the other uses mode interference in a short multimode waveguide [5-5, 5-6]. The approaches using single mode spot size converters require complex fabrication steps, such as sub-micron

microlithography and etching [5-4], and special non-planar processing techniques [5-3]. Here, a short-multimode waveguide photodiode (SMWP) approach is chosen due to its simple fabrication technology and high yield. In this chapter, the design of SMWP will be discussed first, followed by the details of the fabrication and measurement results of balanced SMWPs.

5.2 Device design

A schematic cross section of the waveguide photodiode is shown in Figure 5.1(a). Figure 5.1(b) shows the layer structure of the wafer. The multimode waveguide consists of a diluted waveguide and two optical matching layers. The diluted waveguide is a stack of 10-periods of un-doped InP/GaInAsP (1.1-μm band gap) layers. The number of periods has been optimized to achieve high coupling efficiency with an input fiber and low TE/TM polarization dependence. The two optical matching layers are N-doped GaInAsP. The doping concentration is $1\times10^{18}cm^{-3}$, which exhibits acceptable free carrier loss, while maintaining a good N-type contact. The band gaps correspond to 1.1-μm and 1.4-μm for the first and second optical matching layers, respectively. This provides a gradual increase of the optical refractive index from the diluted waveguide to the absorbing layer, which results in a significant enhancement of the quantum efficiency.

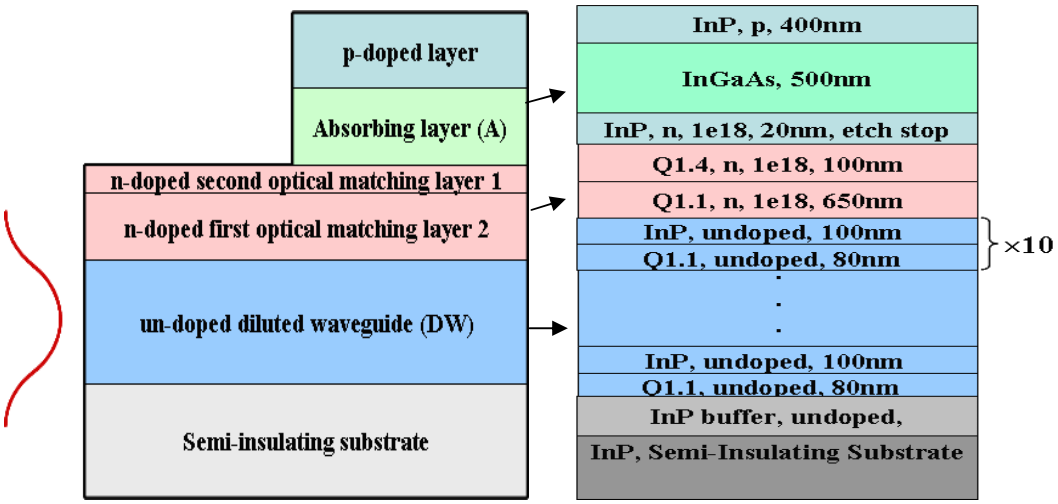

(a) (b)

Figure 5.1 (a) Schematic cross section layer diagram of the evanescently coupled short multimode photodiode structure and (b) wafer structure

The structure was simulated and optimized using BEAM_PROP, a commercial simulation tool based on the Beam Propagation Method (BPM) from RSoft Corporation. In the optimization, the layer thickness was scanned to maximize light absorption in a short photodiode length. Figure 5.1(b) shows the optimized epitaxial layers with their thickness and doping level. The simulated light intensity in the final waveguide photodiode structure is shown in Figure 5.2. The multimode beating can be clearly seen from the picture.

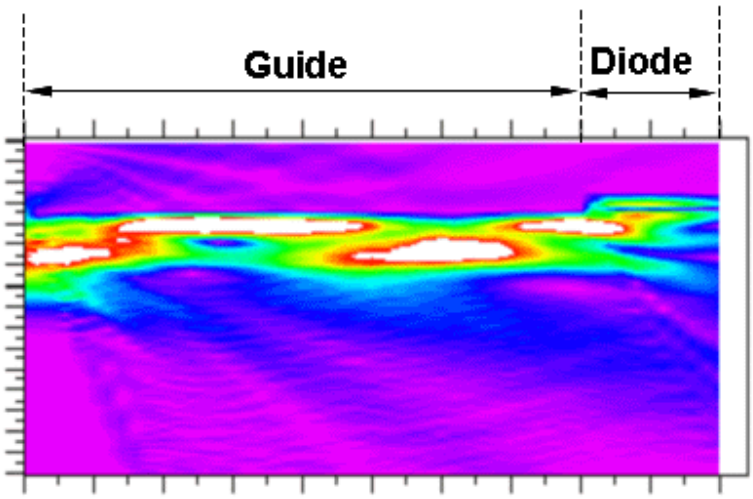

Figure 5.2 BPM simulation result of the light propagation and absorption in the finalized SMWP structure

5.3 Balanced waveguide photodetector

Photodiode responsivity limits the output power of the high power photodiodes in cases where the input optical power is limited. The top-illuminated balanced photodetectors described in Chapter 4 exhibit low responsivity of ~0.32A/W. Balanced waveguide photodetectors are demonstrated here. The motivation for utilizing waveguide photodiodes in a balanced configuration is to achieve higher responsivity than the top illuminated balanced photodetectors described in Chapter 4. The waveguide structure used is the same as that described in the last section. Two different photodiode structures were investigated. One was a conventional PIN photodiode structure; the other was a

partially depleted absorber (PDA) photodiode structure [5-7]. To keep the optimization of the SMWP the same, the InGaAs absorber thickness is 500nm for both PIN and PDA structures. Different from the PIN structure, the absorber of the PDA structure consisted of a 260nm depleted InGaAs layer sandwiched between a 180nm-thick p-doped InGaAs layer and a 60nm-thick n-doped InGaAs layer.

5.3.1 Device fabrication

The wafer was grown by molecular beam epitaxy on a semi-insulating substrate. The photodiode mesas were patterned using a dry etch, followed by a wet etch. The P-contact metallization was used as an etching mask and a thin InP layer on the top of the waveguide served as an etch stop. A SiO_2 passivation film was then deposited. After the diode was isolated by a dry etch, a planarization polyimide was patterned where the electrical pads are formed at the end of the process. The photodiodes were connected to contact pads through air bridges. The chips were precisely cleaved using V-grooves etched using HBr. Finally, a $ZnSe/MgF_2$ AR coating was deposited on the waveguide input facet. Details of the fabrication process are described in Chapter 2. Figure 5.3 shows a microscope picture of the fabricated balanced SMWP. The planar waveguide, photodiode, V-groove and planarization polyimide can be clearly seen from the picture. The

distance between the two photodiodes is 250μm, which is one of the standard distances for fiber and lens arrays.

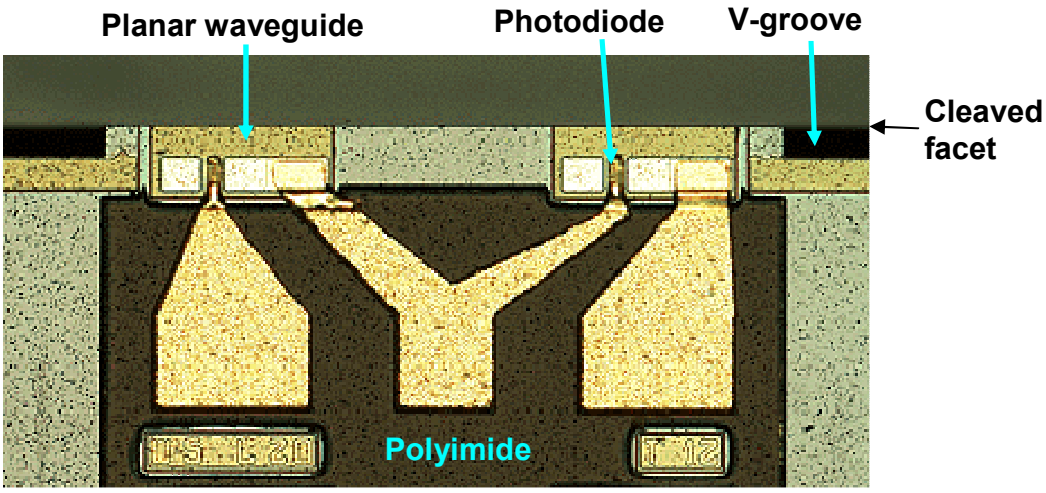

Figure 5.3 Microscope picture of fabricated balanced SMWP

5.3.2 Measurement results

The fabricated balanced photodetectors were characterized with a large-signal optical heterodyne setup similar to the one used in Chapter 4. Two polarizers were used in front of the two waveguide photodiodes to optimize the responsivity. The light was coupled to the balanced photodetectors using two lensed fibers with spot sizes of 5μm. In balanced operation, both diodes in the balanced pair were reverse biased through a custom designed microwave probe. The photocurrents of the two photodiodes were monitored separately. The responsivities of the waveguide PIN and PDA photodiodes were measured to be

0.94A/W and 0.81A/W, respectively. The polarization dependence was smaller than 0.5dB.

Figure 5.4 shows the measured relative responsivity versus fiber tip position of the waveguide photodiodes. The -1dB alignment tolerance was ±1.8μm in the lateral (parallel to wafer surface) direction and ±1.25μm in the vertical direction. When coupling the light into both photodiodes of a balanced pair using a lensed fiber array, the responsivity was ~30% lower than that of single devices. This is due to the mismatch of the fiber array and the balanced photodetectors, and could be improved by using more accurate coupling methods.

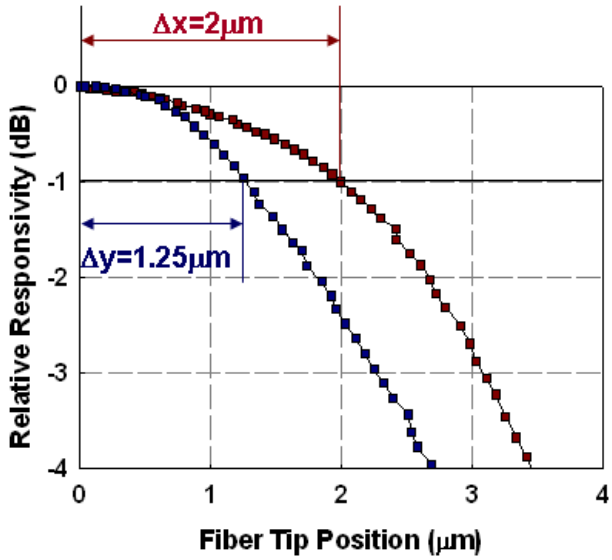

Figure 5.4 Measured relative responsivity versus the fiber tip position of a fabricated SMWP

The measured frequency response and the saturation behavior of both types of balanced photodetectors are shown in Figure 5.5. The load was 50Ω in all

the measurements. Figure 5.5 (a) shows the frequency response of a typical SMWP balanced pair consisting of two 5x20μm^2 PIN photodiodes, when only one photodiode was illuminated at a time. The 3dB bandwidth of the balanced pair was measured to be ~30GHz. The difference between the two frequency response curves was less than 0.4dB up to 30GHz. Figure 5.5(b) shows the results of the saturation current measurement for one of the photodiodes at 30GHz. Under 3V bias, the 1-dB compression photocurrent was ~10mA. The maximum output RF power from one photodiode at this frequency was ~0dBm. With a differential input signal to the balanced photodetector, the maximum total RF output power is expected to be ~6dBm at 30GHz. The bandwidth of a 5x20μm^2 SMWP with PDA photodiode balanced pair was ~24GHz, as shown in Figure 5.5(c). The difference between the two frequency response curves was less than 0.7dB up to 30GHz. The power saturation behavior was measured at the 3dB frequency (24GHz) of the balanced pair. Under 3V bias, the 1-dB compression current was ~16mA, as shown in Figure 5.5(d). The maximum output RF power from one photodiode at this frequency was ~3dBm. With a differential input signal to the balanced photodetector, the maximum total RF output power was expected to be ~9dBm at 24GHz. The bandwidth of the PDA device is smaller than the PIN device due to higher junction capacitance. The bandwidth-current

product of the PDA device is higher than that of the PIN device due to a reduced space charge effect [5-7].

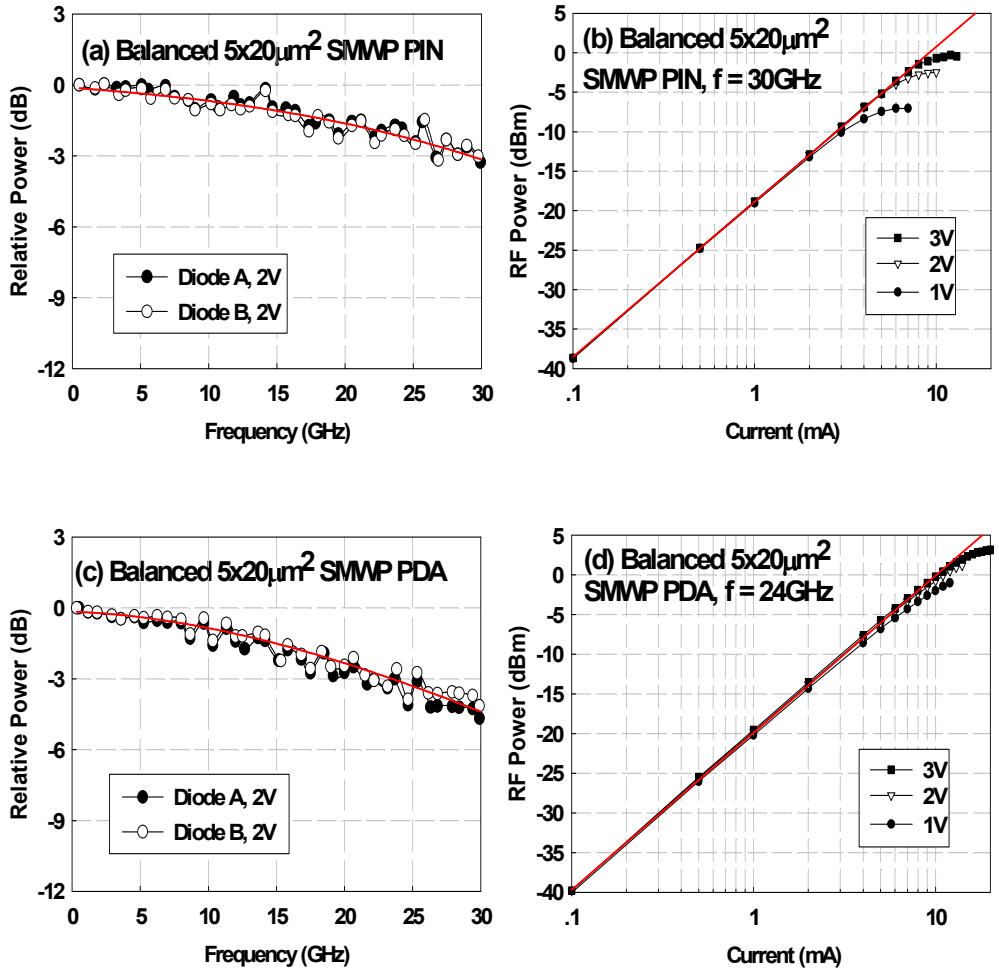

Figure 5.4 Measured frequency response (a) and output power versus current (b) of a 5x20μm^2 SMWP PIN, Measured frequency response (c) and output power versus current (d) of a 5x20μm^2 SMWP PDA

The output signal spectra of a 5x20μm^2 SMWP PDA balanced pair was also measured, as shown in Figure 5.6, at a modulation frequency of 10GHz using a setup similar to the frequency response measurement. The differential and common mode inputs were obtained by tuning the variable optical delay line to make the phase difference between the two optical inputs $(2n+1)\pi$ and $2n\pi$, respectively, where n is an integer. The photocurrents of the two photodiodes were kept the same. The CMRR, which is the difference between the peaks of curves (b) and (c), was ~30dB at this frequency. With differential input signal (b), compared to the single input case (a), the output signal power was enhanced by ~6dB due to the doubled AC current.

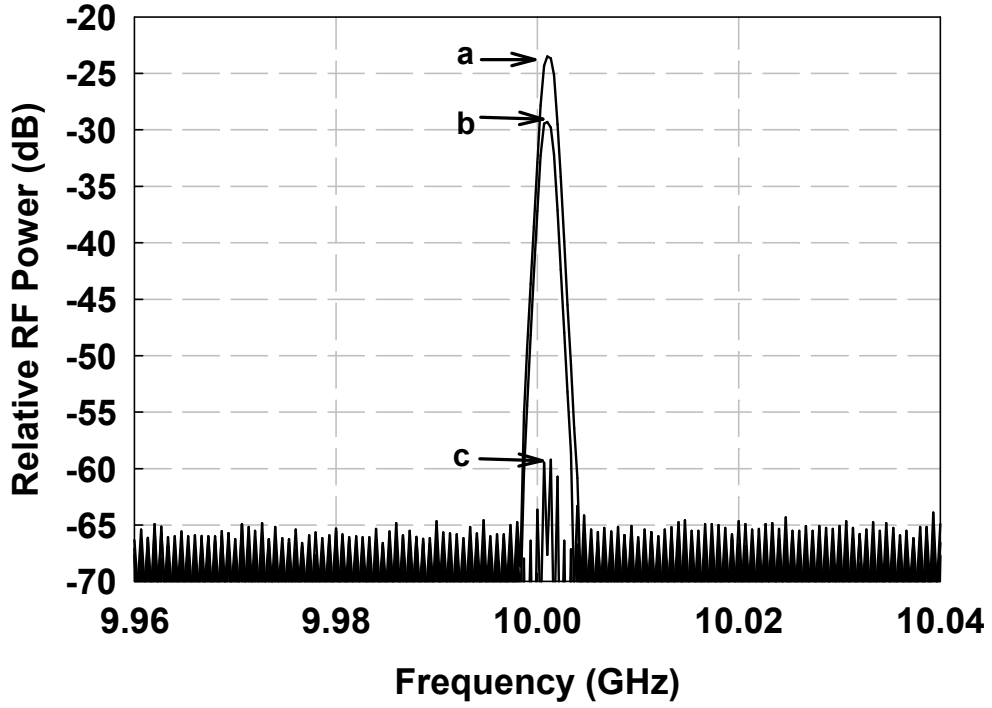

Figure 5.6 Measured output spectra of a balanced SMWP PDA photodetector when (a) only one photodiode was illuminated, (b) both photodiodes were illuminated by the same intensity optical signals with a phase difference of $(2n+1)\pi$, and (c) both photodiodes were illuminated by the same intensity optical signals with a phase difference of $2n\pi$ (n is an integer)

5.4 Summary

Evanescently-coupled short multimode waveguide photodiodes (SMWP) were designed, fabricated and characterized. Very high-responsivity, low polarization dependence, and broad bandwidth were achieved simultaneously for single photodiodes. Balanced SMWP PIN and PDA photodetectors were

demonstrated for the first time. A SMWP balanced pair consisting of two $5x20\mu m^2$ PIN photodiodes exhibited a responsivity of 0.94A/W, a bandwidth of 30GHz, and a large-signal saturation current of 10mA for each photodiode. A SMWP balanced pair consisting of two $5x20\mu m^2$ PDA photodiodes exhibited a responsivity of 0.81A/W, a bandwidth of 24GHz, and a large-signal saturation current of 16mA for each photodiode. Compared to the top illuminated balanced photodetectors described in Chapter 4, these devices achieved a much higher responsivity, while maintaining a broad bandwidth. A more accurate coupling method needs to be used for coupling light into the two waveguide photodiodes at the same time.

Chapter 6: Au-bonded High-power Photodiodes with Improved Responsivity and Output Power

6.1 Introduction

For high power photodiodes, once the structure is fixed, the saturation current is strongly tied to the device bias voltage. The photodiode bias can be increased to postpone the onset of saturation. However, elevated bias voltage and current will cause elevated heat dissipation. Thermal failure will ultimately limit the photodiode output power. The better the heat transfer out of the photodiode depletion region, the higher the maximum dissipated power. InP is the lattice-matched substrate widely used for InGaAs photodetectors working at 1.55μm. If the InP substrate can be replaced by materials with higher thermal conductivity, the heat conduction through the substrate can be improved [6-1].

In this chapter, high power InGaAs/InP photodiodes transferred onto a Si wafer using gold wafer bonding are demonstrated. Si was chosen because both its thermal conductivity and specific heat capacity are more than two times higher than those of InP at 300K. For temperatures greater than 300K, the thermal conductivity ratio between the two materials is even higher. In addition to better heat conduction, the bonding also offered a method to integrate the infrared detectors with Si-based read-out electronics on the same chip, which may provide

additional functionalities, superior performance, and lower cost compared to hybrid solutions. Gold wafer bonding was chosen because it can be achieved at ~200°C, which is much lower than the temperature needed for direct wafer bonding. This means much less stress is introduced in the process. Another advantage of this Au-bonded photodiode structure is the resonant cavity enhanced responsivity. In the following, the results of simulations of the effect of bonding on heat conduction and responsivity, the gold bonding process, and the experiment will be discussed.

6.2 Simulation results

Simulations were used to compare the expected performance of photodiodes grown on InP to photodiodes transferred to a Si substrate. The simulated characteristics include the photodiode heat handling capabilities and photodiode responsivity.

6.2.1 Effect of bonding on heat conduction

An analytical thermal model of surface-illuminated photodiodes was developed [6-2] to calculate the photodiode temperature versus the total dissipated power. In this model, the temperature dependent thermal conductivity of different layers was taken into account and heat generation was considered to be uniform in the depletion region. The heat conduction in the photodiode mesa was considered

to be one dimensional, while three dimensional heat flow in the substrate was taken into account. The same model is used to compare the power handling capabilities of InGaAs PIN and UTC photodiodes grown on InP to those bonded to Si substrates.

Figure 6.1 shows the simulation results of the depletion layer temperature versus total dissipated power for various photodiodes. For an InGaAs PIN photodiode, the total dissipated power can be nearly doubled at the same photodiode temperature, by switching the substrate from InP to Si. This improvement is even higher for the UTC photodiode. This is due to ease of heat flow from the depletion layer in a UTC photodiode, resulting from the higher thermal conductivity in InP than InGaAs. This means that, after bonding the photodiode can handle a higher bias voltage and current, thus delivering higher RF power to the load.

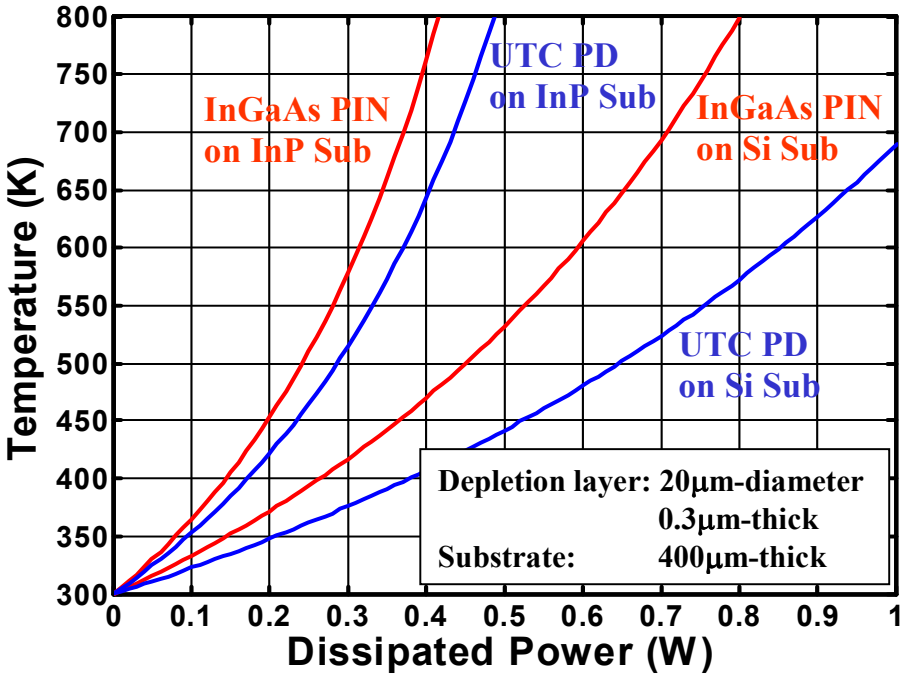

Figure 6.1 Simulated maximum depletion layer temperature versus dissipated power for InGaAs PIN and UTC PD on top of InP and Si substrates

6.2.2 Effect of bonding on responsivity

In high power photodiodes, it is usually preferable to utilize a thin InGaAs absorbing layer to reduce thermal impedance, space charge effects, and/or the carrier transit time. Therefore, in some cases where the optical input power is limited, the maximum RF output power is limited by its low responsivity, though the photodiode can handle very high power.

Due to the high reflectivity of gold in the infrared (>98% at 1.55μm), the gold layer introduced in the bonding process can also be used as a bottom mirror to form a resonant cavity enhanced (RCE) photodiode structure. Through proper

design, this resonant cavity can improve the photodiode responsivity significantly at the operating wavelength.

Figure 6.2 shows the simulated photodiode peak quantum efficiency (at the resonant wavelength near 1.55μm) of an InGaAs RCE photodiode versus InGaAs absorber thickness for different top and bottom mirror configurations. The calculation was made using the transfer matrix method. Both the amplitude and the phase change at the semiconductor-gold interface were considered by taking into account the complex refractive index of gold. For devices with an InGaAs absorber thickness of 0.45μm, Table 6.1 compares the calculated values of quantum efficiency and responsivity for photodiodes with and without a gold bottom mirror. The quantum efficiency of this photodiode structure without a gold mirror is only 25%. By simply using the 30% reflectivity of the semiconductor-air interface as the top mirror, the peak quantum efficiency of the bonded photodiode can be as high as 90%. A higher quantum efficiency can be achieved using a top mirror with a 50% reflectivity. This will allow the photodiode to deliver much more RF power with the same available optical input power, which is a very desirable property for high power photodiodes in cases where optical power is limited.

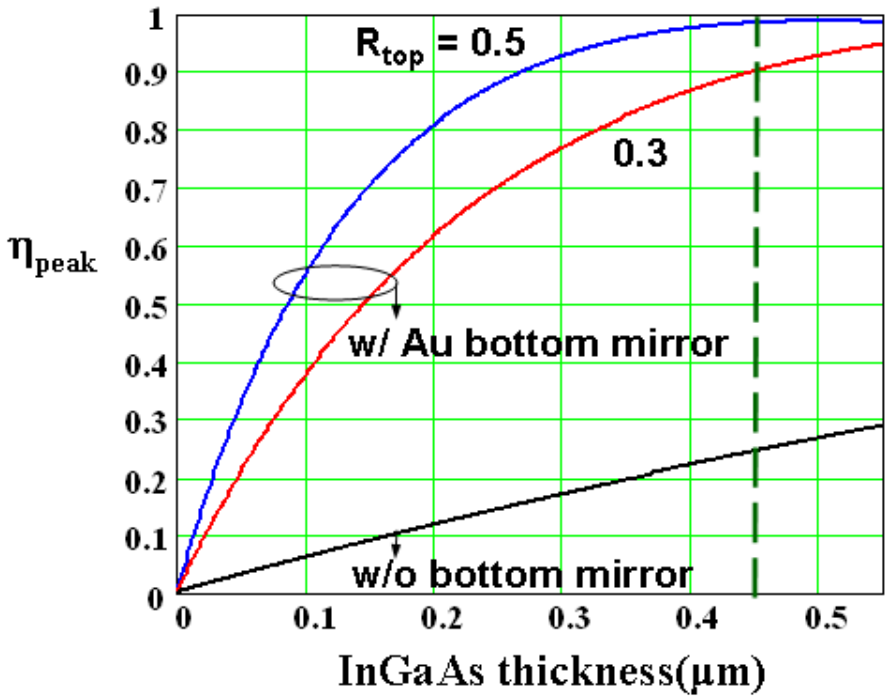

Figure 6.2 Calculated photodiode peak quantum efficiency versus InGaAs absorber thickness for various top and bottom mirror configurations: (a) top illuminated photodiode without Au bottom mirror, (b) top illuminated photodiode with a Au bottom mirror and a top mirror reflectivity of 30%, and (c) top illuminated photodiode with a Au bottom mirror and a top mirror reflectivity of 50%

Photodiode structure	Without Au mirror	With Au mirror	
		R_{top}=30%	R_{top}=50%
Quantum efficiency	25%	90% (peak)	98% (peak)
Responsivity (A/W)	0.31	1.1 (peak)	1.2 (peak)

Table 6.1 Calculated photodiode peak quantum efficiency and responsivity near 1550nm for top illuminated photodiodes with a 0.45μm-thick InGaAs absorber

6.3 Au wafer-bonding process

Direct wafer bonding (~600°C) has been reported for transfering InGaAs high power photodiodes onto Si substrates [6-1, 6-3]. In this work, in order to reduce the annealing temperature, a gold bonding method was used [6-4]. Uniform bonding was achieved at 200°C, which is much lower than that required for direct wafer bonding (typically ~600°C). The stress induced by the thermal expansion mismatch of InP and Si during annealing was significantly reduced. This low-temperature process also allowed Zn and Be doping during material growth before the bonding process, because diffusion is minimal at this low temperature. Using this Au bonding procedure, the photodiode can be transferred not only to Si, but also to other substrates or ceramics with even higher thermal conductivity and/or heat spreading capability than Si.

The process flow of gold wafer bonding is shown in Figure 6.3. The high power photodiode structure was first grown in reverse order on an InP substrate using MBE. The bonding process begins with mesa etching. This ensured that no gas or liquid would be trapped at the interface. Then, ~400nm of Au was deposited on top of both the InP epitaxial wafer and an intrinsic Si wafer. The gold surfaces of these two wafers were bonded under conditions of elevated pressure and temperature using the equipment described in Reference [6-5]. Good bonding quality can be achieved at ~200°C. After bonding, the InP

substrate on which the photodiode material was grown was removed using a wet etch that stopped at an InGaAs etch stop layer. At this point, the epi-layers were transferred onto the Si wafer. A microscopic picture of the bonded wafer after this step is shown in Figure 6.4. No bubbles are observed at the bonding interface. The Au layer between the mesas was etched away to provide electrical isolation.

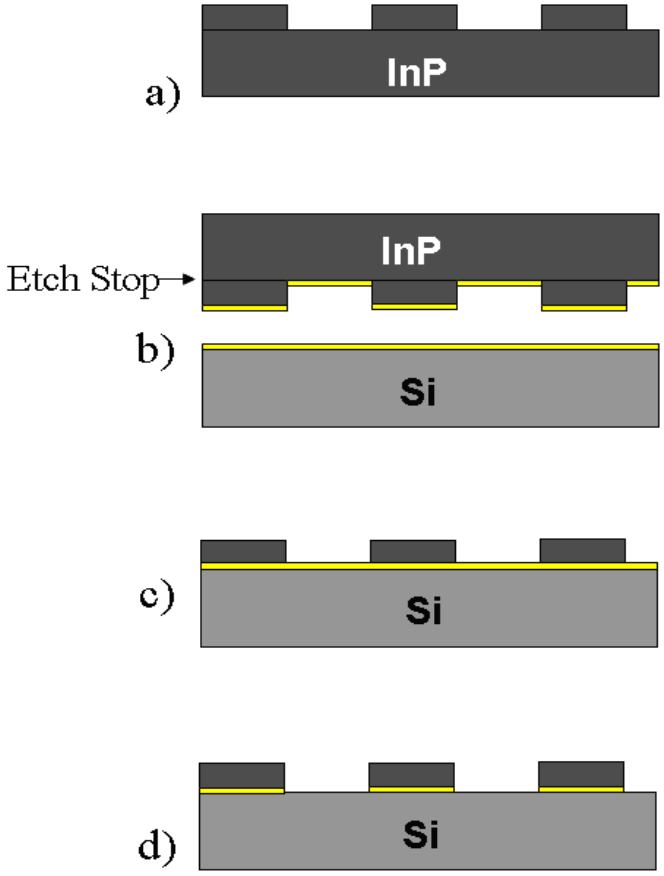

Figure 6.3 Au wafer bonding process: a) Epi-layer mesa etching, b) Au deposition and annealing, c) InP substrate removal, and d) Au bonding layer etching

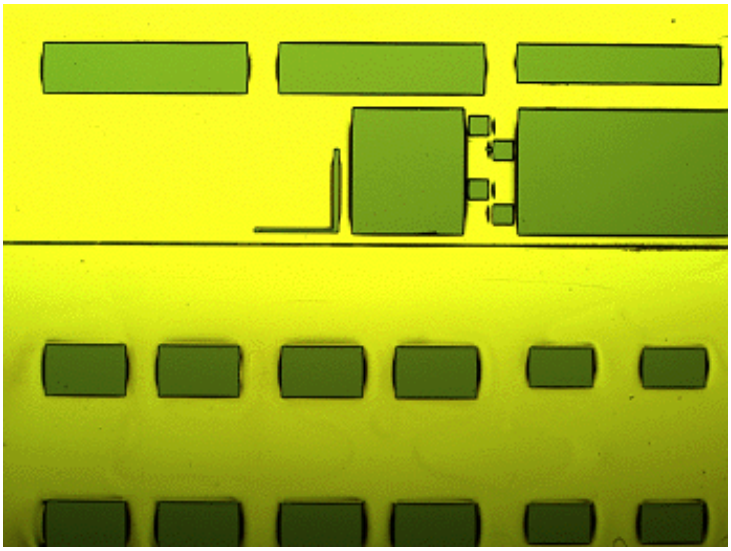

Figure 6.4 A plane view microscopic picture of the Au bonded wafer taken after InP substrate removal (step (c) in Figure 6.3)

6.4 Experimental results and discussion

After transferring the substrate, the wafer was fabricated into high-speed top illuminated photodiodes using our conventional photodiode fabrication process. Figure 6.5 is a schematic diagram of a fabricated photodiode. The measured responsivity, bandwidth and saturation current of the Au-bonded photodiodes were compared to our previously fabricated top-illuminated photodiodes with the same structure on an InP substrate.

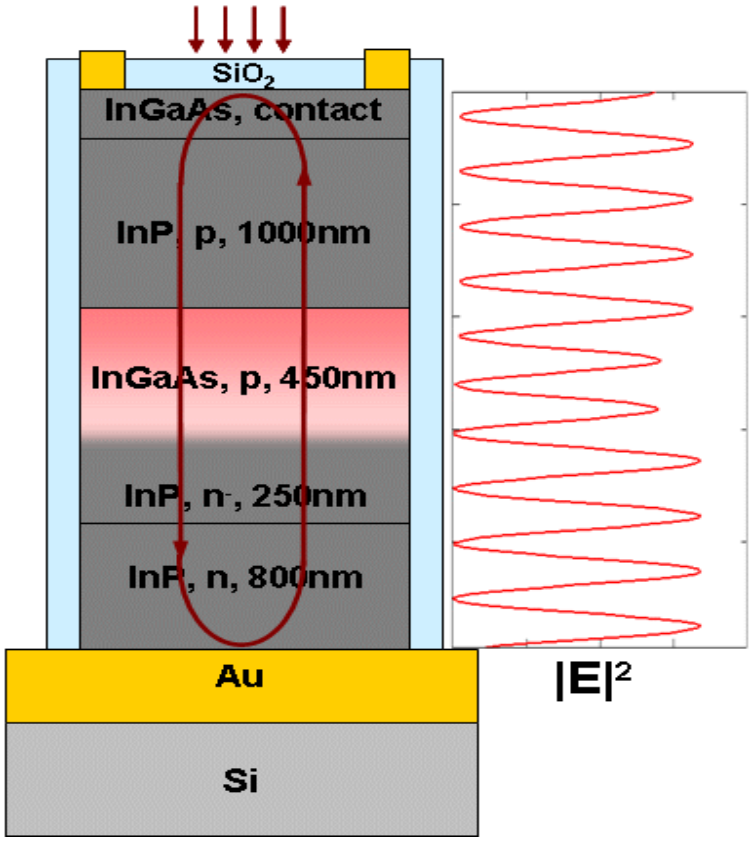

Figure 6.5 Schematic diagram of a fabricated photodiode

Responsivity versus wavelength characteristics of the bonded photodiode is shown in Figure 6.6. With a 260nm SiO_2 passivation layer on top, the top mirror reflectivity was estimated to be ~10%. The peak responsivity was higher than 0.8A/W (64% quantum efficiency) at ~1530nm. By etching away the SiO_2 passivation layer on top of the photodiode, the cavity top mirror reflectivity increased to 30%. In this case, the photodiode responsivity was measured to be ~1A/W (80% quantum efficiency) at ~1526nm and higher than 0.8A/W over a

~25nm bandwidth range. These responsivity values are much higher than those of the same photodiode fabricated on InP, which were 0.32A/W for top illumination and 0.45A/W for backside illumination. By adjusting the cavity length, the resonant wavelength can be tuned to 1550nm or other desired wavelength.

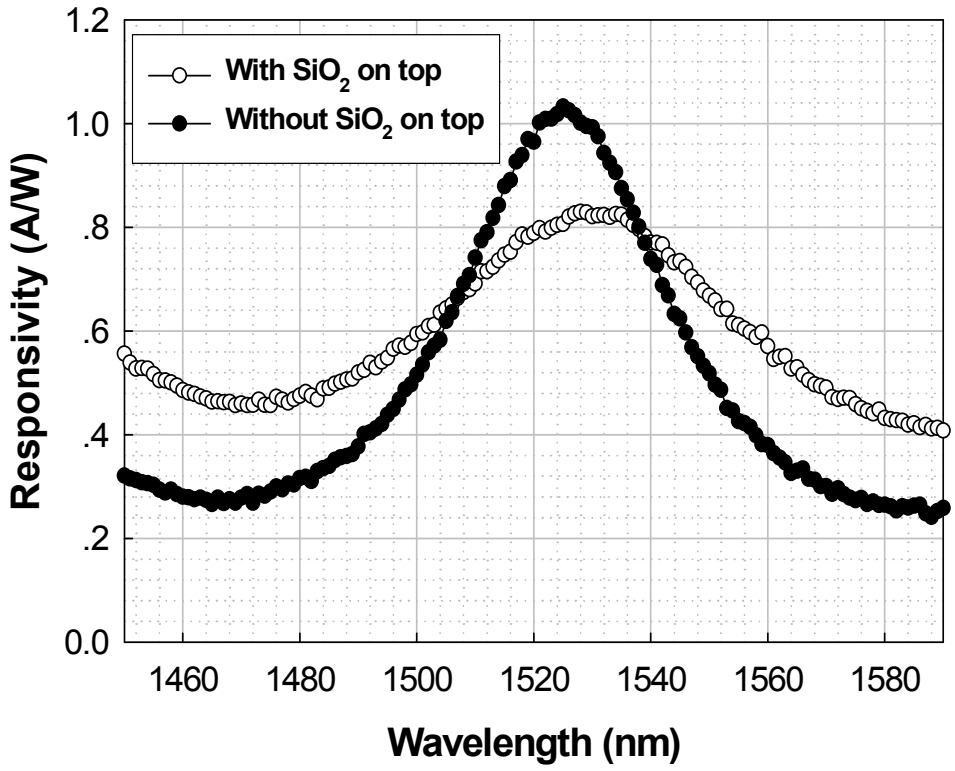

Figure 6.6 Measured responsivity versus wavelength of bonded photodiode

The frequency response and saturation behavior of the fabricated photodiodes was characterized with the large-signal optical heterodyne setup discussed in the previous chapters. Figure 6.7 shows the measured frequency

response of a 20μm-diameter photodiode bonded on Si and a 20μm-diameter photodiode on InP. Both devices showed a similar bandwidth of ~18GHz.

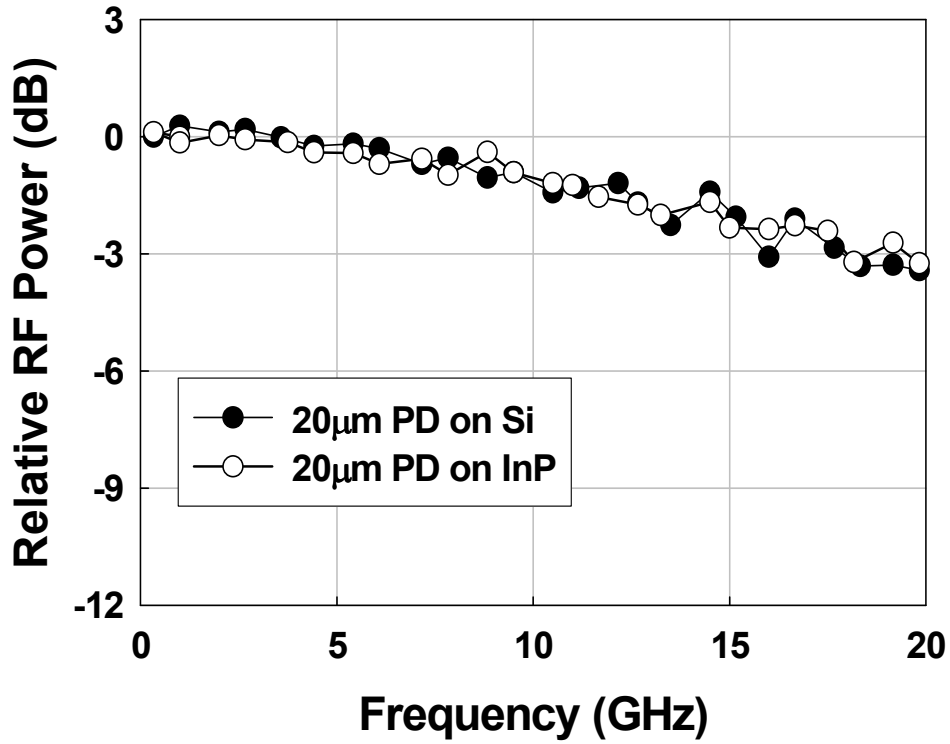

Figure 6.7 Measured frequency response of a 20μm-diameter photodiode bonded on Si and a 20μm-diameter photodiode on InP

Figure 6.8 shows the measured output RF power versus photocurrent at 10GHz of: (a) a top-illuminated 20μm-diameter photodiode on an InP substrate and (b) a top-illuminated 20μm-diameter photodiode bonded on Si wafer. For the photodiode on InP, the maximum operating currents without saturation were

30mA under 4V bias, 35mA under 5V bias, and 40mA under 6V bias. This device died at 45mA at 6V bias due to thermal failure. All the photodiodes of the same size failed at similar conditions. At bias voltages of 4V, 5V and 6V, the 20μm photodiode bonded on Si showed very similar saturation behavior as the photodiode on InP. Due to better thermal conductivity and larger specific heat capacity of Si, this photodiode could be operated at higher bias voltages of 7V and 8V, thus higher power dissipation, even though no additional heat sink was mounted. The highest operating current without saturation was ~50mA at 8V reverse bias. The maximum total dissipated power was more than 1.5 times higher than that of the same photodiode on InP. The maximum output RF power also increased from 14dBm to 16dBm.

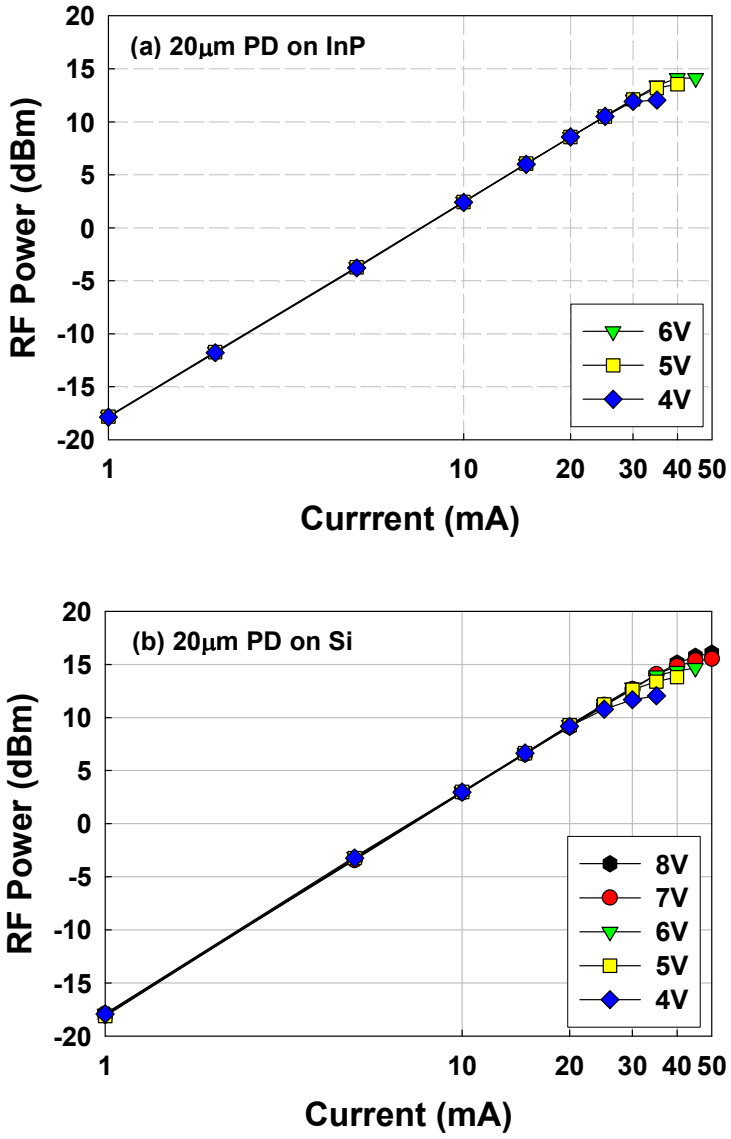

Figure 6.8 Measured output RF power versus photocurrent at 10GHz for: (a) a 20μm-diameter photodiode on an InP substrate and (b) a 20μm-diameter photodiode bonded on a Si wafer

6.5 Summary

High power photodiodes wafer bonded to Si using a gold intermediate layer were demonstrated. The gold bonding process is a low-temperature, uniform process. The bonded photodiodes have better heat conduction due to the higher thermal conductivity of Si, and a higher responsivity due to the resonant cavity formed with the Au bottom mirror. A 20μm-diameter photodiode exhibited a peak responsivity of ~1A/W, a bandwidth of ~18GHz and a large-signal saturation-current of ~50mA. Both the responsivity and the saturation current of the Au-bonded photodiode were improved compared to a photodiode with the same structure on an InP substrate. Using the same bonding method, we can transfer photodiodes to other substrates with even higher thermal conductivity and/or heat spreading capability to further improve heat conduction. In cases where a heat sink or cooling system is needed, this method can significantly improve the cooling efficiency.

Chapter 7: Avalanche Photodiode with Undepleted Absorber (UA-APD)

7.1 Introduction

Differing from a p-i-n photodiode, an avalanche photodiode (APD) is designed to have internal gain, which originates from carrier impact ionization in a high electric-field multiplication region. This internal gain can boost the sensitivity of the optical receiver in long haul and metro optical communication systems, if the APD has good responsivity, high gain-bandwidth product and low excess noise characteristics [7-1]-[7-4]. The single photon counting avalanche photodiode (SPAD) [7-5] is another type of photodiode that attracted more and more attention recently, due to its applications in quantum cryptography, spectroscopy and imaging. In APDs designed for all these applications, the absorption layers are usually depleted in order to ensure high speed collection of photo-generated carriers. In this chapter, a new APD structure with an undepleted absorber is described. The potential advantage of using it in both communication and photon counting applications is also discussed.

7.2 Device structure and property analysis

7.2.1 Device structure

Figure 7.1 shows the layer diagram of the proposed undepleted-absorber APD (UA-APD) structure with an InGaAs absorption layer. It consists (from top to bottom) of an InGaAs p-contact layer, a p-InAlAs diffusion blocking layer, a graded p-doped InGaAs absorption layer, an InGaAlAs compositional grading layer, an InAlAs charge layer, an InAlAs multiplication layer, and an InAlAs n-contact layer. It is similar to the high gain-bandwidth product, low excess noise APDs reported in [7-1]-[7-4] and the single-photon counting APD in [7-5], except that the InGaAs absorption layer is p-type doped and not depleted.

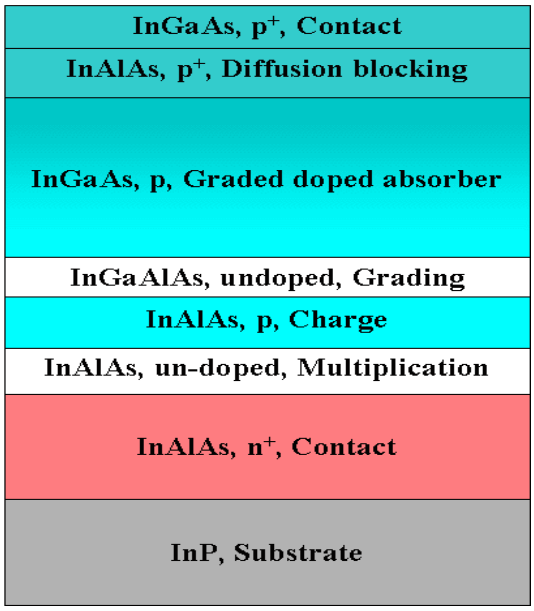

Figure 7.1 Schematic layer structure of an APD with undepleted InGaAs absorber

7.2.2 Carrier transport analysis

At unity gain, the operation of this APD is similar to the uni-traveling-carrier (UTC) photodiode [7-6]. The photo-generated holes respond within the dielectric relaxation time, which is on the order of femtoseconds [7-7]. The photo-generated electrons travel from the p-type absorbing layer to the wide bandgap depletion region by diffusion and drift. The doping in the p-InGaAs is graded so that a built-in electric field is formed in the InGaAs absorber. The built-in field can be calculated as

$$E = \frac{kT}{p(x)} \cdot \frac{dp(x)}{dx}$$

A gradient doping from 2×10^{18}cm^{-3} to 2×10^{17}cm^{-3} in the 450nm-thick InGaAs will give a built-in electric field of ~1.3kV/cm.

The carrier transport process for this device can be solved using the following diffusion-drift equation and boundary conditions,

$$\frac{\partial n}{\partial t} = D_e \frac{\partial^2 n}{\partial x^2} - v_d \frac{\partial n}{\partial x} - \frac{n}{\tau} + G$$

$$\left(\frac{\partial n(x,t)}{\partial x} - v_d n\right)\Big|_{x=0} = 0$$

$$n(x,t)\big|_{x=d} \approx 0$$

where n is the electron density, D_e is the electron diffusivity, v_d is the drift velocity caused by the built-in field, τ is the carrier lifetime, G is the generation rate, x=0 is the border between the absorber and the diffusion blocking layer, and

x=d is the border between the absorber and the depletion region. A solution of the above equations was given in Reference [7-8]. When there is no built-in electric field, the travel time of an electron in the 450nm InGaAs absorbing layer is determined solely by diffusion is ~10ps [7-9]. Considering high minority mobility (~5000cm^2/V/S in InGaAs with a p doping of $1\times10^{18}cm^{-3}$ [7-9]) and the overshoot velocity, the built-in electric field can reduce the carrier transit time in the absorption region significantly [7-8, 7-9].

When the UA-APD is biased in the avalanche gain regime, the secondary holes do not need to travel all the way through the InGaAs absorbing layer before being collected by the p-doped layer. Thus, they have a much shorter transit path than in conventional separate absorption, charge and multiplication (SACM) APD structures with the same absorption layer thickness. At high gain, the undepleted absorber is expected to have very little influence on the gain-bandwidth product, which is mainly determined by the ionization process in the multiplication region. However, at low gains, the bandwidth is expected to improve, due to a reduction in carrier transit time, which is the dominant factor limiting the device bandwidth. If this can be achieved, APDs would potentially operate at 40Gb/s. Due to the limitation of the gain-bandwidth product, the 40Gb/s APDs that have been reported to date [7-10] operate at gains less than 4 or 5, where the bandwidth is

still mainly limited by the carrier transit time. Increasing the low-gain bandwidth would result in improved performance for high speed operation.

7.2.3 Dark current analysis

Dark current is another important APD performance parameter [7-11], particularly for APDs that operate as single photon counting or Geiger mode detectors [7-5, 7-12]. For the UA-APD, reduced dark current is expected for two reasons. First, since the electric field is negligible in the InGaAs region, there is minimal tunneling dark current in this type of APD. Second, the generation-recombination part of the dark current in InGaAs is much lower when it is not depleted. Some calculations for the generation-recombination dark current will be presented in the following.

For the APD with depleted InGaAs, the generation-recombination dark current in InGaAs can be calculated as

$$G_i = \frac{q \cdot n_i \cdot V}{\tau_{eff}}$$

where n_i is the intrinsic carrier concentration, τ_{eff} is the effective carrier lifetime, V is the volume of InGaAs, and q is the charge of an electron.

For the p-InGaAs in UA-APDs, the p-InGaAs layer thickness is much less than the electron diffusion length (~9μm [7-13] for 1×10^{18}cm^{-3} p-doping), thus all of the electrons that are thermally generated in the p-InGaAs are collected by the

high field depletion region. Therefore, the dark current contributed by the p-InGaAs can be calculated from the thermal generation rate equation

$$G_p = \frac{q \cdot n_p \cdot V}{\tau_n}$$

where n_p is the electron concentration, and τ_n is the nonradiative minority carrier lifetime.

Based on the above equations, a comparison of the thermal generation current from InGaAs layers in APDs with depleted and undepleted absorbers is shown in Table 7.1. The InGaAs layer is usually the main source of the dark current in a conventional APD due to its narrow bandgap. For the carrier lifetime value used in the calculation in Table 7.1, the InGaAs in the UA-APD generates several orders of magnitude lower dark current than that in the depleted absorber APD. This will ensure that InGaAs is no longer the dominant source of dark current in the UA-APD, an attractive property for photon counting applications.

Device type	APD with depleted InGaAs absorber	APD with undepleted InGaAs absorber
Thermal generation rate equation in InGaAs	$G_i = n_i/\tau_{eff}$	$G_p = n_p/\tau_n = n_i^2/(N_A \cdot \tau_n)$
Material parameters at 300K	$n_i = 6.3\times10^{11}\text{cm}^{-3}$ [7-14] τ_{eff} = 0.34~1.7μs [7-15] (for $N_D = 1\sim3\times10^{15}\text{cm}^{-3}$)	$n_i = 6.3\times10^{11}\text{cm}^{-3}$ [7-14] τ_n = 20ns [7-14] (for $N_A = 1\times10^{18}\text{cm}^{-3}$)
Calculated thermal generation rate in InGaAs	$G_i = 3.7\times10^{17}\text{s}^{-1}\text{cm}^{-3}$ (for τ_{eff} = 1.7μs)	$G_p = 1.9\times10^{13}\text{s}^{-1}\text{cm}^{-3}$

Table 7.1 Thermal generation rate calculation in InGaAs layers of APDs with depleted and undepleted absorbers

7.2.4 Other properties

Another advantage of this structure, compared to the SACM APD, is that there is no impact ionization in the absorbing layer, which degrades the noise and gain-bandwidth product [7-16]. In the undepleted absorber structure, the breakdown and punch-through voltages can be easily designed by controlling the electric field intensity in the multiplication layer. The electric field intensity in the absorption layer is negligible because it is almost neutral as a result of the high p doping. Most of the bias voltage is applied to the multiplication layer. The electric field intensity in the multiplication layer is dominated by the doping level and

thickness of the charge layer. This is a very desirable feature from a device engineering perspective.

Compared to the depleted absorbing layer structure, the undepleted absorber APD has lower operating bias voltage because all of the bias was applied across the multiplication layer.

7.3 Experimental results and discussion

7.3.1 UA-APD with 450nm-thick InGaAs

An UA-APD wafer structure, as shown in Figure 7.2, was designed and grown in a modified Varian Gen-II molecular beam epitaxy (MBE) reactor at the University of Texas at Austin, on semi-insulating (Fe doped) InP substrates. It consists of an 800nm n^+ $In_{0.52}Al_{0.48}As$ buffer layer, a 150nm undoped $In_{0.52}Al_{0.48}As$ multiplication layer, a 90nm Be doped (4×10^{17} cm^{-3}) $In_{0.52}Al_{0.48}As$ charge layer, a 100nm undoped $In_{0.52}Al_{0.48}As$ drift layer, a 50nm undoped InGaAlAs grading layer, a 450nm p-type $In_{0.53}Ga_{0.47}As$ absorbing layer, a 200nm p-type $In_{0.52}Al_{0.48}As$ diffusion blocking layer, and a 30nm heavily Be-doped $In_{0.53}Ga_{0.47}As$ p-contact layer.

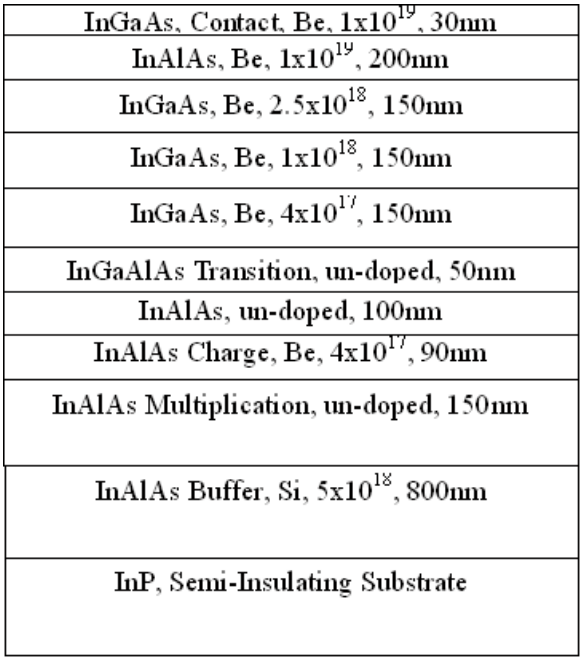

Figure 7.2 Schematic layer structure of the UA-APD with 450nm InGaAs

The calculated band diagram of the device at 17V reverse bias is shown in Figure 7.3. The doping in the p-type absorber was "graded" in three 150nm-thick steps (4×10^{17} cm^{-3}, 1×10^{18} cm^{-3}, and 2.5×10^{18} cm^{-3}) to form a quasi-electric field to aid carrier transport in the absorbing layer. The absorbing layer band tilt can be seen in the diagram. The 50nm-thick composition-graded InGaAlAs quaternary layer was used to reduce the abrupt conduction band barrier at the $In_{0.53}Ga_{0.47}As/In_{0.52}Al_{0.48}As$ heterojunction interface.

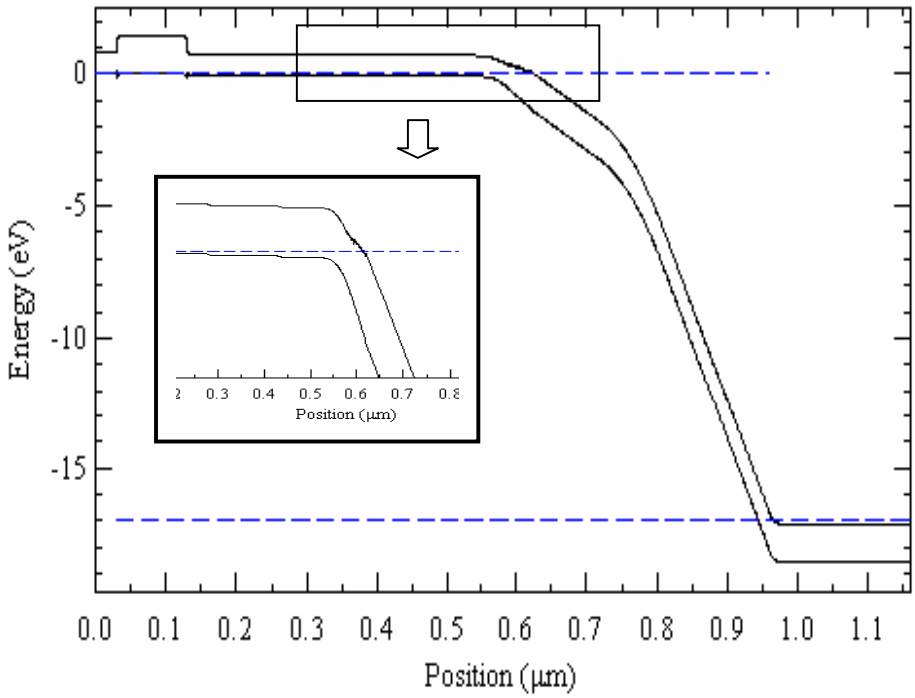

Figure 7.3 Calculated band diagram for the undepleted absorber APD at 17V reverse bias. Inset: a close up diagram of the graded InGaAs absorption layer and InGaAlAs transition layer.

The wafer was fabricated into a top illuminated mesa structure using conventional photolithography, wet chemical etching, SiO_2 passivation, and lift off metallization techniques. Microwave contact pads were fabricated for high-speed measurements.

Figure 7.4 shows a typical I-V curve for a 20μm diameter device. The breakdown voltage is only ~17V because the depletion region is very thin (390nm). Gains in excess of 200 were achieved. The dark current was ~300pA

(~1×10^{-4}A/cm^2) at 90% of breakdown. At gains of 10 and 56 the dark current was ~1nA (~3.2×10^{-4}A/cm^2) and ~5nA (~1.6×10^{-3}A/cm^2), respectively. The total dark current can be expressed in terms of the multiplied and unmultiplied dark current components. The multiplied dark current was ~87pA (~2.8×10^{-5}A/cm^2) and the unmultiplied dark current was ~23pA (~7.3×10^{-6}A/cm^2). The linear relation between the dark current and gain holds up to a gain of 56.

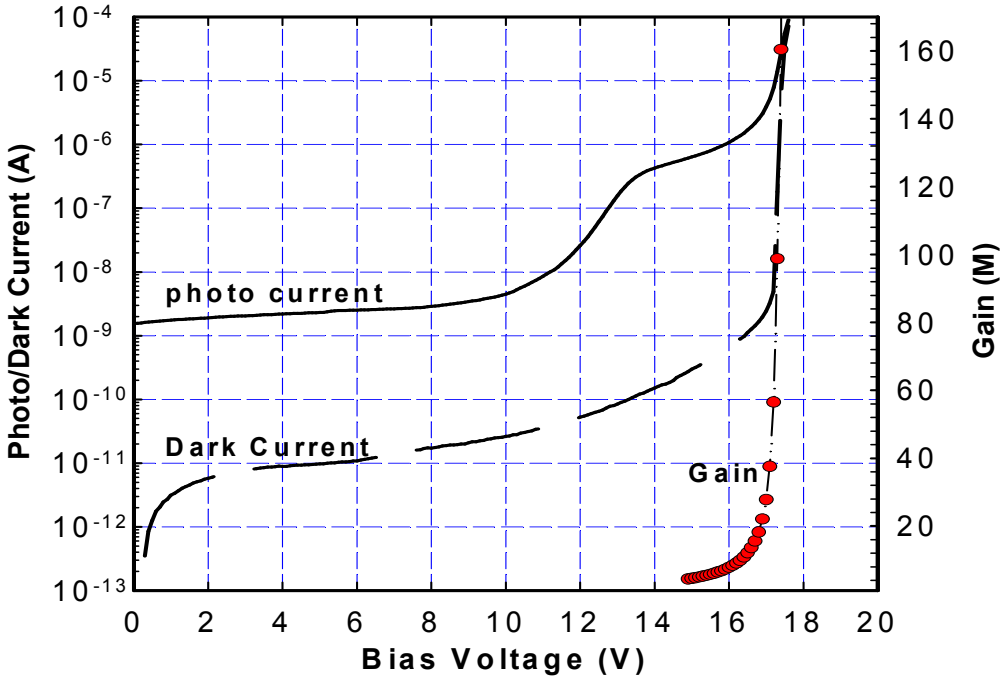

Figure 7.4 Typical DC photocurrent, dark current, and gain as a function of reverse bias voltage for a 20μm diameter device

It is clear from Figure 7.4 that the unity gain quantum efficiency can not be measured directly, because there is a small gain at the punch-through voltage. We have estimated a lower limit for the gain at punch-through from measurements of the responsivity. The transmission coefficient of a 2200Å SiO_2 AR coating was calculated to be ~ 90%. With this transmission, assuming an absorption coefficient of $0.67\mu m^{-1}$ at 1.55μm [7-17], the quantum efficiency of a 450nm-thick $In_{0.53}Ga_{0.47}As$ absorbing layer was calculated to be 23%. At 15V, the measured quantum efficiency was 102%, which indicated a gain of ~4.4 at this bias. This value was used as a reference to calculate the gain at different biases.

To reinforce the gain measurement described above, the carrier multiplication process in this structure was simulated using a Monte Carlo model [7-18]. The impact ionization parameters for the $In_{0.52}Al_{0.48}As$ material were extracted by first fitting measured gain and noise for a series of $In_{0.52}Al_{0.48}As$ APDs of different thickness [7-19]. The simulation tool was then applied to a wide range of structures fabricated from this material. The simulated and measured gain versus bias for this device is shown in Figure 7.5. There is very good agreement between the two curves. The simulated result also shows a gain of ~4.4 at 15V confirming the estimation from the quantum efficiency measurements.

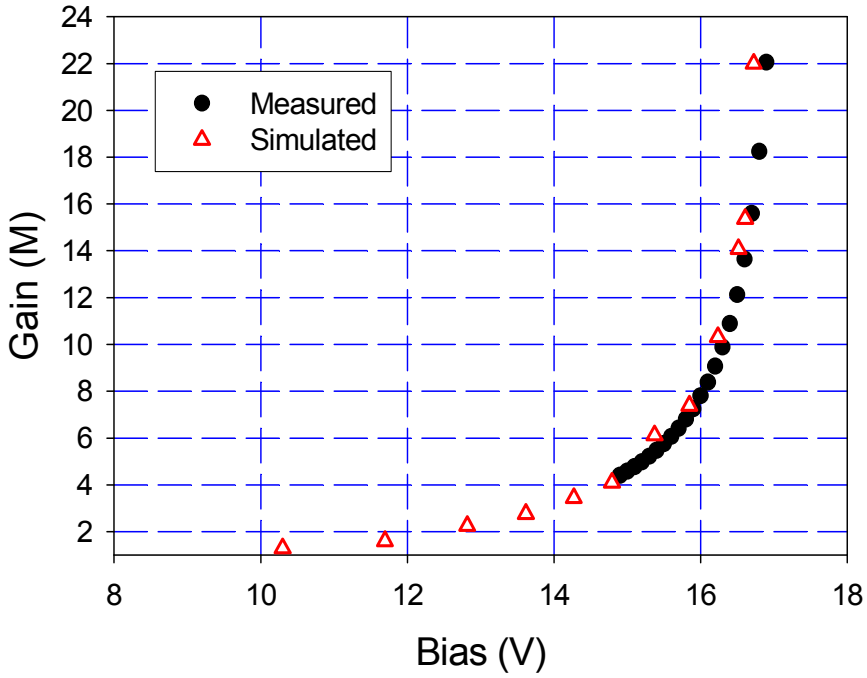

Figure 7.5 Simulated and experimental gain value as function of bias voltage

The excess noise factor, F(M), of these APDs was measured using a HP8970B noise figure meter and a standard noise source [7-20]. The determination of F(M) is complicated by the fact that the noise value at unity gain is not known. We have again used Monte Carlo simulations to find an F value of 1.63 at a gain of 4.4. We used this as a reference point to measure F(M) at higher gains. The measured and simulated F(M) values are shown in Figure 7.6. The effective k value was estimated to be 0.15. This is consistent with previous

measurements [7-1, 7-19] of APDs with comparably thin $In_{0.52}Al_{0.48}As$ multiplication layers.

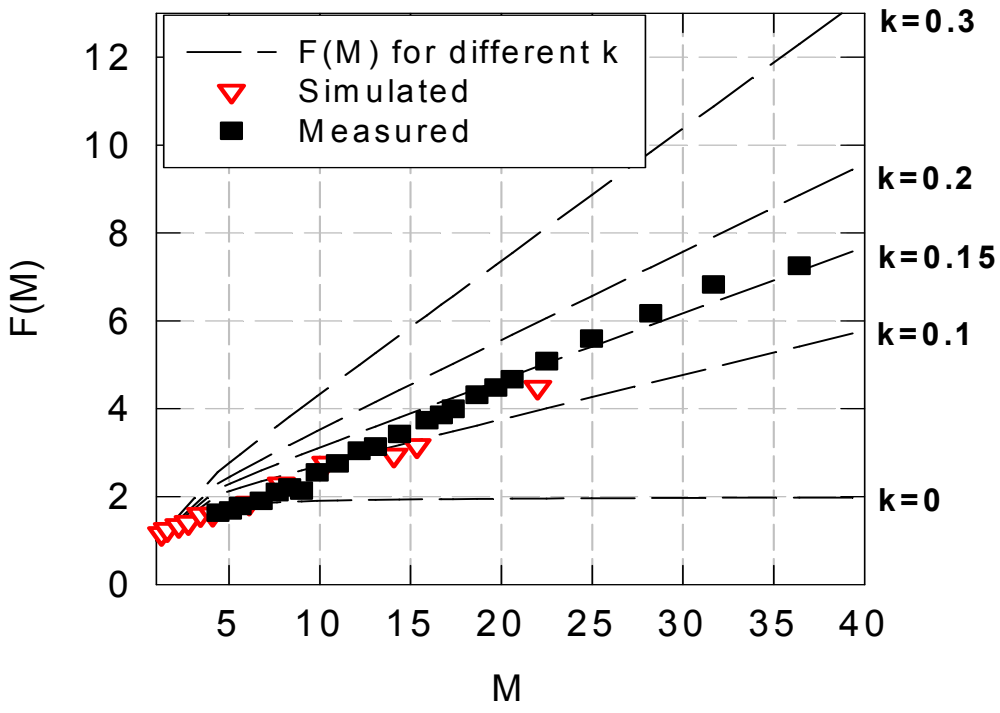

Figure 7.6 Simulated and experimental excess noise factor as a function of gain

RF response measurements were made using a small-signal optical heterodyne setup. Figure 7.7 shows the measured 3dB bandwidth of a 16μm diameter mesa device versus gain. A gain-bandwidth product of 160GHz was achieved. The low gain bandwidth was ~20GHz, and limited primarily by carrier trapping at the InGaAs/InAlAs interface. The conduction band barrier between

these two materials is ~0.5eV [7-7]. Although the interface is graded, there is still carrier trapping at the graded interface, since the photo-generated electrons do not get energized in the undepleted absorber.

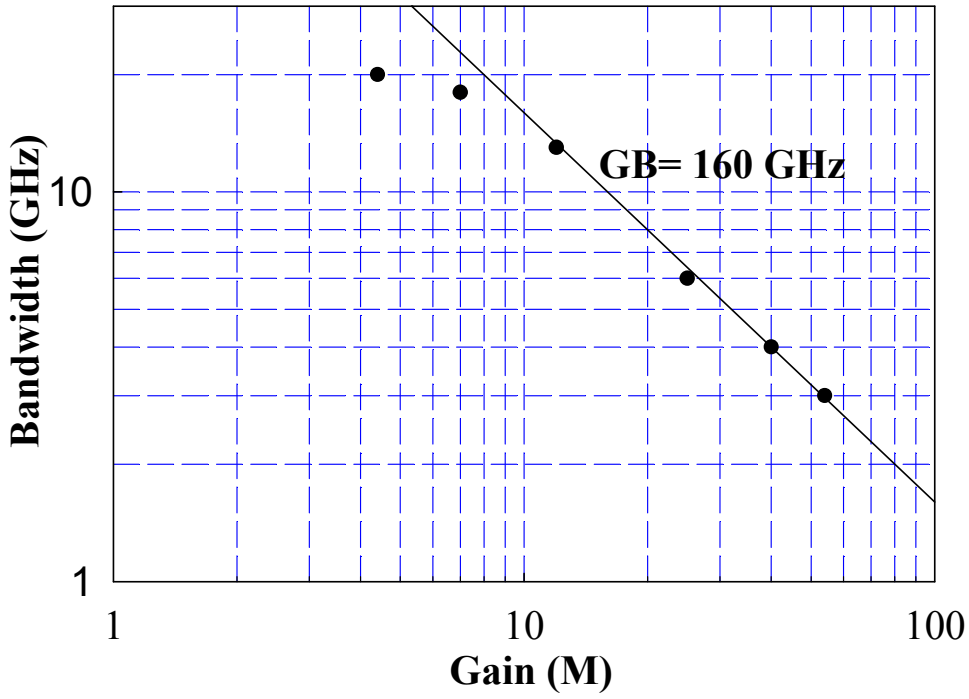

Figure 7.7 The measured 3dB bandwidth versus gain for a 16μm diameter device

This carrier trapping could be reduced by using a better grading layer or a smaller conduction band barrier. Following our report of the above device [7-21], Y. Hirota et al. utilized our idea of using an undepleted absorber APD and changed the depletion layer from InAlAs to InP [7-22]. The main advantage of using an InP multiplication layer is a much smaller conduction band barrier

(~0.24eV [7-7]) at the interface with InGaAs. This modified device demonstrated low-gain bandwidth as high as 40GHz and a gain-bandwidth product of 140GHz.

7.3.2 UA-APD with 1μm-thick InGaAs

To increase the quantum efficiency, an UA-APD with 1μm-thick InGaAs absorber was designed and characterized. The structure is shown in Figure 7.8. The InGaAs absorber is graded doped from $3\times10^{18}cm^{-3}$ to $2\times10^{17}cm^{-3}$ to form a built-in electric field. The multiplication layer has an impact ionization engineered structure [7-23] to reduce excess noise and increase the gain-bandwidth product.

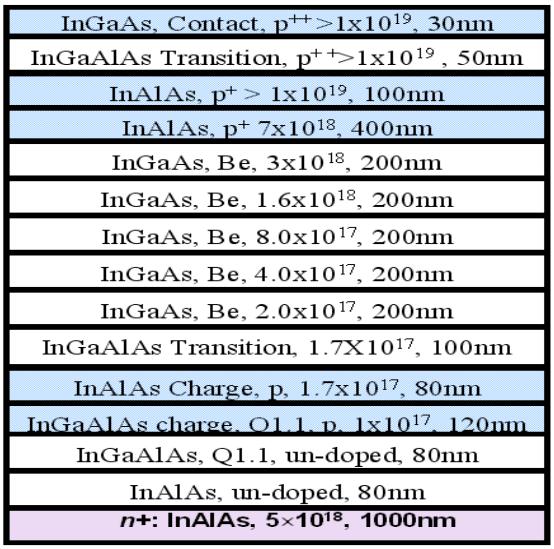

Figure 7.8 Schematic layer structure of the UA-APD with a 1μm-thick InGaAs and impact ionization engineered multiplication layer

The ratio of the measured responsivity at punch-through to the calculated unity gain responsivity was ~1.6. During characterization, this value was used as

a reference to calculate gains at different biases. The measured bandwidth versus gain is shown in Figure 7.9. The bandwidth at low-gain of this device is ~12GHz up to a gain of eight. It is worth noting that this low-gain bandwidth is higher than the reported low-gain bandwidth (~9GHz) of the depleted absorber APD with the same InGaAs thickness [7-24]. Tunneling dark current can be observed near breakdown due to the thin quaternary multiplication layer. The excess noise factor was also measured, yielding an effective k value of ~0.15.

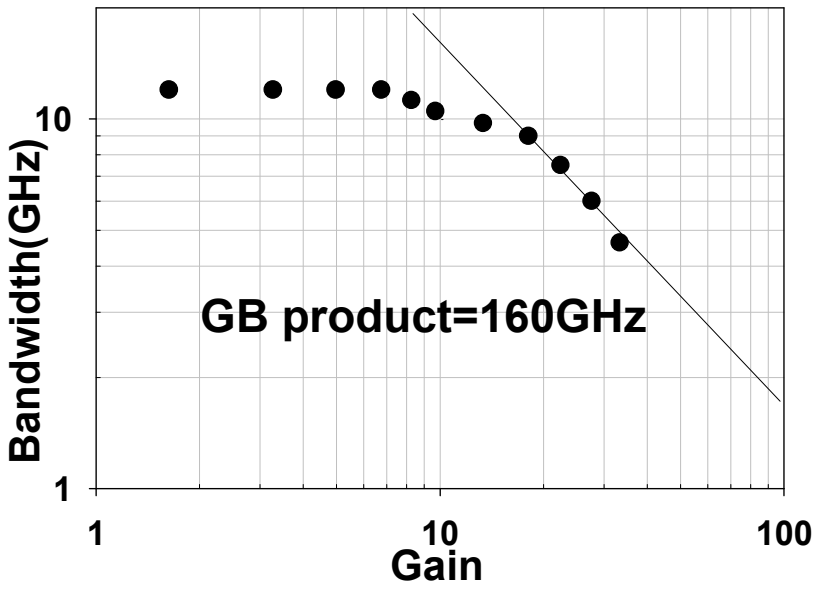

Figure 7.9 Measured bandwidth versus gain for the APD structure in Figure 7.8

7.4 Summary

A new type of APD with an undepleted absorber was proposed and analyzed theoretically. InGaAs/InAlAs APDs with 450nm-thick and 1μm-thick undepleted InGaAs absorbers were designed, fabricated and characterized. The fabricated APDs demonstrated similar gain-bandwidth products and excess noise characteristics as APDs with depleted absorber. With proper design optimization of the heterojunction between the InGaAs absorber and the InAlAs multiplication layer, higher low-gain bandwidth can be expected. Due to the suppression of tunneling and generation-recombination current, very low dark current was achieved. Further study is needed on the performance of this type of device in Geiger mode.

Chapter 8: Summary and Future Work

8.1 Summary

An analysis of photodiode saturation mechanisms for the large-signal modulation case was presented. The analysis shows that for small high-speed devices, the space charge effect is prominent and needs to be minimized for high output operation; whereas, for photodiodes working at moderate or low frequencies, the main limiting factor of the device output RF power was found to be the DC bias limited voltage swing. Based on this analysis, two types of improved UTC photodiodes were designed and experimentally studied. At high frequency, charge-compensated UTC photodiodes delivered 20dBm at 20GHz, and 17dBm at 40GHz; at lower frequency, a UTC photodiode with thick depletion region delivered 25dBm at 6GHz, all record high output RF power values at the respective frequencies.

In order to suppress laser RIN in high-power analog fiber-optic links, high-power top-illuminated balanced photodetectors were demonstrated. High saturation current, good broadband common mode rejection ratio and good noise suppression were achieved. A thick p-type window layer was used to reduce the p-layer lateral resistance in this top illuminated structure. In order to increase the responsivity, balanced evanescently-coupled short-multimode waveguide

photodiodes (SMWP) were designed, fabricated and characterized. Very high-responsivity, low polarization dependence, and broad bandwidth were achieved.

High-power photodiodes were wafer bonded to Si using a gold intermediate layer to improve photodiode heat conduction. A uniform, low temperature gold bonding process was developed. The responsivity of the top illuminated photodiode increased from 0.32A/W to 1A/W (peak) due to the resonant cavity formed with the Au bottom mirror.

A new type of APD with an undepleted absorber (UA-APD) was proposed and studied theoretically and experimentally. Theoretically, this structure has the advantage of high low-gain bandwidth, low dark current, no multiplication in the absorber and low breakdown voltage. The fabricated UA-APDs demonstrated a similar gain-bandwidth product and excess noise characteristic as APDs with depleted absorbers. Low dark current was observed.

8.2 Future work

8.2.1 Future work for high power photodiodes

In order to achieve saturation current for small-signal modulation (modulation depth <5%), it is advantageous to use a thin depletion region in order to reduce the space charge effect. Also, it is beneficial to operate at low bias voltage in order to reduce thermal loading. As analyzed in Chapter 3, the load

voltage swing factor comes into play for large signal (modulation depth ~100%) operation, thus the DC bias and heat dissipation have to be increased in order to increase the RF output power. This favors photodiodes with thick depletion layers. However, a thicker depletion region results in a larger space charge effect. Therefore, there exists a trade off. Another trade off involving depletion region thickness is between the device capacitance and the carrier transit time. A thicker depletion region reduces the capacitance but increase the carrier transit time. These considerations make the optimized depletion layer thickness of high-output-power photodiodes different for different operation frequencies. As new application areas arise, the analysis in Chapter 3 can be used as a guide for optimizing the design of high-output-power photodiodes for different operation frequency ranges.

Using the gold bonding method, high power photodiodes can be transferred to substrates with even higher thermal conductivity than Si. Table 8.1 lists the thermal conductivity of several materials at 300K. SiC, AlN and diamond all have higher thermal conductivity than Si. Bonding the high-power photodiodes to those substrates can further improve the heat conduction, thus maximizing the output power.

Material	InGaAs	InP	Si	4H-SiC	AlN	Diamond
k (W/cm-K)	0.05	0.68	1.5	3.7	3.0	22

Table 8.1 Thermal conductivity (k) of various materials at 300K

In the current wafer bonding approach, the bonding interface is on the n-InP side of the photodiode, as shown in Figure 8.1 (a). This configuration was chosen to have a smaller thermal impedance between the depletion region and the bonding interface and to provide a better comparison to devices on InP substrates. In a UTC PD structure, the InGaAs absorber is on the p-side of the depletion region. As can be seen in Table 8.1, InGaAs has much poorer thermal conductivity than InP. However, this configuration has the drawback of high p-layer lateral resistance. To eliminate this high p-layer lateral resistance problem, the configuration in Figure 8.1 (b) is proposed. This will lead to higher thermal impedance for a UTC-PD, since the heat generated in the depletion region has to go through the high thermal impedance of the p-InGaAs absorber to reach the bonding interface. However, for a PIN structure with InP layers on both sides of the InGaAs, the thermal impedance between the depletion region and the bonding interface is similar in both configurations.

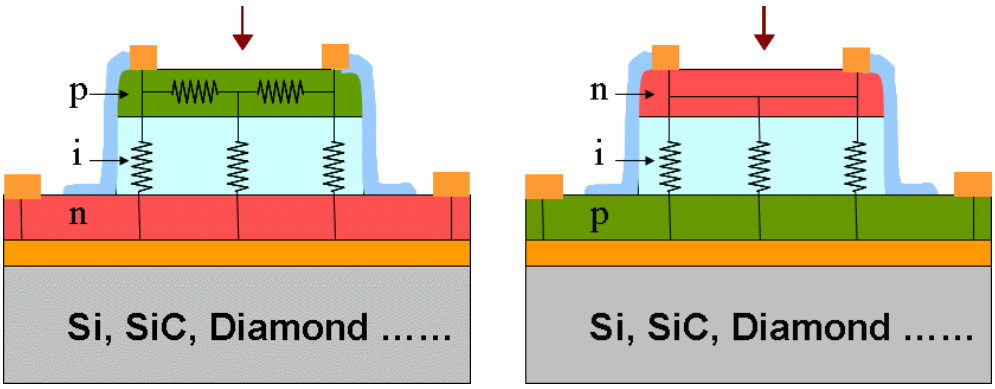

(a) (b)

Figure 8.1 Schematic layer structure for gold wafer bonded high-power photodiodes with (a) the n-layer close to the bonding interface and (b) the p-layer close to the bonding interface

.Using a transparent electrode is another way to reduce the lateral resistance in the top-illuminated photodiode structures shown in Figure 8.1. At 1.55μm, a transparent electrode with transmittance of ~80% and a sheet resistance of 7Ω/□ has been reported [8-1]. This sheet resistance value is much smaller than can be achieved with a highly doped 1μm-thick p-InP layer. Therefore, the current crowding can be effectively reduced. Using a transparent electrode can also increase the illumination area for the top-illuminated photodiodes, by eliminating the gold contact ring, which blocks the light. This will yield smaller space charge density in the photodiode depletion region for the same photocurrent.

A TE cooling system can further improve the maximum heat dissipation on the photodiode. However, for the devices on InP substrates, mounting a TE

cooler on the backside of the substrate is not very helpful, because of the high thermal impedance of the InP substrate. Bonding the photodiode directly to the TE cooler is not efficient either, because the heat source (photodiode) diameter is too small, and the cooling power of the TE cooler is proportional to the contact area. An effective approach is to first bond the high power photodiode to a submount with very high thermal conductivity or heat spreading capability. Subsequently, the TE cooler can be attached to the backside of the submount. In this way the heat generated from the photodiode can be spread to a much larger area providing better thermal conduction. The ideal materials for the submount might be diamond or heat spreading ceramics.

Finally, the resonant cavity in the gold bonding structure can be optimized to get higher responsivity. With a 0.45μm-thick InGaAs absorber, a top mirror with a reflectivity of 50% will give a quantum efficiency close to 100%.

8.2.2 Future work for avalanche photodiodes

Theoretical calculations in Chapter 7 show that the undepleted absorber APD (UA-APD) has lower dark current than a depleted absorber structure. In experiments, low dark current was observed for fabricated UA-APDs. This is a very desirable feature for photon counting applications. Further investigation is still needed to test the performance of using UA-APDs as single photon counters.

If the grading layer at the hetero-interface between the InGaAs absorber and the InAlAs multiplication region can be further optimized in the UA-APD, a higher low-gain bandwidth may be obtainable. Although the interface is graded in the current structure, the photo-generated electrons do not gain much energy in the absorber, thus carrier trapping is still a concern. One way to avoid carrier trapping is to use materials with a type II heterojunction band lineup. $GaAs_{0.51}Sb_{0.49}$ is lattice matched to InP and absorbs at 1.55μm. The conduction band edge of $GaAs_{0.51}Sb_{0.49}$ is 0.11eV above that of InP [8-2]. Figure 8.2 shows the simulated band diagram of a UA-APD with a $GaAs_{0.51}Sb_{0.49}$ absorber and an InP multiplication region. Very little or no carrier trapping is expected in this structure, since there is no conduction band barrier for electrons to travel from the absorber to the multiplication region. The UA-APD structure could also be used in devices with other materials at other operating wavelengths to reduce the dark current.

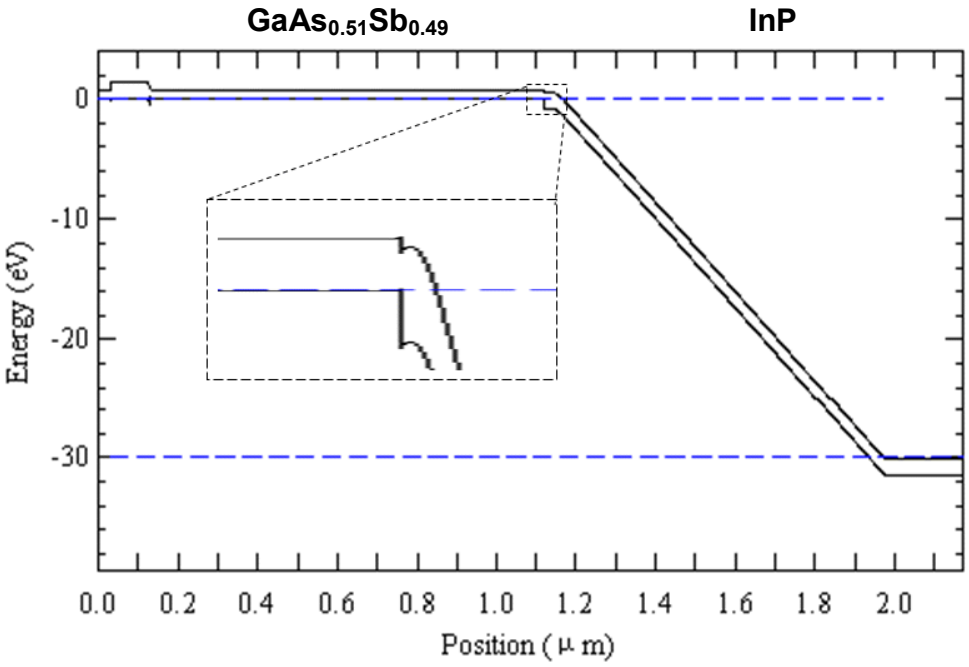

Figure 8.2 Simulated band diagram of UA-APD with GaAsSb absorption layer

Appendix: Publications

Journal Papers:

[1] **N. Li**, X. Li, S. Demiguel, X. Zheng, J. C. Campbell, D. A. Tulchinsky, K. J. Williams, T.D. Isshiki, G.S. Kinsey, R. Sudharsansan, "High-Saturation-Current Charge-Compensated InGaAs/InP Uni-Traveling-Carrier Photodiode," *IEEE Photonics Technology Letters*, Vol. 16 No.3, pp864-866, Mar. 2004

[2] **N. Li**, R. Sidhu, X. Li, F. Ma, X. Zheng, S. Wang, G. Karve, S. Demiguel, A. L. Holmes, Jr., and J. C. Campbell, "InGaAs/InAlAs Avalanche Photodiode with Undepleted Absorber," *Applied Physics Letters*, Vol. 82 No.13, pp2175-2177, Mar. 2003

[3] **N. Li**, H. Chen, S. Demiguel, X. Li, J. C. Campbell, T.D. Isshiki, G.S. Kinsey, R. Sudharsansan, "High-Power Charge-Compensated Uni-Traveling-Carrier Balanced Photodetector," *IEEE Photonics Technology Letters*, Vol.16, No.10, pp2329-2331, Oct. 2004

[4] **N. Li**, R. Sidhu, X. Li, F. Ma, S. Demiguel, X. Zheng, A. L. Holmes Jr., D. Tulchinsky, K. J. Williams, "Charge-Compensated High-Saturation-Current InGaAs/InAlAs Uni-Traveling-Carrier Photodiode," *Phys. Stat. Sol.* (a) 201, N.13,pp3037-3041, 2004

[5] **N. Li**, S. Demiguel, H. Chen, X. Zhang, J. C. Campbell, J. Wei, H. Lu, A. Anselm "Planar Short-Multimode Waveguide Evanescently-Coupled Balanced Photodetectors with Fully Depleted and Partially Depleted Absorber," submitted

[6] F. Ma, **N. Li**, J. C. Campbell, "Monte Carlo Simulations of the Bandwidth of InAlAs Avalanche Photodiodes," *IEEE Transactions on Electron Devices*, Vol. 50, Issue 11, pp2291 – 2294, Nov. 2003

[7] S. Demiguel, **N. Li**, X. Li, X. Zheng, J. Kim, J. C. Campbell, H. Lu, and K. A. Anselm, "Very High-Responsivity Evanescently-Coupled Photodiodes Integrating a Short Planar Multimode Waveguide for High-Speed Applications," *IEEE Photonics Technology Letters*, Vol. 15, Dec. 2003

[8] X. Li, **N. Li**, S. Demiguel, J. C. Campbell, D. Tulchinsky, K. J. Williams, "A Comparison of Front- and Backside-Illuminated High-Saturation Power

Partially Depleted Absorber Photodetectors," *IEEE Journal of Quantum Electronics*, Vol. 40, pp1321 - 1325, Sept. 2004

[9] X. Li, **N. Li**, S. Demiguel, J. C. Campbell, D. Tulchinsky, K. J. Williams, "High-Saturation-Current InP-InGaAs Photodiode with Partially Depleted Absorber," *IEEE Photonics Technology Letters*, Vol. 15 pp1276-1278, Sept. 2003

[10] X. Li, **N. Li**, S. Demiguel, X. Zheng, J. C. Campbell, H. H. Tan, C. Jadadish, "A Partially Depleted Absorber Photodiode With Graded Doping Injection Regions," *IEEE Photonics Technology Letters*, Vol. 16 pp2326-2328, Oct. 2004

[11] S. Demiguel, X. Zheng, **N. Li**, X. Li, J. C. Campbell, J. Decobert, N. Tscherptner,A. Anselm, **"**High-Responsivity and High-Speed Evanescently-Coupled Waveguide Avalanche Photodiode," *Electronics Letters*, Vol. 39, pp1848-1849 Dec. 2003

[12] X. Li, S. Demiguel, **N. Li**, J. C. Campbell, D. Tulchinsky, K. J. Williams, "Backside illuminated high saturation current partially depleted absorber photodetectors,**"** *Electronics Letters*, Vol. 39 pp1466-1467, Oct. 2003

[13] D. Tulchinsky, X. Li, **N. Li**, S. Demiguel, J. C. Campbell, K. J. Williams, "High saturation current, wide bandwidth photodetectors," *IEEE Journal on Selected Topics in Quantum Electronics*, Vol. 10, Issue 4, pp. 702 – 708, 2004

[14] G. Karve, X. Zheng; X. Zhang; X. Li, **N. Li**, S. Wang, F. Ma, A. Holmes, Jr., J.C Campbell, G.S Kinsey, J.C. Boisvert, T.D Isshiki, R. Sudharsanan, D.S. Bethune, W.P. Risk, "Geiger mode operation of an $In_{0.53}Ga_{0.47}As$-$In_{0.52}Al_{0.48}As$ avalanche photodiode," *IEEE Journal of Quantum Electronics*, Vol. 39, pp1281-1286, Oct. 2003

[15] N. Duan, S. Wang , X. Zheng, X. Li, **N. Li**, J. C. Campbell, C. Wang and Larry A. Coldren, "Detrimental Effect of Impact Ionization in the Absorption Region on the Frequency Response and Excess Noise Performance of InGaAs/InAlAs SACM Avalanche Photodiodes" *IEEE Journal of Quantum Electronics*, Vol.41, No.4, pp568 – 572, April 2005

[16] S. Wang, R. Sidhu, G. Karve, F. Ma, X. Li, X. Zheng; J.B. Hurst, X. Sun, **N. Li**, A.L. Holmes, Jr., J.C. Campbell, "A study of low-bias photocurrent

gradient of avalanche photodiodes," *IEEE Transactions on Electron Devices*, Vol. l49, pp2107–2113, Dec. 2002

[17] **N. Li**, Y. Han, Z. Hao, C. Sun, Y. Luo "Direct wafer bonding of InP materials," *Chinese Journal of Semiconductors*, Vol. 22, pp1217-1221, Sept. 2001 (in Chinese)

[18] **N. Li**, Q. Jin, "Statistical dead-time correction of a time-of-flight mass spectrometer (TOFMS)," *Vacuum and Cryogenics*, No. 71, pp233-237, Dec. 1999 (in Chinese)

Conference Presentations:

[19] **N. Li**, X. Li, S. Demiguel, X. Zheng, J. C. Campbell, D. A. Tulchinsky, K. J. Williams, T.D. Isshiki, G.S. Kinsey, R. Sudharsansan, "High-Saturation-Current Charge-Compensated InGaAs/InP Uni-Traveling-Carrier Photodiode, " *2003 IEEE/LEOS Annual Meeting Conf. Proc.*, Tucson, AZ, pp790–791, Oct. 2003

[20] **N. Li**, H. Chen, S. Demiguel, X. Li, J. C. Campbell, T.D. Isshiki, G.S. Kinsey, R. Sudharsansan, "High-Power InGaAs/InP Charge-Compensated Uni-Traveling-Carrier Balanced Photodetector," *2004 IEEE/LEOS Annual Meeting Conf. Proc.*, Puerto Rico, Paper TuH1

[21] **N. Li**, S. Demiguel, H. Chen, X. Zhang, J. C. Campbell, J. Wei, H. Lu, A. Anselm "Planar Short-Multimode Waveguide Evanescently-Coupled Balanced Photodetectors with Fully Depleted and Partially Depleted Absorber," *2005 Optical Fiber Communication Conference*, Anaheim, CA

[22] **N. Li**, H. Chen, N. Duan, M. Liu, S. Demiguel, R. Sidhu, A. L. Holmes Jr., J. C. Campbell, "High Power Photodiode Wafer Bonded to Si Using Au with Improved Responsivity and Output Power," *OSA Proceedings of Integrated Photonics Research and Applications,* post deadline paper, April 2005, San Diego, CA

[23] X. Li, **N. Li**, S. Demiguel, J. C. Campbell, D. Tulchinsky, K. J. Williams, "High saturation current, wide bandwidth photodetectors," *2004 IEEE International Topical Meeting on Microwave Photonics*, Ogunquit, Maine

[24] X. Li, **N. Li**, S. Demiguel, J. C. Campbell, D. Tulchinsky, K. J. Williams, "High-saturation-current InP-InGaAs photodiode with partially depleted absorber," *2003 Optical Fiber Communication Conference*, Atlanta, GA

[25] X. Li, **N. Li**, S. Demiguel, J. C. Campbell, D. Tulchinsky, K. J. Williams, "High-saturation-current InP-InGaAs photodiode with partially depleted absorber," *2002 IEEE/LEOS Annual Meeting Conf. Proc*., Glasgow, Scotland

[26] X. Li, **N. Li**, S. Demiguel, J. C. Campbell, D. Tulchinsky, K. J. Williams, "Space charge balance in high-speed high-saturation-current photodetectors," *Proceedings of SPIE - The International Society for Optical Engineering*, v 5246, p 458-464, 2003

[27] S. Demiguel, X. Zheng, **N. Li**, X. Li, J. C. Campbell, J. Decobert, N. Tscherptner,A. Anselm, **"**High-responsivity and high-speed evanescently-coupled waveguide avalanche photodiode," *2004 Optical Fiber Communication Conference*, Los Angeles, CA

[28] S. Demiguel, X. Li, **N. Li**, H. Chen, J. C. Campbell, J. Wei, A. Anselm, "High responsivity and high power partially depleted absorber waveguide photodiodes with relaxed coupling efficiency," *2005 Optical Fiber Communication Conference*, Anaheim, CA

[29] S. Demiguel, X. Li, **N. Li**, H. Chen, J. C. Campbell, J. Wei, A. Anselm, "Partially depleted absorber waveguide photodiodes," *2004 IEEE/LEOS Annual Meeting Conf. Proc.*, Puerto Rico, Paper TuH2

[30] J. C. Campbell, S. Wang, X. Zheng, X. Li, **N. Li**, F. Ma, X. Sun, J.B. Hurst, R. Sidhu, A.L. Holmes, Jr., A. Huntington, L.A. Coldren, "Recent developments in avalanche photodiodes," *Conference on Optoelectronic and Microelectronic Materials and Devices*, pp.53–58, Dec. 2002

[31] J. C. Campbell, S. Demiguel, **N. Li**," High-Speed Photodetectors," *31st European Conference on Optical Communication (ECOC)*, Glasgow, Sept. 25th-30th 2005, Invited paper We3.6.3

Bibliography

Chapter 1:

[1-1] C. H. Cox, III, *Analog Optical Links — Theory and Practice,* Cambridge University Press, 2004

[1-2] C. Cox III, E. Ackerman, R. Helkey, and G. E. Betts, "Techniques and Performance of Intensity-Modulation Direct-Detection Analog Optical Links", *IEEE Transactions on Microwave Theory and Techniques,* Vol. 45, No. 8, pp1375-1383, 1997

[1-3] D.S. Shin, "High Efficiency Optical Modulation and Detection for Analog Fiber Optic Links", Ph.D. Dissertation, University of California at San Diego, 2001

[1-4] M.L. VanBlaricum, " Photonics Systems for antenna applications," *IEEE Antenna Propagation Magazine*, Vol.36, pp30-38, 1994

[1-5] R. D. Atkinson, K. Sandgren, and P.H. Wisseman, " A next generation satellite ground station application using commercial 1300nm fiber optic components to carry K-band microwave signals," *Technical digest of International Topical Meeting of Microwave Photonics*, pp.241-244, 1996

[1-6] T. Kuri, K. Kitayama, A. Stohr, and Y. Ogawa, "Fiber-optic millimeter-wave downlink system using 60GHz-band external modulation," *Journal Lightwave Technolg.,* Vol.17, no.5, pp799-806,1999

[1-7] D. Wake, “Optoelectronics for millimeter-wave radio over fiber systems,” in *Analog Optical Fiber Communications*, edited by B. Wilson, Z. Ghassemlooy, and I. Darwazeh, (IEE, London, UK), pp.202-228, 1995

[1-8] K. J. Williams, L. T. Nichols, and R. D. Esman, “Photodetector Nonlinearity Limitations on a High-Dynamic Range 3 GHz Fiber Optic Link,” *Journal of Lightwave Technology*, Vol. 16, No. 2, 1998, pp192-199

[1-9] K. J. Williams, R. D. Esman, “Design considerations for high-current photodetectors,” *Journal of Lightwave Technology,* Vol.17 No. 8, pp. 1443-1454, 1999

[1-10] Keith J. Williams, Ronald D. Esman, and Mario Dagenais, “Effects of High Space-Charge Fields on the Response of Microwave Photodetectors,” *IEEE Photonics Technology Letters*, Vol. 6, No. 5, pp. 639-641, 1994

[1-11] P.-L. Liu, Keith J. Williams, Michael Y. Frankel, and Ronal D. Esman, “Saturation Characteristics of Fast Photodetectors,” *IEEE Transactions on Microwave Theory and Techniques*, Vol. 47, No. 7, pp. 1297-1303, 1999

[1-12] K. J. Williams, M. L. Dennis, I. N. Duling, C. A. Villarruel, and R. D. Esman, “A simple high-speed high-output-voltage digital receiver,” *IEEE Photonics Technology Letters.,* Vol. 10, pp. 588–590, Apr. 1998.

[1-13] Y. Miyamoto, M. Yoneyama, K. Hagimoto, T. Ishibashi, and N. Shimizu, “40Gbit/s high sensitivity optical receiver with uni-traveling-carrier photodiode acting as decision IC driver,” *Electronics Letters*, Vol. 34, Issue 2, pp214 – 215, 1998

[1-14] T. Ishibashi, N. Shimizu, S. Kodama, H. Ito, T. Nagatsuma and T. Furuta, "Uni-Traveling-Carrier Photodiodes," *Tech. Dig. Ultrafast Electronics and Optoelectronics*, pp.83-87, 1997

[1-15] T. Ishibashi, T. Furuta, H. Fushimi, S. Kodama, H. ITO, T. Nakatsuma, N. Shimizu, Y. Miyamoto, "InP/InGaAs uni-traveling-carrier photodiodes," *IEICE Trans. Electron.*, Vol. E83-C, pp938-949, 2000

[1-16] H. Ito, H. Fushimi, Y. Muramoto, T. Furuta, and T. Ishibashi, "High-Power Photonic Microwave Generation at K- and Ka-Bands using a uni-traveling-carrier photodiode," *Journal of Lightwave Technology*, Vol. 20, No8, pp1500-1505, 2002

[1-17] Frank, J. Effenberger, Abhay M. Joshi, "Ultrafast, Dual-Depletion-Region InGaAs/InP pin Detector," *IEEE Journal of Lightwave Technology*, Vol. 14, No. 8, pp.1859-1864, 1996

[1-18] X. Li, N. Li, S. Demiguel, J. C. Campbell, D. Tulchinsky, K. J. Williams, "High-saturation-current InP-InGaAs photodiode with partially depleted absorber**,"** *IEEE Photonics Technology Letters*, Vol. 15 pp1276-1278, Sept. 2003

[1-19] X. Li, "High-saturation-current partially-depleted-absorber photodetector," Ph.D. Dissertation, The University of Texas at Austin, 2004

[1-20] K. Kato, S. Hata, K. Kawano, J. - I. Yoshida, and A. Kozen, "A High - Efficiency 50 GHz InGaAs Multimode Waveguide Photodetector," *IEEE J. Quantum Electron.*, Vol. 28, pp.2728-2735, 1992

[1-21] S. Demiguel, L. Giraudet, L. Joulaud, J. Decobert, F. Blache, V. Coupé, F. Jorge, P. Pagnod-Rossiaux, E. Boucherez, M. Achouche, and F. Devaux, "Evanescently Coupled Photodiodes Integrating a Double Stage Taper for 40Gb/s Applications – Compared Performance with Side-Illuminated Photodiodes," *IEEE J. Lightwave Technol.,* Vol. 12, pp.2004-2014 , 2002

[1-22] G. Unterbörsh, D. Trommer, A. Umbach, R. Ludwig, and H. G. Bach, "High-power performance of a high-speed photodetector," in *Proc. ECOC'98*, pp. 67-68

[1-23] F. Xia, J. K. Thomson, M.R. Gokhale, P.V. Studenkov, J. Wei, W. Lin and S.R. Forrest, "An Asymmetric Twin-Waveguide High-Bandwidth Photodiode Using a Lateral Taper Coupler", *IEEE Photonics Technol.. Lett.,* Vol. 13, pp845-847, 2001

[1-24] L. Y. Lin, M. C. Wu, T. Itoh, T. A. Vang, R. E. Muller, D. L. Sivco, A. Y. Cho, "Velocity-matched distributed photodetectors with high-saturation power and large bandwidth" *IEEE Photonics Technology Letters*, Vol. 8, Issue 10, pp1376 – 1378, 1996

[1-25] K. J. Williams and R. D. Esman, "Optically amplified downconverting link with shot-noise-limited performance," *IEEE Photonics Technol. Lett*., Vol. 8, no.1, pp.148-150, 1996

[1-26] A. Beling, H. G. Bach, D Schmidt, G. G. Mekonnen, M. Rohde, L. Molle, and H. Ehlers, "High-speed balanced photodetector module with 20dB broadband common-mode rejection ratio," *Optical Fiber Communication Conf.*, Vol. 1, 2003, pp.339-340

[1-27] M.S. Islam, T. Jung, T. Itoh, M. C. Mu, A. Nespola, D. L. Sivco, and A. Y. Cho, "High power and highly linear monolithically integrated distributed balanced photo detectors," *J. Lightwave Technol*., Vol. 20, pp.285-295, Feb. 2002

[1-28] G. A. Davis, R. E. Weiss, R. A. LaRue, K. J. Williams, and R. D. Esman, "A 920-1650nm High Current Photodetector," *IEEE Photonics Technology Letters*, Vol. 8, No. 10, pp. 1373-1375, 1996

[1-29] K. J. Williams, "Comparisons between dual-depletion-region and uni-traveling-carrier p-i-n photodetectors," *IEE Optoelectronics Proceedings*, Vol. 149, No. 4, pp.131-137, Aug. 2002

[1-30] X. Zheng, "Long-Wavelength, High-Speed Avalanche Photodiodes and APD Arrays," Ph.D. Dissertation, The University of Texas at Austin, 2004

[1-31] E. Gramsch, M. Szawlowski, S. Zhang, and M. Madden, "Fast, High Density Avalanche Photodiode Array", *IEEE Trans. On Nuclear Science*, Vol. 41, No.4, 762-766, August 1994

[1-32] G. Karve, "Avalanche Photodiodes as Single Photon Detectors," Ph.D. Dissertation, 2005

[1-33] W. P. Risk, and D. S. Bethune, "Quantum cryptography using autocompensating fiber-optic interferometers," *Optics and Photonics news*, Vol. 13, no. 7, pp. 26, 2002.

[1-34] B. F. Levine, C. G. Bethea, and J. Campbell, "1.52 μm room temperature photon counting optical time domain reflectometer," *Electron. Lett.*, Vol. 21, pp. 194-196 , 1985

[1-35] J. M. Smith, P. A. Hiskett, I. Gontijo, L. Purves and G. S. Buller, "A picosecond time-resolved photoluminescence microscope with detection at wavelength greater than 1500nm", *Review Sci. Intrum*., Vol. 72, no. 5, pp. 2325-2329, 2001

[1-36] J. M. Smith, P. A. Hiskett, I. Gontijo, L. Purves and G. S. Buller, "A picosecond time-resolved photoluminescence microscope with detection at wavelength greater than 1500nm", *Review Sci. Intrum*., Vol. 72, no. 5, pp. 2325-2329, 2001

[1-37] J. C. Tsang, J. A. Kash, D. P. Vallett, "Time-resolved optical characterization of electrical activity in integrated circuits*," Proceedings of the IEEE*, Vol. 88, Issue 9, Sept. 2000 pp1440 – 1459

[1-38] P. A. Hiskett, G. S. Buller, A. Y. Loudon, J. M. Smith, I. Gontjo, A. C. Walker, P. D. Townsend, and M. J. Robertson, "Performance and design of InGaAs/InP photodiodes for single photon counting at 1.55 μm," *Appl. Optics*, Vol. 39, no. 36, pp. 6818-6829, 2000

[1-39] J. G. Rarity, T. E. Wall, K. D. Ridley, P. C. M. Owens, and P. R. Tapster, "Single-photon counting for the 1300-1600-nm range by use of Peltier-cooled and passively quenched InGaAs avalanche photodiodes," *Appl. Optics*, Vol. 39, no. 36, pp. 6746-6753, 2000

[1-40] K. A. McIntosh*,* J. P. Donnelly, D. C. Oakley, and A. Napoleone, "Development of Geiger-mode APD arrays for 1.06 μm", *Proceedings of IEEE LEOS Annual Conference*, Vol. 2, pp. 760-761, 2002

Chapter 2:

[2-1] W. Liu, *Handbook of III-V Heterojunction Bipolar Transistors,* Wiley-Interscience Publication, TK7871.96.B55L57, 1998

[2-2] P. Boury, G. Landgren, "Versatile reactive ion beam etching (RIBE) of InP-based material using CH_4/H_2/Ar chemistry," *Eighth International Conference on Indium Phosphide and Related Materials,* 1996, pp.119 – 120

[2-3] Y.-S. Kim, J. Kim, J.-S. Choe, Y.-G. Roh, H. Jeon, and J. C. Woo, "Semiconductor microlenses fabricated by one-step wet etching," *IEEE Photonics Technology Letters*, Vol. 12, No. 5, pp.507-509, May 2000

[2-4] X. Zheng, "Long-Wavelength, High-Speed Avalanche Photodiodes and APD Arrays," Ph.D. Dissertation, The University of Texas at Austin, 2004

[2-5] S. Demiguel, N. Li; X. Li; X. Zheng; J. Kim, J. C. Campbell, H. Lu; A. Anselm, "Very high-responsivity evanescently coupled photodiodes integrating a short planar multimode waveguide for high-speed applications," *IEEE Photonics Technology Letters*, Vol. 15, Issue 12, Dec 2003 pp1761 – 1763

Chapter 3:

[3-1] K. J. Williams, R. D. Esman, "Design considerations for high-current photodetectors," *J. Light. Technol.*, Vol.17 No. 8, pp. 1443-1454, 1999

[3-2] X. Li, S. Demiguel, Ning Li, J. C. Campbell, D. Tulchinsky, K. J. Williams, **"**Backside illuminated high saturation current partially depleted

absorber photodetectors," *Electronics Letters*, Vol. 39 pp1466-1467, Oct. 2003

[3-3] N. Li, X. Li, S. Demiguel, X. Zheng, J. C. Campbell, D. A. Tulchinsky, K. J. Williams, T.D. Isshiki, G.S. Kinsey, R. Sudharsansan, "High-Saturation-Current Charge-Compensated InGaAs/InP Uni-Traveling-Carrier Photodiode," *IEEE Photonics Technology Letters*, Vol. 16 No.3, pp864-866, Mar. 2004

[3-4] Williams, K. J., "Comparisons between dual-depletion-region and uni-traveling-carrier photodetectors," *IEE. Proc.-Optoelectron.*, August 2002, Vol. 149 No. 4, pp. 131-137

[3-5] H. Ito, H. Fushimi, Y. Muramoto, T. Furuta, and T. Ishibashi, "High-Power Photonic Microwave Generation at K- and Ka-Bands using a uni-traveling-carrier photodiode," *J. Lightwave Technol.* Vol. 20, No8, pp1500-1505, 2002

[3-6] P.D. Hale, T.S. Clement, and D.F. Williams, "Frequency response metrology for high-speed optical receiver", *in proc. OFC'01*, paper WQ1-1.

Chapter 4:

[4-1] C. Cox, III, E. Ackerman, R. Helkey, and G.E. Betts, "Techniques and performance of intensity-modulation direct-detection analog optical links," *IEEE Trans. Microwave Theory Tech.*, Vol.45, pp.1375-1383, Aug 1997

[4-2] E. Ackerman, S. Wanuga, D. Kasemset, A.S. Daryoush, and N. R. Samant, "Maximum dynamic range operation of a microwave external modulation fiber-optic link," *IEEE Trans. Microwave Theory Tech.,* Vol. 41, pp.1299-1306, Aug. 1993

[4-3] L. T. Nichols, K.J. Williams, and R.D. Esman, "Optimizing the ultrawide-band photonic link," *IEEE Trans. Microwave Theory Tech.,* Vol.45, pp.1384-1389, Aug. 1997

[4-4] G. L. Abbas, V. W. S. Chan, and T. K. Yee, "A dual-detector optical heterodyne receiver for local oscillator noise suppression," *J. Lightwave Technol.*, Vol. LT-3, pp.1110-1122, 1985

[4-5] K. J. Williams and R. D. Esman, "Optically amplified downconverting link with shot-noise-limited performance," *IEEE Photonics Technol. Lett.*, Vol. 8, no.1, pp.148-150, Jan 1996

[4-6] A. Beling, H. G. Bach, D Schmidt, G. G. Mekonnen, M. Rohde, L. Molle, and H. Ehlers, "High-speed balanced photodetector module with 20dB broadband common-mode rejection ratio," *Optical Fiber Communication Conf.*, Vol. 1, 2003, pp.339-340

[4-7] S. S. Afashe, S. Datta, F. Xia, and S. R. Forrest, "A monolithically integrated long-wavelength balanced photodiode using asymmetric twin-waveguide technology," *IEEE Photonics Technol. Lett*., Vol. 16, no. 1, pp.236-238, Jan 2004

[4-8] M.S. Islam, T. Jung, T. Itoh, M. C. Mu, A. Nespola, D. L. Sivco, and A. Y. Cho, "High power and highly linear monolithically integrated

distributed balanced photo detectors," *J. Lightwave Technol.*, Vol. 20, pp. 285-295, Feb. 2002

[4-9] M.S. Islam, S. Murthy, T. Itoh, M. C. Mu, D. Novak, R. B. Waterouse, D. L. Sivco, and A. Y. Cho, "Velocity-matched distributed photodetectors and balanced photodetectors with p-i-n photodiodes," *IEEE Trans. Microwave Theory Tech.,* Vol. 49, pp.1914-1920, Oct. 2001

Chapter 5:

[5-1] K. Kato, S. Hata, K. Kawano, J. - I. Yoshida, and A. Kozen, "A High - Efficiency 50 GHz InGaAs Multimode Waveguide Photodetector," *IEEE J. Quantum Electron*., Vol. 28, pp.2728-2735, 1992

[5-2] S. Demiguel, L. Giraudet, L. Joulaud, J. Decobert, F. Blache, V. Coupé, F. Jorge, P. Pagnod-Rossiaux, E. Boucherez, M. Achouche, and F. Devaux, "Evanescently Coupled Photodiodes Integrating a Double Stage Taper for 40Gb/s Applications – Compared Performance with Side-Illuminated Photodiodes," *J. Lightwave Technol.,* Vol. 12, pp. 2004-2014, 2002

[5-3] G. Unterbörsh, D. Trommer, A. Umbach, R. Ludwig, and H. G. Bach, "High-power performance of a high-speed photodetector," *Proc. ECOC'98*, pp. 67-68

[5-4] F. Xia, J. K. Thomson, M.R. Gokhale, P.V. Studenkov, J. Wei, W. Lin and S.R. Forrest, "An Asymmetric Twin-Waveguide High-Bandwidth Photodiode Using a Lateral Taper Coupler", *IEEE Photonics Technol. Lett.*, Vol. 13, pp.845-847, 2001

[5-5] T. Takeuchi, T. Nakata, K. Makita and T. Torikai, “A high-power and high-efficiency photodiodes with an evanescently coupled graded-index waveguide for 40Gb/s applications,” *Proc. OFC’01*, Vol. 3, Paper WQ2-1

[5-6] M. Achouche, S. Demiguel, E. Derouin, D. Carpentier, F. Barthe, F. Blache, V. Magnin, J. Harari, and D. Decoster, “New All 2-inch Manufacturable High Performance Evanescent Coupled Waveguide Photodiodes with Etched Mirrors for 40Gb/s Optical Receivers”, *Proc. OFC’03*, paper WF5

[5-7] X. Li, N. Li, S. Demiguel, J. C. Campbell, D. Tulchinsky, K. J. Williams, “High-saturation-current InP-InGaAs photodiode with partially depleted absorber,” *IEEE Photonics Technol. Lett.*, Vol. 15 pp1276-1278, 2003

Chapter 6:

[6-1] D. A. Tulchinsky, K. J. Williams, A. Pauchard, M. Bitter, P. Zhong, S. Kristjansson, L. A. Hodge, S. G. Hummel, Y. H. Lo **“**High-power InGaAs-on-Si pin RF photodiodes,” *Electronics Lett*., Vol. 39, No.14, pp1084-1086, Jul. 2003

[6-2] K. J. Williams, R. D. Esman, “Design considerations for high-current photodetectors,” *J. Lightwave Technol*., Vol.17 No. 8, pp. 1443-1454, 1999

[6-3] A. Pauchard, M. Bitter, P. Zhong, S. Kristjansson, L. A. Hodge, K. J. Williams, D. A. Tulchinsky, S. G. Hummel, Y. H. Lo, **“**Infrared-sensitive InGaAs-on-Si p-i-n photodetectors exhibiting high-power linearity,” *IEEE Photonics Technol. Lett*., Vol.16, No.11, pp2544-2546, Nov. 2004

[6-4] D. Tauber, M. Horita, J. Piprek, P. Abraham, A. L. Holmes, Jr., and J. E. Bowers, "The microstrip laser," *IEEE Photonics Technol. Lett.*, Vol. 10, No. 4, April 1998

[6-5] X. Zheng, "Long-Wavelength, High-Speed Avalanche Photodiodes and APD Arrays," Ph.D. dissertation, The University of Texas at Austin, 2004

Chapter 7:

[7-1] G. S. Kinsey, J. C. Campbell, and A. G. Dentai, "Waveguide Avalanche Photodiode Operating at 1.55 μm with a Gain-Bandwidth Product of 320 GHz," *IEEE Photon. Technol. Lett.*, Vol. 13, No. 8, pp. 842-844, 2001

[7-2] T. Nakata, T. Takeuchi, J. Watanabe, K. Makita, T. Torikai, "10Gbit/s high sensitivity, low-voltage-operation avalanche photodiodes with thin InAlAs multiplication layer and waveguide structure," *Electron. Lett.*, Vol. 36, No. 24, pp. 2033 –2034, 2000

[7-3] C. Lenox, H. Nie, P. Yuan, G. Kinsey, A. L. Holmes, Jr., B. G. Streetman, and J. C. Campbell, "Resonant-cavity InGaAs–InAlAs avalanche photodiodes with gain-bandwidth product of 290 GHz," *IEEE Photon. Technol. Lett*., Vol. 11, pp. 1162–1164, 1999

[7-4] H. Nie, K. A. Anselm, C. Lenox, P. Yuan, C. Hu, G. Kinsey, B. G. Streetman, and J. C. Campbell, "Resonant-cavity separate absorption, charge and multiplication avalanche photodiodes with high-speed and high gain-bandwidth product," *IEEE Photonics Technol. Lett.*, Vol. 10, No. 3 , p 409 –411, 1998

[7-5] J. C. Jackson, P. K. Hurley, B. Lane, A. Mathewson, and A. P. Morrison, "Comparing leakage currents and dark count rates in Geiger-mode avalanche photodiodes," *Appl. Phys. Lett.,* pp. 4100-4102, 2002

[7-6] T. Ishibashi, N. Shimizu, S. Kodama, H. Ito, T. Nagatsuma and T. Furuta, "Uni-Traveling-Carrier Photodiodes," *Tech. Dig. Ultrafast Electronics and Optoelectronics*, pp.83-87, 1997

[7-7] T. Ishibashi, " Nonequilibrium Electron Transport in HBTs," *IEEE Transactions on Electron Devices*, Vol.48, No.11, pp. 2595-2605, 2001

[7-8] T. Ishibashi, S. Kodama, N. Shimizu, T. Furuta, "High speed response of uni-traveling-carrier photodiodes," *Jpn. J. Appl. Phys.*, Vol. 36, pp. 6263-7268, 1997

[7-9] T. Ishibashi, T. Furuta, H. Fushimi, S. Kodama, H. ITO, T. Nakatsuma, N. Shimizu, Y. Miyamoto, "InP/InGaAs uni-traveling-carrier photodiodes," *IEICE Trans. Electron.*, Vol. E83-C, pp938-949, 2000

[7-10] N. Yasuoka, H. Kuwatsuka, A. Kuramata, "High-speed and high-efficiency InP/InGaAs waveguide avalanche photodiodes for 40Gbit/s transmission systems, " *OFC2004*, paper TuM2

[7-11] H. S. Kim, J. H. Choi, H. M. Bang, Y. Jee, S. W. Yun, J. Burm, M.D. Kim and A. G. Choo, "Dark current reduction in APD with BCB passivation," *Electronics Lett.*, Vol. 37, No.7, pp.455-456, 2001

[7-12] A. Karlsson, M. Bourennane, G. Ribordy, H. Zbineden, J. Brendel, J. Rarity, and P. Tapster, "Single photon counting at 1550nm using

InGaAs/InP avalanche photodiodes," *Circuits & Devices*, Nov 1999, pp.34-40

[7-13] E. Kuphal, K. Mause, K. Miethe, A. Eisenbach, F. Fiedler, A. Corbet, " Electron diffusion length in InGaAs: Zn Derived from heterostructure bipolar transistors," *Solid-State Electronics*, Vol. 38, No. 4, pp.795-799, 1995

[7-14] M. Levinstein, S. Rumyantsev and M. Shur, *Handbook Series on Semiconductor Parameters*, World Scientific, London, 1996

[7-15] S. R. Forrest, "Performance of lnxGa1-xAsyP1-y Photodiodes with Dark Current Limited by Diffusion, Generation Recombination, and Tunneling," *IEEE J. Quantum Electron.*, Vol. QE17, pp217-226, 1981

[7-16] J. N. Hollenhorst, "Frequency Response Theory for Multilayer Photodiodes," *IEEE J.Lightwave Technol.*, Vol. 8, No. 4, pp. 531-537, April 1990

[7-17] S. Adachi, *Optical Constants of Crystalline and Amorphous Semiconductors*, Kluwer Academic Publishers, QC611.6 O6 A3, 1992, pp.362

[7-18] F. Ma, S. Wang, X. Li, K. A. Anselm, X. G. Zheng, A. L. Holmes, Jr., and J. C. Campbell, "Monte Carlo simulation of low-noise avalanche photodiodes with heterojunctions," *J. Appl. Phys.,* V92, N8, Oct 2002, pp.4791-4795

[7-19] P. Yuan, C. C. Hansing, K. A. Anselm, C. V. Lenox, H. Nie, A. L. Holmes, Jr., B. G. Streetman and J. C. Campbell, "Impact ionization

characteristics of III-V semiconductors for a wide range of multiplication region thicknesses," *IEEE J. Quantum Electron.,* Vol.36, No.2, Feb. 2000, pp.198 –204

[7-20] S. Wang, R. Sidhu, X.G. Zheng, X. Li, X. Sun, A. L. Holmes, Jr., and J.C. Campbell, "Low-Noise Avalanche Photodiodes With Graded Impact-Ionization-Engineered Multiplication Region," *IEEE Photonics Technol. Lett.*, Vol.13, no.12, pp.1346-1348, 2001

[7-21] N. Li, R. Sidhu, X. Li, F. Ma, X. Zheng, S. Wang, G. Karve, S. Demiguel, A. L. Holmes, Jr., and J. C. Campbell, "InGaAs/InAlAs Avalanche Photodiode with Undepleted Absorber," *Appl. Phys. Lett.,* Vol. 82 No.13, pp2175-2177, Mar. 2003

[7-22] Y. Hirota, S. Ando, and T. Ishibashi, "High-Speed Avalanche Photodiode with a Neutral Absorption Layer for 1.55μm Wavelength," *Jpn. J. Appl. Phys.*, Vol. 43, No 3A, 2004, ppL375-L377

[7-23] S. Wang, "Low Noise Avalanche Photodiodes with An Impact-Ionization-Engineered Multiplication Region," Ph.D. dissertation, The University of Texas at Austin, 2002

[7-24] X. Zheng, "Long-Wavelength, High-Speed Avalanche Photodiodes and APD Arrays," Ph.D. dissertation, The University of Texas at Austin, 2004

Chapter 8:

[8-1] C. A. Pan, T. P. Ma, "Highly transparent conductive films of thermally evaporated In_2O_3," *Journal of Electronic Materials*, Vol. 10, No. 1, pp. 43-57, 1981

[8-2] L. Zheng, X. Zhang, Y. Zeng, S. R. Tatavarti, S. P. Watkins, C. R. Bolognesi, S. Demiguel, J. C. Campbell, “Demonstration of high-speed staggered lineup GaAsSb-InP uni-traveling-carrier photodiodes,” *IEEE Photonics Technology Letters*, Vol. 17, Issue 3, pp. 651 – 65, March 2005

Vita

Ning Li (李宁) was born in Shaanxi, China, on July 6, 1978, the son of Junli Xu (徐俊利) and Huaide Li (李怀德). After completing his study at the Beijing No. 8 middle school, he entered the Electronics Engineering Department of Tsinghua University in Beijing, China, where he received the degree of Bachelor of Science and Master of Science in July 1998 and December 2000, respectively. In January 2001, he entered the graduate program in Electrical and Computer Engineering department at the University of Texas at Austin to pursue his Ph.D. degree.

Permanent address: 11 Fucheng Rd., Bldg. 5, Unit 2, Room 204,
Beijing 100037, China

This dissertation was typed by the author.